Early Detection of Lung Cancer Using Fusion Techniques

By

Imran Nazir

Registration No: 74-FET/PHDEE/F14

A dissertation submitted to IIU in partial fulfilment of the requirements for the degree of

DOCTOR OF PHILOSOPHY

Department of Electronic Engineering
Faculty of Engineering and Technology
INTERNATIONAL ISLAMIC UNIVERSITY
ISLAMABAD

2022

Lung-Cancer-Diagnosis
Medical imaging-Data processing
Image fusion
Biomedical engineering
Computer-assisted diagnosis
Diagnostic imaging-Technology

This dissertation includes the following subsequent research articles.

1. Nazir, I., Haq, I. U., Khan, M. M., Qureshi, M. B., Ullah, H., Butt, S. (2021). Efficient pre-processing and segmentation for lung cancer detection using fused CT images.Electronics,11(1), 34. (IF. 2.68)

2. Nazir, I., Haq, I. U., Khan. Enhanced Lung CT Image Segmentation using Multi View Image Registration and Fusion for Lung Cancer Detection. Frequenz.(Submitted, IF. 1.02)

 It is declared that the research work presented in this dissertation "Early Detection of Lung Cancer Using Fusion Techniques", is solely my work.

CERTIFICATE OF APPROVAL

Title of Thesis: Early Detection of Lung Cancer Using Fusion Techniques

Name of Student: IMRAN NAZIR

Registration No: 74-FET/PhDEE/F14

Accepted by the Department of Electrical and Computer Engineering, Faculty of Engineering and Technology, International Islamic University (IIU), Islamabad, in partial fulfillment of the requirements for the Doctor of Philosophy degree in Electronic Engineering.

Viva voce committee:

DR. IHSAN-UL-HAQ
Associate Professor
Department of Electrical Engineering
Faculty of Engineering & Technology
International Islamic University
Islamabad-Pakistan

Dr. Ihsan ul Haq (Supervisor)
Associate Professor DECE, FET IIU Islamabad

Dr. Muhammad Mohsin Khan (Co-Supervisor)
Lecturer DECE, FET IIU Islamabad

Prof Dr. Muhammad Amir (Internal)
Professor DECE, FET, IIU Islamabad

Dr. Hafiz Muhammad Faisal Zafar (External-I)
Deputy Chief Scientist, PAEC, Islamabad

Dr. Abdul Basit (External-II)
Senior Scientist, TPPD, PINSTECH, Nilore, Islamabad

Dr. Shahid Ikram (Chairman, DEE)
Assistant Professor DECE, FET, IIU Islamabad

Prof. Dr. Nadeem Ahmad Sheikh (Dean, FET)
Professor DME, FET, IIU Islamabad

14th September, 2022

DEDICATION

My respected teachers, parents, sisters, wife and friends.

Abstract

Radiologists have been analyzing multi-view single images for the past twenty years to find cells that are growing abnormally. This abnormal growth of cells is known as cancer which can be benign or malignant. Most common cause of death is lung cancer. It is possible to cure cancer if it is detected at an early stage. Computed Tomography (CT) scan is one of the reliable screening method. Lung cancer detection technique proposed in last two decades are single image based technique. If multiple detection techniques are employed on single data, this would give better results.

Multi-resolution Rigid Registration (MRR), which is applied in this dissertation for multi-view image registration, is used for pre-processing. Lung segmentation is performed after pre-processing. The lung segmentation techniques have been developed for early lung cancer detection. These techniques based on the adaptive globe threshold algorithm in combination with masking and morphological operations. The multi-view image fusion combines Adaptive Sparse Representation (ASR) and Laplacian Pyramid (LP) decomposition. The images are divided into various sizes using the LP decomposition approach in the suggested fusion technique. Following that, the four decomposed layers are fused using LP. The resultant fused image is then acquired using the inverse LP transform. Secondly, the fused image is also obtained using the inverse LP transformation method, which preserves detailed information while reducing image noise and block effect. Finally, the Support Vector Machine (SVM) classifier is used to categorize lung nodules. Intensity, shape and texture were selected to enhance accuracy, sensitivity,

specificity and decrease false positives rate. With only 2.0 false positives per scan, the achieved accuracy, sensitivity, and specificity at the detection and classification stages are 98.0%, 97.90 % and 98.5% respectively.

In this research work, Discrete Wavelet Transform (DWT) and Principle Component Averaging (PCAv) is used for fusion. The proposed DWT-PCAv fusion method contributes well-established details with reduced computational time, however the recommended MRR technique produces significant results compared to Single Rigid Registration (SRR). To evaluate the proposed techniques Lung Image Database Consortium (LIDC) dataset has been used. The outcomes of the suggested fusion techniques are compared with those of the existing approaches. For quantitative assessment, seven different quality analysis measures are used to quantify the results. The proposed technique improves the Feature Mutual Information (FMI), Peak Sign to Noise Ratio (PSNR), and computational time to 0.80, 19.25, and 0.08s, respectively. The detection and stages of cancer of lung nodules is also assessed by using Global Average - Convolutional Neural Network (GA-CNN) classifier. With only 1.8 FP/scan, the achieved sensitivity for detection and classification is 96.4%. Moreover, proposed MRR techniques eliminate the SRR's drawbacks and give more precise image details.

Acknowledgements

ALLAH, The Most Merciful, The Most Gracious. I would want to thank ALLAH for giving me the stamina and endurance to complete this research. All praise and thanks to ALLAH for His last Prophet Muhammad (Sallulahu 'Alayhi wa Sallam) and all of His Sahaba (Razi-Allahu 'Anhu) who dedicated their lives to Dawah and the dissemination of knowledge.

I offer my profound gratitude to my Supervisor Dr. Ihsan ul Haq and my Co-Supervisor, Dr. Muhammad Mohsin Khan, at Yale University in the USA for their support, inspiration, innovative ideas, and guidance. Without their continuous efforts and kind guidance this work would not have been possible.

Special thanks to my teacher Dr. Ijaz Mansoor Quershi (Late), who always encouraged me and conveyed the spirit and guidance necessary for this research. I pay my heartiest thanks to my colleague, Engr. Fahad Munir always helped me in time of need.

My father, mother, sisters, wife, other family members and friends deserve my gratitude. Their prayers, love, and unwavering support throughout my education were among the strongest motivators.

(Imran Nazir)

Contents

List of Figures

List of Tables

Chapter 1

Introduction

1.1 Introduction

Each component of information has worth, allowing you to provide the valuable content material you need. The segmentation and fusion of lungs images is the main objective of this dissertation. Patients have a better chance of surviving lung cancer if detected early. Radiologists are helped during the diagnosis process by automatic detection of lungs cancer. Image fusion is a sub-field of image processing that aids in forming the final image. Image fusion provides a systematic framework for improving the accuracy and applicability of information derived from a collection of source images obtained from various resources. Various tool developments in image processing systems aid in extracting a wide range of data from image database. Such data is combined using an "image fusion" method to produce a more insightful and beneficial image that contains more useful and fruitful information than a collection of input images.

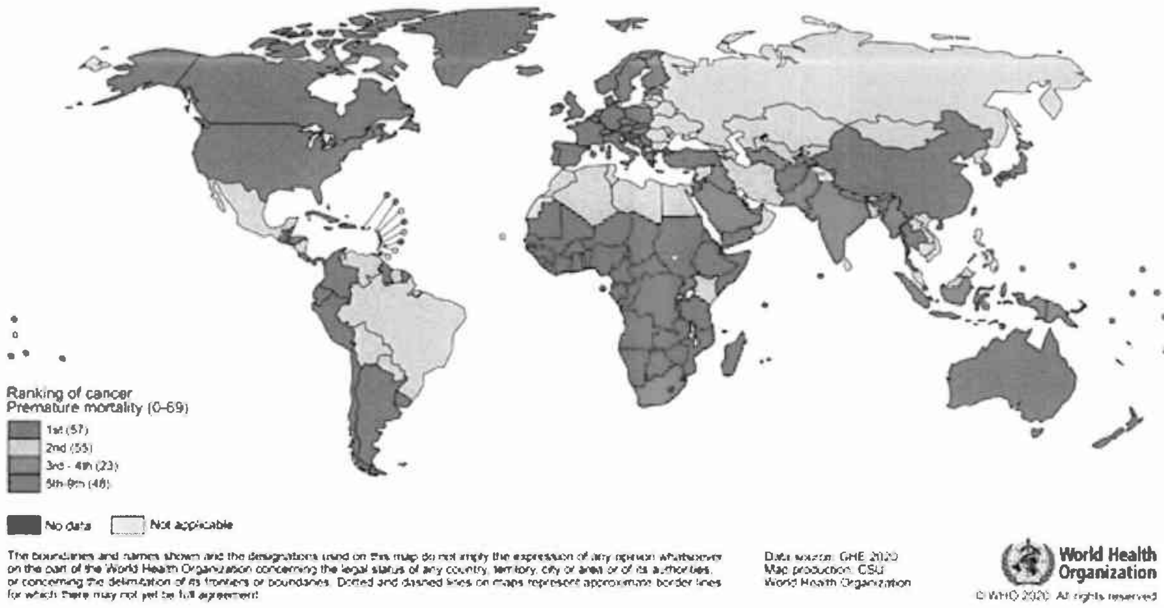

Figure 1.1: Causes of mortality for adults over seventy years in 2019.

1.2 Lung Cancer

In every country of the world, increasing life expectancy is significantly affected by cancer, which is the primary cause of mortality. According to World Health Organization (WHO) data, cancer is the third or fourth major cause of death before the age of seventy in 23 of the 183 countries indicated in Figure 1.1, and the first or second leading cause in 112 of those countries.

The survival rate can be improved by detecting nodules initially [1]. It can be used in both developed and developing nations [2]. According to estimates 225,000 people in the United States (US) are diagnosed with lung cancer per year, costing 12$ billion in health care [3]. According to another report 433 Americans die from lung cancer every day [4]. The year 2005 was the deadliest in terms of lung cancer deaths with a staggering total of 159,292. However, with 155,610 deaths recorded in 2014, there has been a slight decline of 2.3% since then. Men have been the hardest hit by this disease with a higher age-adjusted average of 51.7% per 100,000 versus 34.7% per 100,000 for women. While black and white women have almost identical rates, black men have a higher rate of 45.7% per 100,000 people than white men, 45.4% per 100,000 people [5].

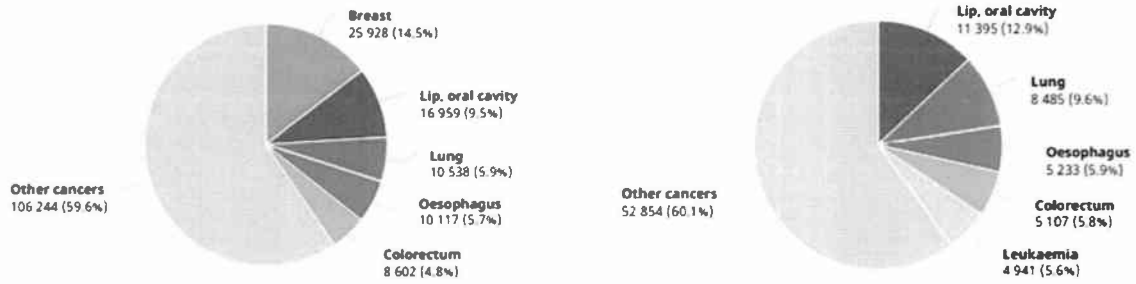

(a) (b)

Figure 1.2: Facts of Cancer in Pakistan (2020) By WHO, (a): male and female (b): males of all ages

In developing nations, the situation is much more alarming. Lung cancer in Asia is most prevalent cancer with having the highest risk [6]. According to estimates, lungs cancer deaths in Asia increased to 926,436 cases out of 1,033,881 in 2012, with a miserable mortality risk of 11.5% [6]. According to a different report, Asia accounts for 51% of lung cancer cases [7]. Apart from tobacco, the primary cause of this deadly disease, lack of knowledge, poor hygienic conditions, and meat intake are the other major factors [8]. Lung cancer in Pakistan is the third-primary factor of mortality. Total 9771 new cases were registered in Pakistan in 2020 by WHO as shown in Figure 1.2a and 1.2b.

The first sign of lung cancer is the appearance of a nodule in the lung. To diagnose lungs cancer, doctors usually recommend a variety of tests. The most critical of these measures is radiography screening, which involves CT [5], MRI [6] and PET [6]. The most popular and cost-effective form of detecting lung cancer is the CT scan [7]. The presence of abnormalities on a CT scan suggests that an individual may be at risk for lung cancer. CT scan procedure produce the more than a hundred patient images. To diagnose cancer, radiologists must review all images that take a long time and are vulnerable to errors. To address this problem radiologists needs automated or semi-automated systems that assist them in clearly distinguishing between cancerous and non-cancerous regions. Decision-making systems contribute a significant role in early detection in medical imaging [9]. Radiologists benefit from these programs because they have a second opinion. In classifying abnormal lesions in CT scan images, radiologists employ various decision-making algorithms. Multiple computer vision algorithms are used in these systems.

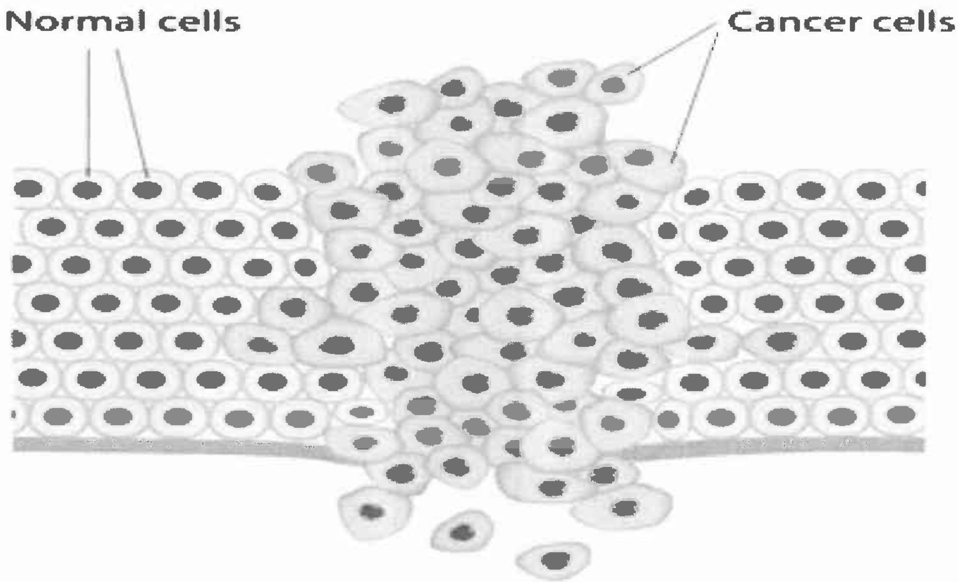

Figure 1.3: Normal versus cancer cells.

1.3 Lung Cancer and Nodule Detection

The development of cancerous nodules in the lung area or periphery is the prime reason for lung cancer as shown in Figure 1.3. Lung tissue defects with an approximately spherical shape and a diameter in the range of 3-30 mm are called nodules [10], [11]. Well-circumscribed, juxta-vascular, juxta-pleural, and pleural tail are the different types of lung nodules as shown in Figure 1.4. Solitary nodules with no connections to adjacent vessels or other anatomical structures are known as well-circumscribed nodules. The attached portion of juxta-pleural nodules adjacent to the pleural surface has been discovered. That surface has its tail nearby the pleural wall. The lung normal functioning can be disrupted by larger nodules and causes death in a short time [12]. When a nodule grows, it becomes more challenging to treat the patient [13]. So that, the detection of cancer in the initial stage is more desirable and highly recommended.

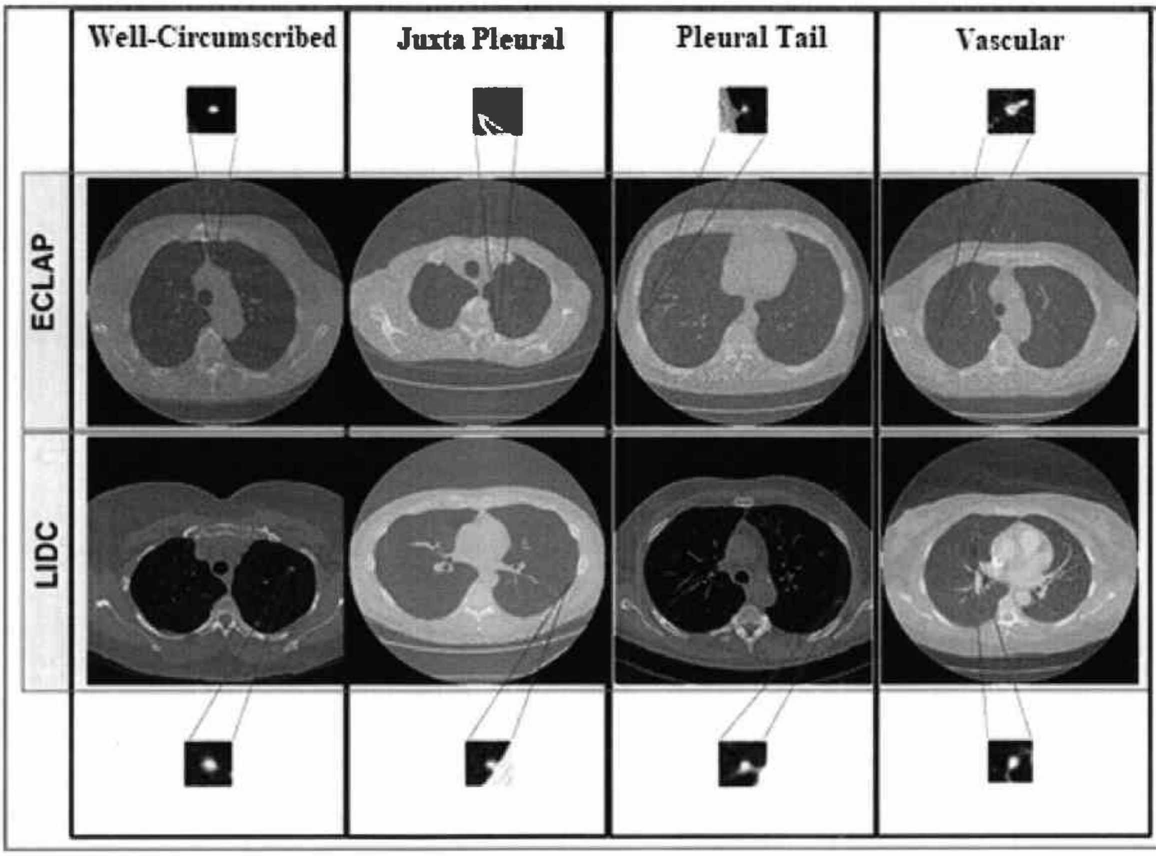

Figure 1.4: Lung nodule size less than 10 mm from two different clinical studies

1.4 Computer-Aided Detection (CAD)

Identification of lung nodules at the initial stage can be aided by CAD. CAD is a term used in radiology to describe medical procedures that help doctors interpret medical images [14]. The value of CAD has grown significantly due to the quick advancement of imaging techniques in medical science. Through non-invasive human body examination, imaging techniques in medical science assist researchers in gathering potentially life-saving data. The medical image analysis community has been pre-occupied with the difficult task of extracting clinically useful knowledge from anatomic structures images using CT, MRI, PET, and other modalities using computers. Table 1.1 shows the pros and cons of multiple screening methods.

Despite the fact that modern imaging devices provide excellent views of internal anatomy, ability of computers to accurately and effectively enumerate and examine embedded structures is limited. Accurate, reproducible, and quantifiable data must be extracted appropriately to en-

Table 1.1: Comparison of the various screening techniques

Screening Methods	Advantages	Disadvantages
X-Ray	Less expensive, quick, simple to perform, provide significant information. It is recommended for initial screening.	Invasive, provide few details, high false positive
CT	Highly sensitive, gold standard, 3D image	Expansive, high X-Ray dose, Invasive
MRI	Better contrast resolution, No ionizing radiation, very sensitive	Expensive
PET	Low false positive rate, non-invasive high resolution, highly sensitivity, assesses the metabolic activity of tumors	Expensive
Sputum Cytology	Non-invasive, useful for centrally located malignancies, less expensive	Non-specific for tumor types, false negative, low sensitivity

sure the integrity of scientific studies and medical procedures from diagnosis through radiation and surgery. As a result, the actual extraction of interest zones is the basic concept of CAD [15], [16]. CAD accomplishes three main objectives:

1. Improve the diagnostic accuracy.
2. Improve treatment outcomes by detecting cancer early.
3. Avoid taking biopsies that are not required.

1.4.1 Computed Tomography (CT)

CT images are created by integrating X-ray technology with a computer to aid doctors in visualizing and examining the body in greater detail. An X-ray tube takes images by slowly rotating 360 degrees across the human body.

It's a technique for examining the human body's internal structure in great detail, allowing doctors to scan for internal bleeding, masses, brain tumors, and lung nodules. It has been a common imaging modality over the last two decades. For bone structures, CT provides more detailed results. CT scans take less time and are less affected by patient movement as compared to MRI or PET scans. It is less expensive and detect nodules of size less than 3mm [17] as shown in Figure 1.5, which would be undetectable through standard X-ray of lung. On a reality

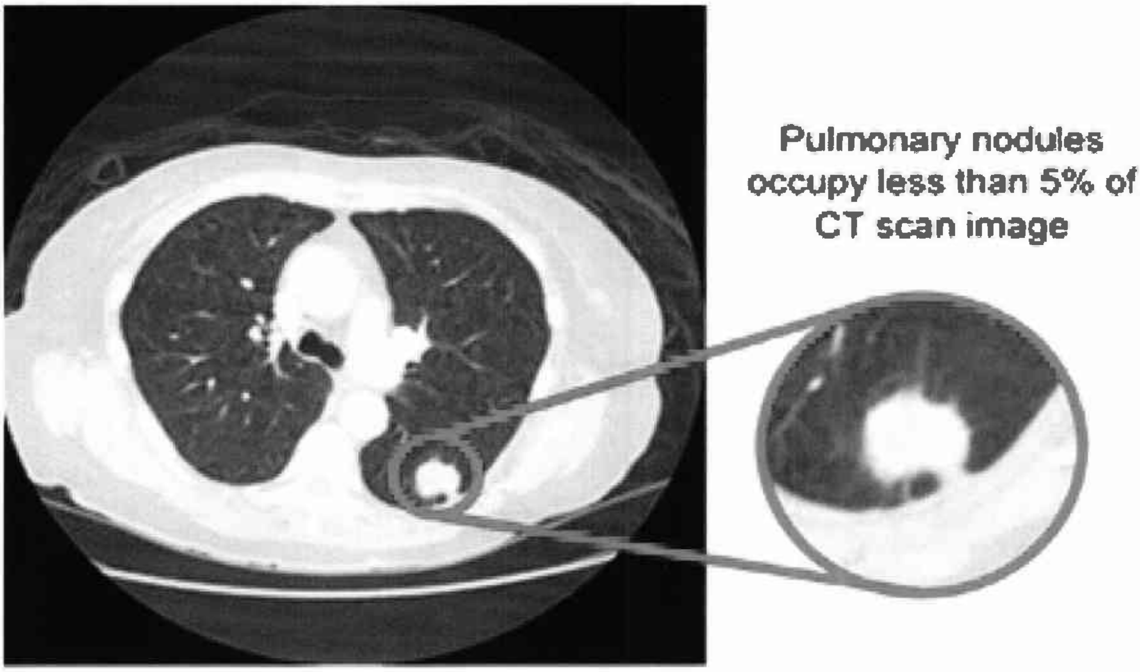

Figure 1.5: Pulmonary nodule in CT scan lung image.

basis, CT screening result shows that majority of cases are undetectable through a standard chest X-ray. However, Low Dose Computed Tomography (LDCT) is recommended because, due to advances in CT, it can detect smaller nodules than traditional chest radiography [18].

1.5 Lung CT Imaging Data Sets

In the performance assessment of a diagnostic method, a well-characterized repository is critical. In majority of the research, clinical data from various hospitals were used which were labor and time-intensive process. Normalizing these images necessitates additional work. As a result, a standard repository must be developed, which will take much time and human resources [19]. In recent years, several researchers have been pursuing this issue to increase the diagnostic system's precision and reduce the probability of false positives. [20].

1.5.1 Lung Image Database Consortium (LIDC)

LIDC is an open accessible dataset that researchers can use to test the efficiency of their proposed methods. The National Cancer Institute's Imaging Archive (NCIIA) [21], [22] provides this dataset. This thoracic CT image database was created in collaboration with five medical imaging research groups [23]. The nodules were annotated with regard to their location and size by four experienced radiologists from various institutions. Nodules in this dataset range in size from 3 to 30 mm. [21].

1.5.2 Lung Image Database Consortium-Image Database Resource Initiative (LIDC-IDRI)

The expanded LIDC dataset is known as LIDC-IDRI. The LIDC has 4,682 scanned CT images of 61 lung cancer patients, including nodules ranging in size from 3 - 30 mm that were thoroughly interpreted by different experts. Image Database Resource Initiative (IDRI) was merged with it in 2004. The database has grown with the passage of time, resulting in LIDC-IDRI. It is most comprehensive database for evaluating pulmonary nodule diagnostic systems. Furthermore, researchers can access an XML file repository that contains annotation information for the nodules in the dataset in addition to the image data. This dataset has become a benchmark in recent years, and it is the most commonly used in the performance assessment of diagnosis methods [24].

1.6 Image Fusion

Image fusion is a technique where a system collects similar details from different images and puts them into one image. Technologies likes these are commonly used in the military, remote sensing, medical imaging, astronomy, and many other important domains. Image fusion is a technique for enhancing information quality by merging two or more images. When different data sets are combined with several imaging systems (e.g., airborne, satellite-based, ground-based), object recognition programs can work much better due to the advanced image fusion technology. It also assists in image sharpening, geometric corrections, enhancing features that are not visible in either image, replacing faulty data, and complementing data collection to improve the process of making the right decisions. Here, critical details from input images are assembled to get an improved version of source images in the form of an optimized image (while keeping original data intact.) [25]. Because of the presence of natural and man-made objects in the image, a high-resolution panchromatic image provides geometric data, while a low-resolution multi-spectral image provides color information. According to different application areas, there are four major image fusion components:

1. Multi-focus image fusion
2. Multi-modal image fusion
3. Visible infrared image fusion
4. Multi-spectral image fusion

1.7 The Motivation of Research

A significant increase in lung cancer ratio can be found both in developed and developing countries. Lung cancer is estimated to affect 225,000 people in the United States per year costing 12$ billion in health care. Therefore, it's critical to find lung cancer at an early stage. False positives remain a problem with lung nodule diagnosis approaches. This may be due to radiologist exhaustion, poor image quality, a lack of proficiency and radiologist experience, all of which increase dependence on Phase Congruency (PC) innovation and CAD frameworks. The sensitivity of lung cancer screening is also affected by the image quality. This task is ceptional challenging complete due to a lack of professional radiologist and a large number of patients. All of the above issues illustrate the need for a CAD scheme. Additionally, this approach may be utilised as a second opinion to confirm a radiologist's results, allowing for the early detection of symptoms.

1.8 Problem Statement and Objectives of the Study

Many techniques for diagnosing lung cancer have been developed in the last few years. The accuracy of these systems meets the bottom level of requirements and demands more improvements. All the developed techniques use a single screening method to detect cancer and have limited scope. These algorithms work only with limited datasets. Therefore, foremost need to develop algorithms that may work all kinds of images (noisy, low contrast etc.) with high accuracy. This can only be achieved using image fusion concepts (pixel level, feature level, decision level).

Followings are the objectives of this research work:

i. The main objective of the research is to develop a novel approach to multi-view medical image fusion for better subjective and objective quality.

ii. To develop algorithms, extract the important details from each image, and form a new fused image.

iii. Another significant objective of the research is to develop a robust fusion system that can deal with different multi-view images.

1.9 Thesis Organization

This chapter is one of five that make up this thesis.

Chapter 1 introduces briefly about Lung cancer. Its statistics and the requirement for automated diagnosis tools. It discusses the main goals, inspiration, and limitations in the research.

Chapter 2 presented the recently developed lung cancer diagnosis methods proposed in recent years. This review provides details on various image investigation, fusion, and artificial intelligence methods used in the literature for lung cancer detection and classification.

Chapter 3 includes a multi-view medical image fusion approach built on LP decomposition and ASR. In this approach, ASR was used to reduce the noise, produced on by the high rate of recurrence data. Moreover, SVM classifier was used for the detection and classification of lung nodules into malignant and benign.

Chapter 4 discusses the multi-view strategy used to expand the amount of qualitative and quantitative medical imaging data. For image registration, MRR is used, while image fusion uses the DWT and PCAv. A novel GA-CNN classifier was used for the detection, classification, and staging of lung nodules according to their sizes.

Chapter 5 concludes the thesis by providing summarized outcomes, contributions, and future research areas.

Chapter 2

Literature Review

In this chapter of dissertation we emphasise different reviews pertained to our problem. To detect irregular growths on the lung patients usually undergo X-ray or CT scans, Sputum Cytology (SC), PET, and biopsy. New emerging technologies, such as molecular markers, Discrete Cosine Transform (DCT) technique, Artificial Intelligence (AI) based technology, hybrid energy imaging, and fusion imaging open the door to early lung cancer detection without surgery or misdiagnosis and lower mortality rates. Novel techniques of the image fusion has also been discussed in this chapter.

2.1 Introduction

Over the past ten years, several experts conducted different development studies to classify and define nodules by processing radio-graphs using computer vision and machine intelligence algorithms. These techniques are more valuable in terms of efficiency and precision. [25]. In 1980, the University of Chicago [26] began developing computer-based systems. The primary goal of these applications was to include a computer-based framework that would enhance the radiologist's ability to interpret CT images with greater accuracy and reliability. It had to be a time-saving tool as well. [27], [28]. The key goal of the CAD method is to use computer

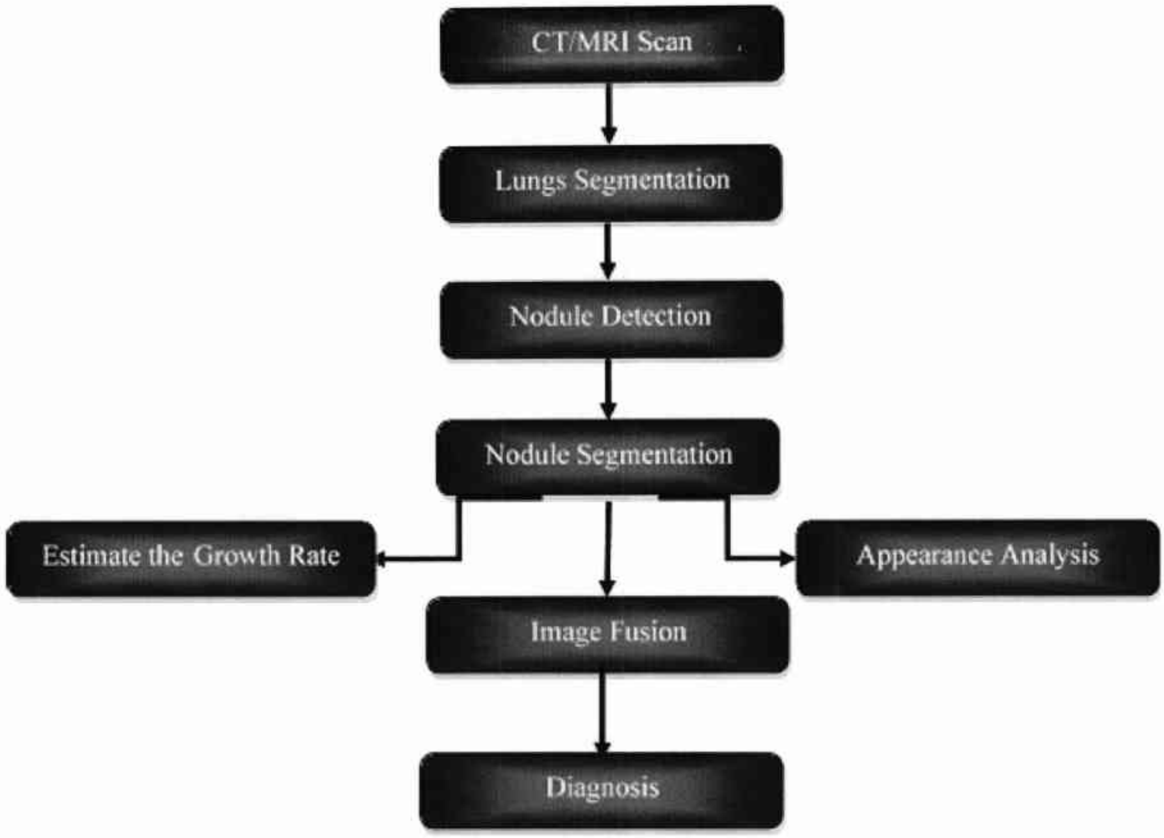

Figure 2.1: CAD system pipeline.

performance to improve diagnostic accuracy and quality in radiologist image interpretation.

The CAD (Figure 2.1)system addresses the problem of creating a computer-based system for extracting maximum features from a segmented suspicious region in a lung image, and these properties can be used to identify lung tumors as benign or malignant directly from the CT image [9]. The features help the CAD system take correct decisions in hard copy converted into soft and store for analysis and processing, then the system classifies the task.

2.2 Image Fusion Algorithms

Many image fusion methods have been implemented to use and compute various images efficiently, and research on such techniques has been ongoing for more than 20 years [29]. Because of their narrow depth-of-focus, optical focal points often produce images that occupy both in and out-of-focus areas [30]. The resultant image [31] has almost all required and useful information. Multiplication, addition, median and maximum functions are all used in traditional image fusion processes. Although such methods are effective, they are insufficient for accurately fusing multi-focus images [32]. These algorithms are classified into different categories which cover the majority of issues.

2.2.1 Algorithms using Dynamic Wavelets

In medical image fusion different parameters such as bones structures, tissues and veins are used [18]. Image fusion is a crucial and fundamental phase in reconstructive image evaluation, which includes medical images. Therefore, the contrast and structure perceptibly of such medical images are minimal. Using distinct contrast operators, a technique that improves image quality while reducing radiation measurement has been proposed in recent years [33]. In addition, image handling systems are designed to re-establish image information locally and globally using multi-scale edge maps [34]. For successful image fusion effects, wavelet modulus maxima are applied at various dimensions and transfer speeds [35]. Correlation information contained in adjacent pixels is adopted to fuse different bands. On the other hand, fusion is an important phase in which useful data from different modalities is combined.

Dual tree dynamic wavelet with shift-invariance and directional selective models are used to persist valuable data [36]. Minimum errors estimator and weight maps dependent filter are used to fuse noisy medical images like MRI and CT but the experimental choice of different parameters is crucial in concluding remarks [37]. By estimating the useful information data, pixel significance assigns weight to each pixel. The statistical properties of pixels and neighboring data are used to determine the importance of pixels [38]. However, such methods produce a variety of blurring objects.

The issues of fusing multi-focus images were discussed by Zhan et al. [39]. The concept of Phase Congruency (PC) is correctly applied. The target measure works as a robust Phase

Congruency near to a specific image function, that is evaluated using a complex Gabor wavelet. The decision map is created by comparing the PCs, and this determines fusion quality. The majority filter is used to complete each of these tasks. This fusion method delivers excellent results in physically and analytically. The guidelines for treating duplicate details from the image have not been thoroughly investigated, which could compromise the method's efficiency. This method's fusion efficiency can be improved by combining alpha mapping and Sum-Modified Laplacian (SML) gradients [40].

2.2.2 Algorithms using Neural Networks

A fusion approach was introduced by Yin et al. [41]. Using this method, source images are decomposed with the help of Non-Subsampled Shearlet Transform (NSST). A Parameter-adaptive pulse Coupled Neural Network(PCNN) is used to merge high-frequency input bands. The PCNN parameters are estimated adaptively using this band. Fusion based on NSST used image characteristics such as detailed details and enhances image features by contrast. However, this approach is not feasible since boundaries are blurred and edges are not demarcated. When used in conjunction with NSST, performance can be improved.

Using Convolutional Neural Networks (CNN), Liu et al. developed an image fusion technique [42]. A Siamese Convolutional Network (SCN) is used to compute a weight map in this technique. The weight combines the pixel behavior information from different input images. The decomposed coefficients modify the fusion process using a local similarity-based approach. When images have a high resemblance, it helps to avoid losing important information sources. This system, in combination with Deep CNN, can improve results.

Salient detection and multi-scale image decomposition were proposed for an image fusion technique by Bavirisetti et al. [43]. By combining multi-scale image decomposition and maximal symmetric salient detection, this technique addresses various issues that arise in multi-focus image fusion. In this fundamental technique, source images are evaluated using the average filter. This technique's weight map aids in locating oriented and refocused areas of the source images. The fused image incorporates sharp image information found in the source images. With this approach and a multi-scale morphological focus-measure, performance can be improved.

To fused medical images, Ramlal et al. implemented an image fusion scheme [44]. With the support of NSST, this scheme uses a simplified version of a PCNN for use in the medical field [44]. After decomposition, NSST extracts estimation and detail parts from the source images. This scheme employs an activity metric dependent on regional electricity. It aids in the verification of accuracy. This measure aids in the fusion of the NSST approximation components. Information components are used with PCNN to fuse with detail components and measure morphological gradient. The majority of the bone and edema specifics are retained using this process. Other types of filters, such as box filters, should boost fusion laws. Activity level calculation was conducted by Liu et al. combine a fusion rule with the CNN model's learning process. Deep CNN image fusion calculates a focus map and assigns weights to each pixel [45]. To identify a direct mapping between the centred measure and the source images, a deep learning methodology is applied. To encode the mapping data, a deep CNN is used next. Image stripes of varying consistency, as well as blurred images. This system was slow because it employed CNN and performed segmentation at different levels and failed to fuse multiple regions.

2.2.3 Algorithms using Different Filtering Methods

Zhan et al. developed a Fast Filtering Image Fusion (FFIF) method built on fast filtering and a structure-preserving mask [46]. The value of discrete gradient magnitude is employed in this approach to detect image quality. This process is further refined using a quick morphological filtering operation. For structure preservation, the mean and variance of the weight matrix are computed by using a filter. Furthermore, a structure-preserving filter is used in conjunction with a box filter to construct the weighted image in the spatial domain for further fusion process. This method is computationally effective and indifferent to the empirical collection of different constraints. Although, FFIF fusion still suffers from additional artifacts in various areas of the image. Performance can be improved by using majority filtering in conjunction with FFIF.

Bavirisetti et al. suggested a procedure for combining medical images [47]. In this process, the source medical images are MRI and CT brain images. This method extracts detail layers from each source image using directed filter and image statistics for fusion. These detail layers are used to calculate weights for each source image with the aid of image data. Weighted average method is applied on source images for the improvement of fusion process Although, it has been discovered that a procedure does not precisely fuse the desired image.

To fuse the source image, Kumar et al. used a weighted average. After processing the information files, this technique applies the weights obtained [48]. Cross Bilateral Filter (CBF) is used to calculate the weights from source images. These weights used to connect neighboring pixels of source images by using geometric closeness function and intensity resemblance for fusion process. The resultant image are obtained by subtracting the input image from the CBF's output image. By computing the intensity of detail elements, such images aid in calculating weights. CBF produces gradient artifacts in the fused image and takes longer to process in the fused image. To prevent objects like these, image fusion frameworks can be used. Although, the efficiency of this approach can be further investigated and enhanced when used in combination with other edge-preserving filters.

To study the behavior of speckle noise, Choi et al. developed an image fusion process [49]. This approach optimizes denoising efficiency by reducing the impact of speckle noise in ultrasonic images. This approach employs a technique known as Speckle Reducing Anisotropic

Diffusion (SRAD). SRAD filter detects the edges of diffusion. Without using logarithmic compression, SRAD is used for speckled images. With additive Gaussian noise, this filter is more efficient. However, the resultant edges are not physically consistent and do not meet industry standards. The SRAD filter's boundary conditions can be investigated further to improve the method's value. The optimum selection fusion criteria has been used to merge the high frequency coefficients. The fused coefficients used the inverse shearlet transform to compute the appropriate fused image. This approach has been successfully used to distinguish tumors correctly in images. However, the quantitative measure root mean square error remains strong, indicating that image information is still lost during the fusion process.

Shuaiqi et al. [50] proposed a fusion approach that incorporates a Rolling Guidance Filter (RGF) and a more accurate spiking cortical model (SCM). Fusion strategy provides a more robust noise-resistant fusion process. SCM aids the method's expansion in fusing various types of medical images. The salience of multimodal source images is first measured using RGF in this technique. To choose the self-adaptive threshold found in SCM, the mean and variance of the source images are used. Finally, SCM, powered by RGF coefficients, is used to obtain the fused image. This system, which is based on RGF and enhanced SCM, enhances the robustness of medical fusion analysis. However, when dealing with noisy images, the output of algorithm is minimal. For a careful analysis of deficiency in quantitative data, the joint filter method can be used for RGF and CBF.

A patch-wise image fusion method was proposed by Ma et al. [51]. This method makes use of the structure vector's path. This vector is used to construct the weighting mechanism, which allows for complex scenes to be considered. For various sequences of images, this algorithm produces good visual results. In the uniform regions, the color tends to be dull. The walls and window frames are examples of such areas. Quantitative analysis reveals that the algorithm achieves good results only for the cave and shape house source sequences. However, it is necessary to set a threshold for blocks in which flat regions are less relevant and decompose color image patch components into three conceptually redundant patches to speed up the algorithm.

The image self-similarity and the distance between the object and the focal plane were investigated by Guo et al. [52]. Adaptive regions are used in this technique. To decide the clarity, such regions are formed. These areas are reliant on the source images' joint uniformity. This technique ignores the blurring of one object in favor of making more genuine fusion decisions. The adaptive regions voting rule is then used to propose a weighting fusion rule to eliminate the blurring artifacts further. The separations between different objects, and the focal plane is combined in adaptive regions to improve visibility. Around margins and corners of the object, there are less artifacts. This approach, however, does not work as well as directed filtering and is computationally costly. To improve this technique, compute weights to assign each pixel a weightage, and outliers assigned minimum weights.

2.2.4 Algorithms using Image Decomposition

Alshawi et al. proposed a Bi-dimensional Empirical Mode Decomposition (BEMD) based medical image fusion process. BEMD-based fusion produces similar results to wavelet-based and curvelet-based fusion methods [53]. BEMD has a long computation time, limiting its utility, and it only fuses residues using the PCA law. However, other interpolation methods can improve the efficiency of the Fusion algorithm. If diagonal values for upper and lower envelopes are also considered, the size of Bi-dimenstional Intrinsic Mode Functions (BIMFs) can differ and common patterns between the two should be avoided. This method's accuracy can be improved by combining PCA and linear discriminant analysis.

Yang et al. [54] proposed an image fusion technique to solve various issues encountered in spatial and transform domain image fusion techniques, such as the difficulties encountered in sub-band coefficient selection in multiscale transform domain-based image fusion methods.

Blocking effects, which are induced by spatial domain image fusion, are discovered. For multi-focus image fusion, this technique employs NSCT, which recommends centered area recognition. Fusion decision map (detected by concentrated areas) aids fusion and improves fusion performance accuracy. However, additional artifacts can be introduced by the high-frequency sub-band coefficients. The Log-Gabor energy rule aids in the fusion of such bands. To reduce the influence of additional artifacts, the gradient approach should be applied to the average of low and high frequency sub-band coefficients.

An efficient quad tree decomposition strategy was implemented by Bai et al. [55]. The input images are segmented into different blocks, according to the strategy of the method. In a quad tree structure, each block is of optimal size. The tree structure employs a weighted focus-measure, which allows for detecting centered regions. To remove the centered areas, the source images must be used. Reconstructing these regions results in a fully focused picture. This algorithm is both efficient and straightforward because of the quad-tree decomposition method and the weighted focus measure. Quantitative findings, on the other hand, suggests that the system still needs to be improved. For images with soft tissues, such as MR images, the gradient similarity metric and the edge-based similarity metric should be checked.

An animated texture decomposition-based image fusion scheme was proposed by Liu et al. [56]. Texture and other material are separated from the input images. The improved iterative re-weighted decomposition collection of rules is used to apply the segmentation procedure. To fuse the texture and cartoon content, appropriate fusion rules are made. It has a high convergence rate and is very similar to the morphological structure components. The fused texture, and other components are combined to create the necessary fused image. This approach yields excellent visual results. On the other hand, up-sampling data are not adequately discussed in this scheme. The combination of morphological contents and gaussian saliency will increase efficiency even more.

2.2.5 Algorithms using Fuzzy Logic Techniques

Using MRI images, a multi-parametric segmentation approach for image fusion was proposed by Kazerooni et al. [57]. This approach employs the spatial fuzzy C-means clustering algorithm and the area increasing method. This approach takes into account the glioblastoma multiform tumor's fuzzy associated behaviors. In the presence of noise, this procedure yields good results. Additionally, this approach effectively distinguishes various areas. On the other hand, this system does not explicitly differentiate regions with low apparent diffusion coefficients, such as partially viable tumors, normal brain tissue, and edema. Each cluster has an ambiguous degree of pixel membership that can be improved by defocusing flat regions in MR images.

2.3 Lung Nodule Detection

The identification of lung nodule candidates in the automated diagnosis phase is important. The nodules are spherical structures with a round form ranging from 3 mm to 30 mm [58]. The nodules tend to be the brighter object in a CT scan, having dark surroundings and higher concentration at the core. The main goal of this stage is to detect the candidate set's all nodules with 100% sensitivity. The drawbacks of this method is to increase the high number of false positives results. A detection method's strength is determined by its sensitivity and low false positives. To classify objects, image features are crucial. An image comprises several pixel values, each with its own set of useful and related characteristics. Feature extraction is the process of extracting these values, and feature selection is selecting the most appropriate values from those extracted to represent an image best. Various machine learning classifiers [59] are used to classify nodules and non-nodules based on selected features. The wrong diagnosis will result from a poor selection of features. The efficacy of the feature selection and extraction procedure is shown by the fact that the correct feature selection increases the diagnostic device efficiency [60].

In recent years, automated diagnostic systems for lung cancer have remained a focus of study. These diagnosis systems have a major problem with sensitivity and false positives. Segmentation, feature extraction, and classification are the key components of lung nodule diagnosis methods [61]. Lungs area extraction and nodule candidate identification are two subsets of the segmentation. In addition, a standard dataset is important for evaluating the efficiency of a diagnostic system. Table 2.1 summarizes the various methods for detecting lung nodules automatically. This section categorizes the approaches suggested in these papers by innovation.

Table 2.1: Methods for detecting lung nodule

S.NO	Author	Feature Types	Detection Methods	Category	Year
1	daSilva Sousa et al. [62]	Texture features, Geometric features	thresholding, SVM	Hybrid Method	2010
2	Messay et al. [63]	Geometric, intensity and gradient features. and quadratic classifiers	Fisher Linear Discriminant (FLD) and quadratic classifiers	Supervised Learning	2010
3	Lee et al. [64]	Gray level values	Random forests based classification	Supervised Learning	2010
4	Lee et al. [65]	Geometric and texture features	Ensemble classification	Supervised Learning	2010
5	Chen et al. [66]	Texture, geometric	Neural network ensemble	Supervised Learning	2011

S.NO	Author	Feature Types	Detection Methods	Category	Year
6	Magalhães Barros Netto et al. [67]	Shape and texture	SVM classifier	Supervised Learning	2012
7	Cascio et al. [68]	Geometric and intensity	3D Mass-Spring Model	Supervised Learning	2012
8	Chen et al. [69]	Morphological features	Neural network	Supervised Learning	2012
9	Elizabeth et al. [70]	Shape and texture	Thresholding	Thresholding	2012
10	Teramoto and Fujita [71]	Shape and intensity	Thresholding, cylindrical nodule, enhancement filter	Hybrid Method	2013
11	Choi and Choi [16]	Geometric and texture features	Thresholding method for segmentation and SVM	Supervised Learning	2013
12	Wang et al. [72]	Texture and shape features	SVM based on three-dimensional matrix patterns	Supervised Learning	2013
13	Tartar et al. [73]	Morphological features and patient information	Decision tree	Supervised Learning	2013

S.NO	Author	Feature Types	Detection Methods	Category	Year
14	Keshani et al. [74]	2D stochastic and 3D anatomical features	Adaptive fuzzy thresholding and active contour models (ACM)	Supervised Learning	2013
15	Jang et al. [75]	2D and 3D features	Fuzzy clustering and genetic algorithm	Fuzzy Logic	2013
16	Choi and Choi [10]	Three-dimensional shape-based feature	Dot enhancement filtering/SVM	Supervised Learning	2014
17	Kuruvilla and Gunavathi [76]	Statistical parameters	Artificial neural network	Supervised Learning	2014
18	Cao et al. [77]	Intensity, shape, and gradient features	Ensemble learning	Supervised Learning	2014
19	de Carvalho Filho et al. [78]	Shape and texture	Thresholding based segmentation	Hybrid Method	2014
20	Badura and Pietka [79]	Texture features	Fuzzy connectedness and the evolutionary computation	Hybrid Method	2014
21	Brown et al. [80]	Shape features	Watershed, intensity thresholding and Euclidean Distance Transformation (EDT). A vector quantization (VQ)	Hybrid Method	2014

S.NO	Author	Feature Types	Detection Methods	Category	Year
22	Taşcı and Uğur [81]	Texture features	Otsu thresholding, morphological operations, generalized linear model regression (GLMR) classifier.	Thresholding	2015
23	Akram et al. [82]	Geometric and intensity based statistical features	Artificial neural network	Supervised Learning	2015
24	Wang et al. [83]	Shape features	Spherical shape enhancement filter, Chan–Vese (CV) model	Supervised Learning	2015
25	Kaya and Can [84]	Shape, size, and texture features	Ensemble classification	Supervised Learning	2015
26	Shi et al. [85]	Gray values	ROI extraction based on hessian matrix and Laplacian of Bilateral (LoB)	Unsupervised Learning	2015
27	Dai et al. [86]	No features	Graph cuts algorithm with Gaussian mixture models (GMMs)	Unsupervised Learning	2015

S.NO	Author	Feature Types	Detection Methods	Category	Year
28	Han et al. [87]	Geometric, intensity, gradient, and hessian features	Different levels of vector quantization for lung and nodule segmentation.	Unsupervised Learning	2015
29	Shen et al. [88]	Contextual features	Bidirectional chain Code,SVM	Hybrid Method	2015
30	Hua et al.[89]	Texture and morphological features	Deep belief network	Deep Learning	2015
31	Firmino et al. [90]	HOG features	Region growing, SVM and rule base classifiers	Supervised Learning	2016
32	Nibali et al. [91]	Deep convolutional features	Deep residual learning, curriculum learning, and transfer learning	Deep learning	2017
33	Dou et al. [92]	Deep convolutional features	multi-level 3D CNN	Deep learning	2017
34	da Silva et al. [93]	Deep convolutional features	Deep learning and genetic algorithms.	Deep learning	2017
35	Sun et al. [94]	Shape, texture and deep features	CNN, DBN, Autoencoder	Deep learning	2017
36	Gupta et al. [95]	Shape, texture and intensity features	Neural network classifier	Supervised Learning	2018

S.NO	Author	Feature Types	Detection Methods	Category	Year
37	Zhang et al. [96]	Morphology based 3D skeletonization feature, shape feature and intensity features	ACM, thresholding, morphological operation,, SVM	Morphology Based	2018
38	Jaffar et al. [97]	Intensity and gradient	Differential evolution based thresholding	Hybrid Method	2018
39	Ali et al. [98]	Deep features	Reinforcement learning based deep neural network	Deep Learning	2018
40	Jiang et al. [99]	Deep features	Four channel CNN, Frangi filter	Deep Learning	2018
41	Li et al. [100]	Deep features	CNN-ensemble	Deep Learning	2018
42	Huidrom et al. [101]	Shape, intensity and gradient features	Neural Network optimized with GA and PSO	Supervised Learning	2019
43	Shaukat et al. [102]	Shape, texture and intensity features	ANN, thresholding and watershed segmentation	Supervised Learning	2019
44	Xie et al. [103]	Deep features with RCNN	R-CNN and Boosting CNN	Deep Learning	2019
45	Kasinathan et al. [104]	Deep features	ACM, enhanced AlexNet	Deep Learning	2019

S.NO	Author	Feature Types	Detection Methods	Category	Year
46	Pan et al. [105]	Feature extraction	3D CNNs	Deep Learning	2020
47	Paranathi et al. [106]	Deep Feature	Image enhancement, image segmentation, Feature extraction	Deep Learning	2020
48	Khan et al. [107]	Feature Fusion and selection	Contrast perfection, multiple feature extraction. DWT along with geometric features	Deep Learning	2020
49	Abdullah et al. [108]	extracting features images	Image Processing and k-Nearest Neighbors.	Deep Learning	2020

2.4 Discussion and Analysis

The present study of lung nodule detection methods focuses primarily on recent methods. These methods are evaluated using several criteria, including accuracy, nodule size, datasets, and nodule forms. A diagnostic system's primary goal is to identify and classify nodules with high sensitivity and a low number of false positives. Due to the various criteria used during their study, comparing the soundness of different methodologies is a difficult task. For example, it is unjustifiable if two diagnostic systems produced findings on different datasets based on different kinds of nodules and sizes. These techniques, however, were unable to resolve the rate of false positives. While Keshani et al. [74] achieved 89% sensitivity, their findings were based on a dataset with only large nodules larger than 5 mm in size. These detection techniques have a deficiency in achieving the significant accuracy rate and reducing the false positive ratio in juxta-vascular nodules because of the smaller size of nodules. The drawbacks of modern approaches are shown in Table 2.2. These problems are due to the complex nature of the human lung.

Table 2.2: Constraints in newly developed techniques

S.NO	Year	Techniques	Limitation
1	2013	Keshani et al. [74]	Multiple diseases were treated with features of the same type, resulting in poor performance.Low sensitivity (89%) and high FPs/scan (7.3), multiple diseases were handled with features of the same type, resulting in poor performance.
2	2013	Choi and Choi [16]	For performance assessment, a subset of the dataset was used.
3	2014	Choi and Choi [10]	The evaluation was performed on a subset of the dataset containing 148 nodules,which resulted in a high false positive rate of 6.67 per scan.
4	2014	Kuruvilla and Gunavathi [76]	There were no other features used except statistical ones. 30 false positives per scan is an extremely high rate.
5	2014	Cao et al. [77]	There were no false positives found and achieved 85% accuracy .

S.NO	Year	Techniques	Limitation
6	2015	Wang et al. [83]	Only the false positive rate is stated in terms of performance measurement. A standard dataset was not used to assess the system's performance.
7	2015	Shen et al. [88]	Only accuracy is considered when judging a process. It only dealt with nodules in the juxta-pleural room.
8	2015	Kaya and Can [84]	Sensitivity is just 82 percent. The number of FPs has not been published.
9	2015	Hua et al. [89]	The results were poor, with a sensitivity of 73% and a specificity of 82%. No mention of FPs. The features aren't well-explained. The method isn't put to the test on a regular dataset.
10	2015	Taşcı and Uğur [81]	The accuracy of the method was assessed. Only juxta-pleural nodules were taken into consideration.There was only one form of function used. The FP was not registered.
11	2016	Firmino et al. [90]	For classification, only one feature category was used. Characteristics of HOG
12	2017	Nibali et al. [91]	The fusion of a large number of deep features increases the complexity of the image.it's time to compute FPs aren't even registered.
13	2018	Zhang et al. [96]	A subset of the LIDC-IDRI dataset of 71 scans with 168 nodules was used.

S.NO	Year	Techniques	Limitation
14	2019	Huidrom et al. [101]	The output was assessed over 300 scans, but no information about the nodules is given. Furthermore, there was no information about the amount of FP.
15	2019	Shaukat et al. [102]	To remove the lung ROI, a simple thresholding was used. The juxta-pleural nodules are missed as a result. 84 scans were used to assess the process.
16	2019	Xie et al. [103]	Since the nodule detection is based on 2D properties,the diagnosis is incorrect. As a result, sensitivity drops to 83 percent, while FPs spike to 8 per scan.
17	2020	Abdullah et al. [108]	The fusion of a large number of deep features increases the complexity of the image.
18	2020	Pawer et al. [109]	The objectives of the study are up-to the mark and there is still a need to improve accuracy.
19	2021	Li et al. [110]	The only thing that was done is to enhance the fusion performance in terms of visual quality and variety of quantitative evaluation parameters.

Chapter 3

Efficient Pre-Processing and Segmentation for Lung Cancer Detection Using Fused CT Images

In this chapter, an algorithm based on image fusion for lung segmentation to improve lung cancer diagnosis was proposed.The Laplacian Pyramid (LP) decomposition and Adaptive Sparse Representation (ASR) methods were used to develop the image fusion methodology. Using the LP, the proposed fusion approach divides medical images into several sizes. The four decomposed layers were fused using LP method at this stage. SVM was used for the nodule detection and classification. The Lungs Image Database Consortium and Image Database Resource Initiative (LIDC-IDRI) were used to evaluate the proposed approach.

3.1 Introduction

Cancer is one of the most dangerous types of disease, spreading day by day across the globe. One of the main causes of death is lung cancer. The presence of cancer poses the greatest risk of complications and death. The underlying causes of cancer are not wholly known, which results in the frequent occurrence of the disease. According to the World Health Organization fact sheet, cancer is ranked as the leading cause of death globally. Cancer caused approximately 10 million casualties in 2020 alone, while more than 70% of the deaths occurred in low- and middle-income countries. Surprisingly, lung cancer is the most commonly occurring disease, with 2.21 million cases identified, leading to the death of 1.80 million. However, early detection of lung cancer can significantly help decrease the death toll while saving the lives of many people. The advancement of technology has considerably helped cancer diagnosis with commonly used techniques such as Magnetic Resonance Imaging (MRI), CT scans, X-rays, Positron Emission Tomography (PET), lung biopsy, High-Resolution Computed Tomography (HRCT), etc. The advancement of CT innovation has caused a remarkable expansion in the measurement of information in clinical CT. The development of a Computer-Aided Design (CAD) systems for lung segmentation and fusion depends on computer vision and medical imaging technology.

Lung parenchyma segmentation is used as a pre-processing phase in lung CT image processing, in particular in lung disease. The pre-processing stages have a direct impact on the resultant image preparation. Subsequently, quicker and more exact segmentation strategies for lung CT images are an intriguing issue worthy of exploration, having urgent reasonable importance and clinical worth. Investigations have considered numerous lung division strategies, and a portion of the ordinary methodologies incorporate threshold region-developing techniques [111]. Regardless, the findings are not exceptionally encouraging, and the process is convoluted and repetitive. As a result, it is still an unexplored territory. The process of division is quick, yet not good on the grounds that the dimension estimations of the lung boundaries are the same as the windpipe and bronchus region. Deep learning [112] is a basic image-segmentation technique dependent on area. It can isolate the interstitial lung boundaries rapidly and effectively. This technique, however, is time consuming, and the emerging model is sensitive to boundaries. At present, most lung segmentation frameworks utilize blended systems dependent on the edgerespecting strategy along with unforeseen provincial development and other extraction procedures. In addition, various examinations are based on the division of lung parenchyma with a lung infection. Pu et al. [113] anticipated a robotized division method dependent on a two-dimensional versatile line walking assessment to supervise juxtapleural nodules (injuries lining the chest divider and mediastinum). Senthil et al. in 2019, proposed various evolutionary algorithms for lung segmentation [114]. Four algorithms were applied to the pre-processed images with enhanced quality. MATLAB was used to verify the realistic results for 20 sample of lung images, and it was discovered that the Guaranteed Convergence Particle Swarm Optimization (GCPSO) had improved the accuracy. Moreover, in 2020, Akhter et al. [115] worked on lung cancer detection using enhanced segmentation accuracy. This study developed an algorithm that uses median values measured along each row and column, in addition to maximum and minimum values, and found that this approach improved the accuracy of the segmentation of these images. The sensitivity, specificity, precision, and accuracy of the proposed methodology were significantly high with a lower false-positive rate.

Image fusion is the mixture of appropriate data from different input images into one clarifying fused image. Therefore, image fusion is the mixing and integration of desired information from a set of registered images for clarity and alteration-free features. Spatial-Domain (SD) and Transform-Domain (TD) based image fusion methods are the two categories into which image fusion techniques may be separated based on their mode. Both spatial-area-based and transform-domain-based algorithms can be used to realise image fusion; however, the latter can also intentionally apply different fusion rules to improve the fusion effect while the former is less robust and sensitive to noise. This allows the latter to overcome the aforementioned challenges [116]. Diverse medical modalities for imaging exist with each has its exceptional qualities. This also helps for different processing techniques and adds a valuable data source.

Multi-scale image fusion is a well-known and commonly used technique. Multiple medical images are fused using this process. Pyramid Fusion (PF), DWT, CVT, NSCT and several other multi-scale image fusion algorithms are currently in use. The above methods are based on extracting potentially useful knowledge from modified parameters. After fusing the derived details by measuring the parameters, detailed relevant information along with the fused image are acquired. A natural signal sparsity analysis technique, Sparse Representation (SR) has been proposed to improve the capacity of the human visual system in image processing. SR theory is now commonly used in image-processing applications such as image super-resolution processing, denoising, and fusion. In recent years, SR theory has received much attention in the image-processing field, especially in image fusion. It is very well known that the dictionary development of the algorithms of classical SR can be performed in one of two ways: analytical methodologies (such as wavelet decomposition) or learning-based methodologies, such as as Singular-Value Decomposition (K-SVD) and DL-GSGR [117].

Traditional SR algorithms that use a fixed dictionary, on the other hand, have several drawbacks in the image fusion process. Liu et al. [118] suggested an adaptable compressed dictionary may be created using ASR for image fusion and denoising. Aishwarya et al. [119] applied the adjusted spatial frequency to image fusion and tried to explain the SR fundamentals of an adaptive selection dictionary. In 2015, Singh and Khare [120] investigated an image fusion method for multi-view medical images based on Redundant Wavelet Transform (RWT). Their proposed method found that quality image fusions can be produced through the shift-invariance of the Redundant Discrete Wavelet Transform (R-DWT) method. Numerous multimodal MRI, CT, and PET medical images have been used for experiments, and the results were analyzed using mutual information and strength metrics [121]. Pyramid transformation is a technique that can be used to accomplish the fusion of multi-view images. This method was initially introduced, it was mostly used in image compression, segmentation and computer vision [122]. Presently, the pyramid transform was being extensively used to combine multi-view clinical images. The method of the union LP was proposed by Du et al. [123] to extract many important features, which helped to enhance the outline structure and color contrast of the fused images. To fuse the images captured by a microscope, Kou et al. [124] suggested Region Mosaicking on Laplacian Pyramids (RMLP), but it was found to be vulnerable to noise. Then, it was proposed to use the LP method, which showed the image's rich background features and also included joint averaging. Li and Zhao in 2020 [125] worked on a novel algorithm for combining multi-modal medical images. In their study, firstly, CT and MR images were decomposed into low and high-frequency sub-bands using the Non-Subsampled Contourlet Transform (NSCT) of multi-scale geometric transformation; second, the local area standard deviation method or fusion was selected for the high-frequency sub-band, while an adaptive pulse coupling neural network model was developed for the low-frequency sub-band. The algorithm's fusion findings in this work greatly improved the accuracy of image fusion and had benefits for both visual effects and objective evaluation indices, offering a more reliable foundation for clinical illness diagnosis and treatment. Moreover, Soliman et al. worked on accurate lung segmentation of CT chest images by adaptive appearance-guided shape modeling and reported a high DS, Bidirectional Hausdorff Distance (BHD), and Percentage Volume Difference (PVD) accuracy of our lung segmentation framework on multiple in vivo 3D CT image datasets [126].

Khan et al. in 2020 also worked on an integrated design of contrast-based classical feature fusion and selection [107]. Firstly, the gamma correction max intensity weight approach improves the contrast of the original CT images. Secondly, multiple texture, point, and geometric features are extracted from the contrast images, and then a serial canonical correlation-based fusion is performed. Finally, an entropy-based approach is used to substitute zero values and negative features, followed by weighted Neighborhood Component Analysis (NCA) for selection. The Lung Cancer Data Science Bowl (LDSB) 2017 achieved a maximum accuracy. Similarly, in 2021, Azam et al. a multi-modal registration and merging of medical images is suggested for quality improvement [127]. The HARVARD dataset's CT and MRI imaging modalities were used to validate the suggested method. Quality evaluation measures including MI, NCC, and FMI were produced for the statistical comparison of the suggested system. The suggested technique yielded more precise outcomes, higher image quality, and useful data for medical diagnosis.

Orozco et al.[128] proposed lung noudule classification method in CT images without segmentation. After being trained with the retrieved characteristics, SVM was applied to classify nodule candidates into nodules and non-nodules and achieved the 84% accuracy. A SVM-based classification of lung nodules employing hybrid characteristics from CT images was proposed by Akram et al. in 2016[129]. The classifier was trained using the 2D and 3D geometric and intensity-based statistical characteristics that were acquired. The system claims to have a sensitivity of 95.31% without FP/scan results.

Recently, the American Cancer Society noted that there is a high likelihood of more severe COVID-19 in cancer patients, recommending that patients and their care-givers be required to take special precautions to reduce the risk of contracting the disease. This new type of coronavirus is SARS-CoV-2. Beta-coronavirus is a primary cause of Acute Respiratory Syndrome (ARS). In this regard, lung cancer is closely linked with ARS because it is a part of a disease group based on the progression and expansion of abnormal cells within the human body. American scientists have analyzed the course of COVID-19 in patients with cancer. Therefore, the diagnostic and examination features are of particular importance, since it includes determining the causative agent of infectious disease and the main leading indicators, determining the severity of the clinical images, the prognosis, the nature, and the amount of medical care [130].

In this dissertation, we propose a lung image segmentation and fusion method. The segmentation method is based on an approach by which we optimize the computational time of CT image segmentation with the help of a very effective known method, the adaptive global threshold. The proposed algorithm also incorporates morphological operations and masking, which have proven very helpful in CT image segmentation e.g. environments, this allowed us to decrease computation times while maintaining accuracy and removing the requirement for post-processing activities and operations. Based on the LP and ASR [131] techniques of image fusion, the lung fusion method produces a better outcome and a more effective way of medical image fusion in the treatment of lung cancer [42]. To improve up the construction of the sub-dictionaries using the ASR approach, we applied LP decomposition for the multi-view clinical CT images.

3.2 Background of the Theory

In this section, we review various image fusion methods for multi-view images.

3.2.1 Sparse Representation Method

Several SR-based fusion approaches have been studied in recent years [132]. According to Zhu et al. [133], image patches were generated using a sampling approach and classified by a clustering algorithm, and then, a dictionary was constructed using the K-SVD methodology. A medical image fusion scheme based on discriminative low-rank sparse dictionary learning was proposed by Li et al. [134]. Convolutional-sparsity-based morphological component analysis were introduced by Liu et al. in 2019 [135] as a sparse representation model for pixel-level medical image fusion.

In the SR method, various small dictionary items were used to linearly explain the natural signals. Since SR can only reflect natural images in a limited way, it has recently been widely utilized in different fields. Nevertheless, the use of SR in the fusion methods differs significantly from that of other areas. As a result, we expect an over-complete dictionary SR to show the signal $y \in W^x$ [136]. The SR can be depicted as follows:

$$y = \mathbf{E}\alpha \tag{3.1}$$

where $\mathbf{E} = [e_1, e_2, e_3, \ldots, e_M] \in W^{N \times M}(N < M)$ with e_i as the dictionary particle, which shows the matrix of SR, and $\alpha_i = [\alpha_1, \alpha_2, \alpha_3, \ldots, \alpha_M]^T$ is the set of sparse coefficients. $\mathbf{E}$ has over-complete features; as a result, Equation (3.1) has an infinite number of solutions. This procedure aims to find a single solution vector θ_i which contains the solution with the vector with most zero values. Normally, we choose the largest l_1-norm rule to fuse $\{\alpha_i\}$. The $\{\alpha_i\}$ is found by the following equation:

$$\arg\min_{\alpha} \|y - \mathbf{E}\alpha\|_F^2 + \lambda \|\alpha\|_1 \tag{3.2}$$

where λ has a major impact on sparsity. When λ is large, this indicates that the sparse error will be significant; if λ is small, the final error would also be reduced.

3.2.2 Image Decomposition Based Fusion Methods

A novel multi-component fusion method has been presented to generate superior fused images by efficiently exploiting the morphological diversity features of the images and the advantages [137]. Maqsood and Javed [138] proposed a two-scale Image Decomposition (ID) and sparse representation method for the integration of multi-modal medical images in 2020.

3.2.3 Deep Learning Based Fusion Methods

Several DL-based fusion approaches for multi-modality image fusion have recently been developed. Gao et al. [139] studied the use of a deep network for creating an initial decision map in a CNN for multi-focus image fusion. Li et al. [140] developed a DL architecture for multi-modality image fusion in 2018, which included encoder and decoder networks. Zhang et al.

[141] proposed the general Image Fusion Framework based on a Convolutional Neural Network (IFCNN) (2020), which is a broad multi-modality image fusion framework based on CNNs. The performance of these DL-based fusion algorithms has been proven to be competitive. For the merging of images with different resolutions, Ma et al. [142] proposed a Dual-Discriminator conditional Generative Adversarial Network (DDcGAN) in 2020.

3.2.4 Rolling Guidance Filtering

The Rolling Guidance Filtering (RGF) algorithm, which is an edge-preserving smoothing filter, was presented by Zhang et al. [143] in 2014. Rolling guidance was implemented using RGF in an iterative way, with rapid convergence characteristics. RGF can totally manage the detail smoothing under the scale measure, unlike other edge-preserving filters. Small structure removal and edge recovery are the two main methods in RGF.

3.2.5 Dictionary Learning

Aishwarya and Thangammal [119] proposed a multi-modal adaptive dictionary learning system for fusing the medical images. In order to learn a dictionary, useful information blocks were segregated by deleting zero information blocks and estimating the remaining image patches with a Modified Spatial Frequency (MSF).

The creation of an overly comprehensive lexicon has a significant effect on SR. There are two basic approaches to creating an over-complete dictionary. Firstly, pre-setting a transformation matrix is one procedure, for example contourlet transform and DCT. This method yields a dictionary that is fundamentally unchanged. Although the multi-source images have various attributes, a consistent sparse dictionary to fuse the images could result in poor performance. Secondly, a dictionary can be created based on training algorithms like the PCA and K-SVD approaches. This generates a dictionary from the source image's structure, allowing the trained or prepared particles to address the original image more sparsely. As a result, the dictionary produced by the latter method has better execution and efficiency, making it more appropriate for clinical image fusion. Now, look at how to use the dictionary to train the atoms. We say that ${x_i}^e{}_{i=1}$ is the database sample we obtain via a window with a defined size $(\sqrt{n} \times \sqrt{n})$, where e stands for the number of samples and n for the number of sampling databases. A random sample is taken from a collection of multiple-view clinical images by the window. The **E** learning model from the dictionary is describes as follows:

$$\min_{E,\alpha_i} \sum_{i=0}^{M} ||\alpha_{i0}|| \quad : ||x_i - E\alpha_i||_2 < \varepsilon \tag{3.3}$$

where $\varepsilon > 0$ is the tolerance factor and number of multi-view clinical images is represented by M.

3.2.6 Laplacian Pyramid Method

Liu et al. [42] proposed a deep-learning technique for medical image fusion. The strategy uses the Laplacian pyramid to reconstruct the image in the fusion process after generating a weighted map of the source image using the deep network. Chen et al. [131] defined the Laplace pyramid to describe the lost high-frequency detail information caused by the convolution and down-sampling operations in the Gaussian Pyramid (GP) method.

The LP technique is used to split up a images as input into a series of multi-scale, layer and pyramid shaped images [144]. This technique breaks down medical images that can distinguish between useful data and clinical images. The LP method decomposes an image into a pyramid of images of progressively lower resolution. Images in the bottom layer are high-resolution while those in the top layer are low-resolution, with the size of the lower image being four times that of the higher image. The resulting decomposed images have a neat appearance. In the LP technique, a layer of the GP is created using the contrast between its two levels for processing information at different frequencies by different layers. The first pyramid decomposition in the LP decomposition process is GP decomposition, which loses some high-frequency data due to the convolution and down-sampling operations. The following are the steps involved in image decomposition:

The input images are used to create the initial GP (multi-view medical images). A 5×5 2D separable Gaussian filter $\omega(m \times n)$ is used to convolve the source images and build P_l by down-sampling from layer to layer, where l is represented current layer, and layer's row count is represented by W_l, which is current row count of l-th layer:

$$P_l(i,j) = 4 \sum_{m=-2}^{2} \sum_{n=-2}^{2} \omega(m,n) P_{l-1}(2_i + m, 2_j + n);$$

$$for\ (0 < l \leq L,\ 0 \leq i < W_l,\ 0 \leq j < C_l) \tag{3.4}$$

The GP obtained in the previous step constructs the corresponding LP. The $(l+1)^{th}$ layer P_{l+1} is taken away from the l^{th} layer P_l after up-sampling and Gaussian convolution, and the difference is LP's l^{th} layer P_l. From the bottom layer to the top layer, the LP is constructed as follows:

$$P_l^*(i,j) = 4 \sum_{m=-2}^{2} \sum_{n=-2}^{2} \omega(m,n) * P_l(\frac{i-m}{2}, \frac{j-n}{2})$$

$$\text{for } (1 \leq l \leq N,\ 0 \leq i < W_l,\ 0 \leq j < C_l) \tag{3.5}$$

$$L_l = \begin{cases} P_{l+1} - P_l^* & : 0 \leq l < N \\ P_l^* & : l = N \end{cases} \tag{3.6}$$

where:

$$P^*{}_l(\frac{i-m}{2}, \frac{j-n}{2}) = \begin{cases} P_l(\frac{i-m}{2}, \frac{j-n}{2}) & : \text{if} \frac{i-m}{2}, \frac{j-n}{2} \text{ are integers} \\ 0 & : \text{otherwise} \end{cases}$$

The corresponding GP for the fused LP can be restored layer by layer from top to bottom, resulting in the source image P_0. The preceding indicates that the interpolation method will be used at the start. The inverse LP transform is defined as follows:

$$\begin{cases} P_N = \mathrm{LP}_N, & : l = L \\ P_l = \mathrm{LP}_l + P^*_{l+1} \end{cases} \tag{3.7}$$

3.3 Materials and Methods

In this section, the proposed technique for the image segmentation, fusion and reconstruction of the fused image is represented.

3.3.1 Image-Segmentation Method

Lung parenchyma segmentation is significantly helpful in locating and analyzing the nearby lesions, but it requires certain methodologies and frameworks. In the CAD system of lung nodules based on CT image sequences, lung parenchyma segmentation is an important preprocessing stage. We used an optimal thresholding method to reduce the complexity of lung segmentation in the quest to improve the computational time and accuracy. The approach was applied with the help of experimentation on several CT images taken from the LIDC-IDRI. The flowchart of the proposed segmented method is given in Figure 3.1. All the steps of the proposed segmentation technique are also summarised in Algorithm 1.

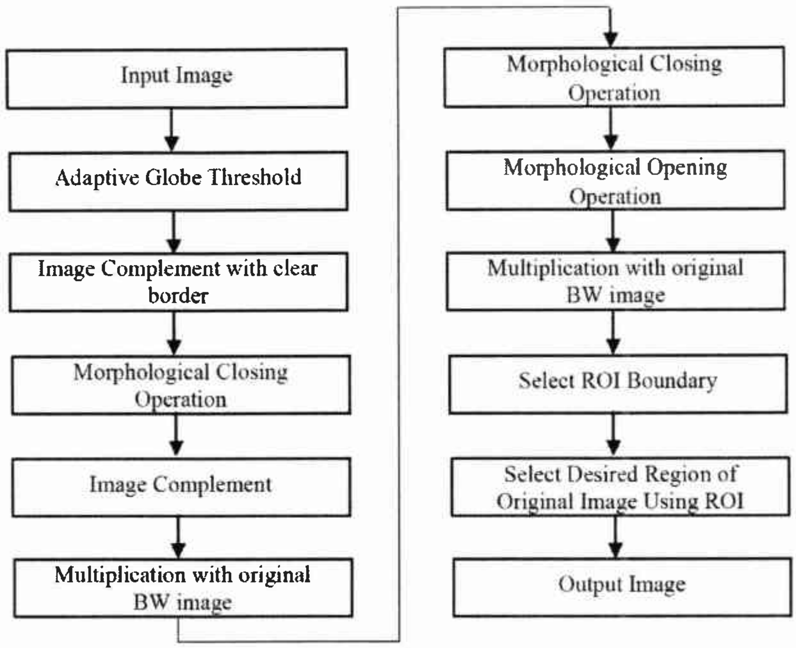

Figure 3.1: Flowchart of the proposed segmentation method.

Let $A(x,y)$ be the input CT image of the lung. The adaptive global threshold was used to perform the segmentation of the lung through intense thresholding of the region of the lung segment from the CT image. Then, the threshold value was picked from the CT image histogram to provide the output.

$$A^{\delta}(x,y) = \begin{cases} 1 & \text{if } A(x,y) \geq \sigma \\ 0 & \text{if } A(x,y) < \sigma, \end{cases} \tag{3.8}$$

where σ is the specific global threshold value applied to original input image $A(x,y)$. After applying thresholding on $A(x,y)$, we obtain the resultant image $A^{\delta}(x,y)$.

Now, we will obtain the image complement to the clear border by using following equation:

$$A^{c}(x,y) = C - A^{\delta}(x,y), \tag{3.9}$$

where C is an image with all pixel values equal to 1. The morphological closing operation is performed on $A^c(x,y)$ by using the mask B:

$$A^{\beta}(x,y) = A^c(x,y) \bullet B \tag{3.10}$$

Now, taking the complement of $A^{\beta}(x,y)$:

$$A^{\gamma}(x,y) = C - A^{\beta}(x,y) \tag{3.11}$$

Now, from Equation (3.8), the binary image $A^{\delta}(x,y)$ is multiplied with image $A^{\gamma}(x,y)$ from Equation (3.11):

$$A^{\tau}(x,y) = A^{\gamma}(x,y)A^{\delta}(x,y) \tag{3.12}$$

Morphological closing is applied on $A^{\tau}(x,y)$ from Equation (3.12) by using the mask B (structuring element):

$$A^{\theta}(x,y) = A^{\tau}(x,y) \bullet B \tag{3.13}$$

In the next step, the morphological opening operation is applied on $A^{\theta}(x,y)$ by using SE B:

$$A^{\omega}(x,y) = A^{\theta}(x,y) \circ B \tag{3.14}$$

In the last step, the output segmented image $\mu(x,y)$ is generated by multiplying $A^{\omega}(x,y)$ from Equation (3.14) with $A^c(x,y)$ from Equation (3.9) as shown below:

$$\mu(x,y) = A^{\omega}(x,y)A^c(x,y) \tag{3.15}$$

Algorithm 1 Proposed segmentation algorithm.

Input: Input image $\rightarrow A(x,y)$
Output: Segmented image $\rightarrow \mu(x,y)$
Initialization: Thresholding value $\rightarrow \sigma$
Structuring Element/Mask $\rightarrow B$

Procedure

$[M,N] \leftarrow size(A(x,y))$
$C \leftarrow ones(M,N)$
if $A(x,y) \geq \sigma$ **then**
  $A^{\delta}(x,y) \leftarrow 1$
else
  $A^{\delta}(x,y) \leftarrow 0$
end if
Image complement:$A^{c}(x,y) \leftarrow C - A^{\delta}(x,y)$
Closing operation:$A^{\beta}(x,y) \leftarrow A^{c}(x,y) \bullet B$
Image complement:$A^{\gamma}(x,y) \leftarrow C - A^{\beta}(x,y)$
$Multiplication: A^{\tau}(x,y) \leftarrow A^{\gamma}(x,y)A^{\delta}(x,y)$
Closing operation:$A^{\theta}(x,y) \leftarrow A^{\tau}(x,y) \bullet B$
Opening operation:$A^{\omega}(x,y) \leftarrow A^{\theta}(x,y) \circ B$
$\mu(x,y) \leftarrow A^{\omega}(x,y)A^{c}(x,y)$

End procedure

3.3.2 Image Fusion Method

In this section, the proposed image fusion algorithm is presented. The proposed method has three steps, as shown in Figure 3.2: decomposition of the source segmented image, hierarchical fusion, and image reconstruction. The complete proposed fusion method is also summarised in Algorithm 2 .The method of LP decomposition is used to decompose each multi-view medical image into proposed four layers in the initial step. The next step is to build a dictionary for each layer, which is then fused using the ASR method in sequence. The last step is to reconstruct the resulting image using the inverse LP transform.

Algorithm 2 Proposed fusion algorithm.

Input: Input image $\rightarrow \mu(x,y)$

Output: Fused image $\rightarrow I_F$

Procedure

$P_0 \leftarrow \mu(x,y)$

for $1 \leq l \leq 3$ **do**

  $P_l \leftarrow \Downarrow (P_{l-1})$

  $P_l^* \leftarrow \Uparrow (P_l)$

  if $0 < l < 4$ **then**

    $LP_l \leftarrow P_l - P_l^*$

  else

    $LP_L \leftarrow P_l$

  end if

end for

Sub-dictionaries $\leftarrow \{E_0, E_1, E_2, \ldots, E_k\}$

Sliding window size $\rightarrow \sqrt{n} \times \sqrt{n}$

Patch Size:$e \leftarrow (M - \sqrt{n} + 1) \times (N - \sqrt{n} + 1)$

Set of patches:$\{s^i{}_1, s^i{}_2, \ldots, s^i{}_J\}_{i=1}^{e}$

$\{v_1^i, v_2^i, \ldots, v_J^i\}_{i=1}^{e} \xleftarrow{Sorting} \{s^i{}_1, s^i{}_2, \ldots, s^i{}_J\}_{i=1}^{e}$

Zero-mean vector:$\hat{v}_j^i \leftarrow v_j^i - \bar{v}_j^i.1$

Gradient orientation histogram: $\{\theta_0, \theta_1, \theta_2, \ldots, \theta_K\}$

$\theta_{max} \leftarrow \max\{\theta_0, \theta_1, \theta_2, \ldots, \theta_K\}$

$k^* \leftarrow argmax\{\theta_k | k = 1, \ldots, K\}$

$\max_{\alpha_j^i} \|\alpha_j^i\| \leftarrow \|\hat{v}_j^i - E_{k_i}\alpha_j^i\|_2 < \sqrt{n}C\sigma + \varepsilon$

$\alpha_F^i \leftarrow \alpha_{j^*}^i$

$j^* \leftarrow arg\ max_j\{\|\alpha_j^i\|_1, \quad j = 1, 2, \ldots, J\}$

$\bar{v}_F^i \leftarrow \bar{v}_{j^*}$

$v_F^i \leftarrow E_{k_i}\alpha_F^i + \bar{v}_F^i\ .1$ (Fused result of layer)

$P_{F_{l-1}} \leftarrow P_{F_l}^* + LP_{F_{l-1}} \qquad (0 \leq l < 4)$

$I_F \leftarrow P_F$

End procedure

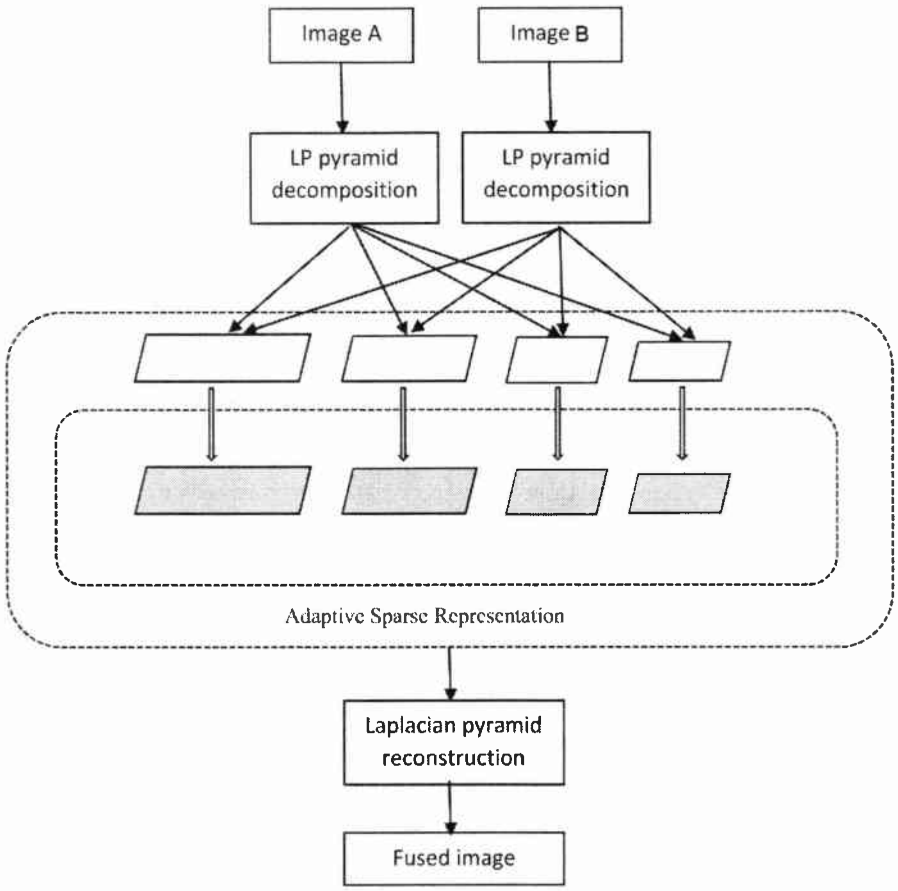

Figure 3.2: Laplacian pyramid and ASR-based fusion algorithm.

3.3.2.1 Decomposition of the Segmented Source Image

To obtain the features of segmented source images $\mu(x,y)$ at various sizes, the LP decomposition technique was applied. First, we need the Gaussian pyramid of an image of size $M \times N$. The source image was on the P_0 layer. To obtain the P_1 layer $(0.5M \times 0.5N)$, the image $\mu(x,y)$ from layer P_0 was down-sampled with the help of the Gaussian kernel function. By repeating the above steps, the LP decomposition was formed. The three stage decomposition of an LP is shown in Figure 3.3. The decomposition of the $(l-1)^{th}$ layer P_{l-1} into the l^{th} layer P_l can be expressed as follows:

$$P_l = \Downarrow (P_{l-1}) \tag{3.16}$$

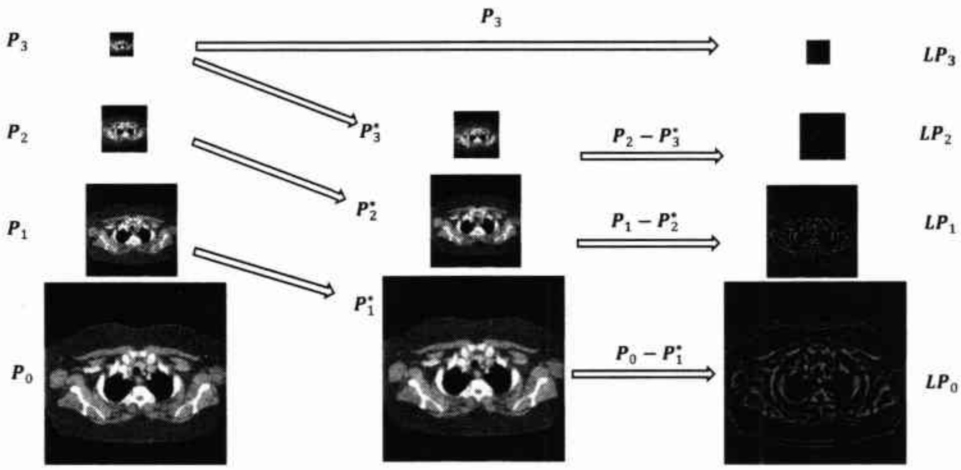

Figure 3.3: Decomposition using the Laplacian pyramid.

Each layer of the Gaussian pyramid is sampled in order to create the LP. The image to be enlarged is considered to be $m \times n$ in dimension. An inverse Gaussian pyramid was used to extend the image into a $2m \times 2n$ image, which can be interpreted as:

$$P_l^* = \Uparrow (P_l) \tag{3.17}$$

Now, the reconstruction of image $\mu(x,y)$ can done from the Laplacian pyramid layers as shown below:

$$\mu(x,y) = \begin{cases} P_0; & for\, l = 0 \\ P_l^* + LP_l; & for\, 0 < l < L \\ P_l = LP_l; & for\, l = L \end{cases} \tag{3.18}$$

where L is the total number of LP layers.

3.3.2.2 ASR Method

After decomposing, the ASR method fuses the two groups (LP_0 to LP_3) of two source images [145]. As shown in Figure 3.4, the most critical step in ASR is selecting and composing the adaptive dictionary. The segmented source images are represented by $\{\mu_1, \mu_2, \dots, \mu_j\}$, and all have the same $M \times N$ size. Medical images must meet the ASR model's requirement that the source images must be of the same size. As a result, ASR is an excellent option for fusing multi-view images.

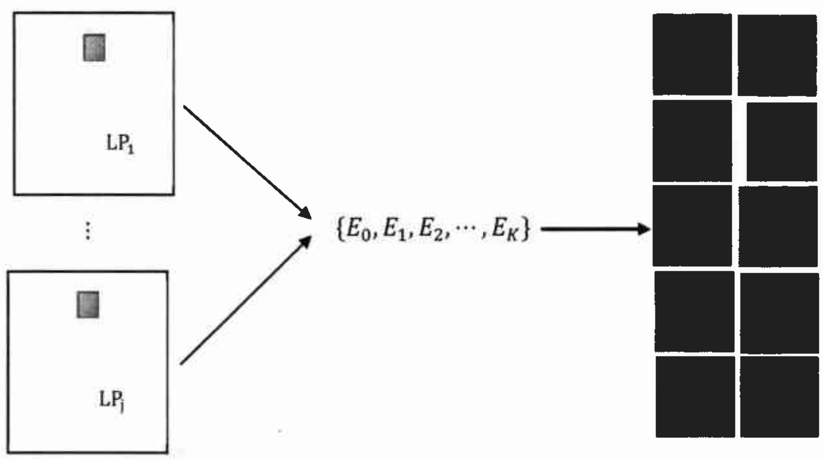

Figure 3.4: Using ASR's dictionary composition and selection.

A new LP of the fused images was made using the pertinent layers from the two images of the LP by using the learned sub-dictionaries $\{E_0, E_1, E_2, \dots, E_k\}$. The sub-dictionaries $\{E_0, E_1, E_2, \dots, E_k\}$ were generated through the following five steps:

1. For each image input μ_j, window that slides with a $\sqrt{n} \times \sqrt{n}$ was used to remove all patches that had one-pixel steps from right to left and upward to downward. It was assumed the $\{s^i{}_1, s^i{}_2, \dots, s^i{}_J\}_{i=1}^{e}$ was a set of patches in $\{\mu_1, \mu_2, \mu_3, \dots, \mu_J\}$ for the i^{th} image. $e = (M - \sqrt{n} + 1) \times (N - \sqrt{n} + 1)$ indicates that how many patched were sampled from each input image.

2. The column vectors $\{v^i{}_1, v^i{}_2, \dots, v^i{}_J\}$ were obtained by rearranging the patches $\{s^i{}_1, s^i{}_2, \dots, s^i{}_J\}$, and each column vector $v^i{}_j$ was made to be zero mean by subtracting the the mean value $\bar{v}^i_j$ from each value of the column vector.

$$\hat{v}^i_j = v^i_j - \bar{v}^i_j.1; \qquad j = 1, 2, \dots, J \tag{3.19}$$

where $\mathbf{1}$ is the unit vector of $n \times 1$;

3. From the set $\{\hat{v}^i_1, \hat{v}^i_2, \dots, \hat{v}^i_J\}$, the $\hat{v}^i_{max}$ with the greatest variance was chosen. Then, using $\hat{v^i}_{max}$, a gradient orientation histogram was generated, and one sub-dictionary was chosen from $E = \{E_0, E_1, \dots, E_K\}$, which had a total of $K+1$ sub-dictionaries. The gradient orientation histogram can be written as:

$$\theta = \{\theta_0, \theta_1, \dots, \theta_K\} \tag{3.20}$$

Now defining E_{ki} as an adaptive sub-dictionary with k_i as index of E_K in which the patch v_i should be divided. The procedure for selecting k_i is shown below:

$$k_i = \begin{cases} 0 & :, \frac{\theta_{max}}{\sum_{k=1}^{K} \theta_k} < \frac{2}{K} \\ k^* & : \text{otherwise} \end{cases} \tag{3.21}$$

where θ_{max} is:

$$\theta_{max} = \max\{\theta_0, \theta_1, \dots, \theta_K\}$$

and the index of θ_{max} is shown as:

$$k^* = argmax\{\theta_k | k = 1, \dots, K\}$$

4. The dictionary that was chosen for SR fusion was D_{ki}. The sparse vectors $\alpha^i{}_F$ of $\{\alpha^i{}_1, \alpha^i{}_2, \dots, \alpha^i{}_J\}$ were obtained after extracting vector $\hat{v}_j{}^i$ from the LP_0 of both source images.

$$\begin{aligned} \max_{\alpha^i_j} \quad & \|\alpha^i_j\| \\ \text{subject to} \quad & \|\hat{v}^i_j - E_{k_i}\alpha^i_j\|_2 < \sqrt{n}c\sigma + \varepsilon \end{aligned} \tag{3.22}$$

where $c > 0$ is a constant and $\varepsilon > 0$ is the error tolerance. The flow graph diagram of above discussed steps are also shown in Figure 3.5.

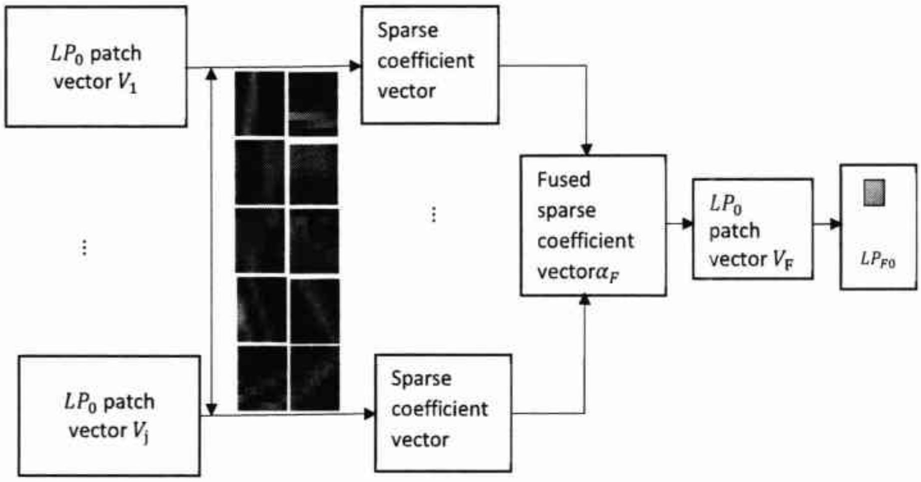

Figure 3.5: LP sparse vector fusion technique.

The fusion rule Max-L1 was used for the fusion of sparse vectors $\{\alpha^i{}_1, \alpha^i{}_2, \ldots, \alpha^i{}_J\}$,

$$\alpha_F^i = \alpha_{j^*}^i; \quad j = 1, 2, \ldots, J \tag{3.23}$$

where:

$$j^* = \underset{j}{arg\,max}\{\|\alpha_j^i\|_1, \quad j = 1, 2, \ldots, J \tag{3.24}$$

The following value should be used as the merged mean value: $\bar{v}_F^i$

$$\bar{v}_F^i = \bar{v}_{j^*} \tag{3.25}$$

Eventually, the projected outcomes of the first layer of $\{v^i{}_1, v^i{}_2, \ldots, v^i{}_J\}$ are as follows:

$$v_F^i = E_{k_i}\alpha_F^i + \bar{v}_F^i.1; \tag{3.26}$$

5. In $\{s^i{}_1, s^i{}_2, \ldots, s^i{}_J\}_{i=1}^{e}$ for the source image patches, Steps 2 to 4 are repeated to obtain the

fused results $\{v_F^i\}_{i=1}^{e}$ of LP_0. The process of choosing the sub-dictionary E_{Ki} is repeated in order to fuse the pyramid's remaining three layers. Finally, we can build the fused LP image LP_F.

3.3.2.3 Image Reconstruction and Fusion

The inverse LP transform is represented in the form of the equation given below:

$$P_{F_{l-1}} = P^*_{F_l} + LP_{F_{l-1}} \qquad (0 < l < 4) \tag{3.27}$$

where $P_{F_l} = LP_{F_l}$ and the Gaussian pyramid of the l^{th} layer retrieved by LP_{F_l} is P_{F_l}. According to Equation (3.27), the corresponding Gaussian pyramid is obtained after recursion on the top layer of the LP, and then, the fused image I_F is acquired.

3.3.3 Nodule Classification

The ultimate objective of the dissertation was to classify the lung nodules into benign or malignant and also reduce the rate of false positives per scan. SVM classifier was used for detection of lung nodule after feature extraction from final resultant fused image.

3.3.3.1 Feature Extraction

To reduce the certain characteristics from the original data set, feature extraction was used. In the proposed system, large initial set of features were selected to represents the state of the art features utilized in the CAD systems. Initially, features were selected and trimmed down to the optimal subset for the detection of nodule with respect to sensitivity and FP/scan. The characteristics of the nodule during the selection process were broadly categorize into intensity, texture and shape.

3.3.3.2 Support Vector Machine Classifier

Since the SVM classifier is very effective and computationally efficient, we used it in our proposed methodology. The fact that there are often far fewer samples of nodules than samples of non-nodules has an effect on a classifier's performance. To minimise biasness, we balanced our dataset by randomly picking an equal number of nodules and non-nodules. To be more accurate, 30% of the data is kept as a test set for the system's final decision and 70% is retained for training. During the training phase, we used a k-fold cross-validation technique for model selection and validation. The k-fold cross-validation process randomly divides the training dataset into k equal-sized subsamples. Following that, one sample is picked from those samples to use as validation data for the evaluation, and the remaining $k-1$ instances are used to train the classifier. k times are used to complete this process. The k outcomes from the folds are then averaged to provide an estimation. This technique has the advantage of only validating each value once, and each sample is utilised for both training and validation. The classifier's input during the training phase consists of the feature vector and the specified class labels. The classifier is eventually tested totally on the test set once it has been trained and its hyper-parameters have been modified. More specifically, the classifier's final evaluation uses 30% of the data that was previously suppressed, and the results are reported in the result section. The features were exclusively chosen from the training set. We next adjust it and apply it to the test set once we have extracted the best feature set for nodule detection from the training dataset, taking into consideration both sensitivity and FP/scan. The four main metrics that may be used to evaluate a classifier's performance are sensitivity, specificity, accuracy, and receiver operating characteristic curves (ROC curves) as shown in Table 3.1.

Table 3.1: Results of Gaussian SVM classification Using 2, 5, 7, and 10-fold cross-validation scheme

K- fold	AUC	Accuracy	Sensitivity	Specificity	FPs/Scan
Two fold	0.980	98.0	97.9	98.5	2.0
Five fold	0.975	97.40	98.32	96.40	2.88
Seven fold	0.965	97.40	98.41	96.40	2.91
Ten fold	0.974	97.30	98.36	96.28	2.67

3.4 Results

In this section, the experimental results of the proposed technique are presented and evaluated by comparing with other recently published results of other proposed techniques/methods.

3.4.1 Dataset

The LIDC-IDRI of lung CT images was used to evaluate the performance of the proposed algorithm. We considered 4,682 scans of 61 different patients from this dataset, which contains nodules of a size of 3–30 mm. Each patient has 60–120 slices. The dataset is in DICOM format contains $512 \times 512 \times 16$ bit images and 4096 gray-level values in HU. The pixel spacing range is from 0.78 mm to 1 mm, whereas the reconstruction interval ranges from 1 mm to 3 mm. We implemented our algorithm in MATLAB R2019a.

3.4.2 Image Segmentation

The first part of the proposed algorithm is image segmentation. For the evaluation of our proposed technique for lung segmentation, the DSC index was used to estimate the consistency between the original segmentation and our calculated results. The dice coefficient is calculated by using the formula:

$$d = 2 * \left(\frac{\mid O_{img} \cap F_{img} \mid}{\mid O_{img} \mid + \mid F_{img} \mid}\right)$$

where O_{img} is the original image, while F_{img} is the segmented result. The results of image segmentation are shown in Figures 3.6 and 3.7. The DSC index was used as an evaluation parameter for the image segmentation. The DSC index value of the proposed method was 0.9929, which is better than the published results of 0.9874 [146].

In Figure 3.7, three cases are presented to show the results. The first column displays the original images taken for lung segmentation, while the second column displays the outcomes with a thick boundary of the selected region. The third column presents the final results of the segmentation. In Figure 3.8, the segmentation results of the proposed method are compared with the results of recently published techniques. Figures 3.9 and Table 3.2 provide a precise comparison of the conventional methods with the proposed method for quantification. The DSC index value of the proposed method was 0.9929, better than the other listed results.

Table 3.3 compares the overall performance of the proposed technique with existing techniques. In this table, three parameters, sensitivity, specificity, and accuracy, are used for evaluation purposes. The quantitative results showed that the purposed technique outperformed the U-Net [147], AWEU-Net [148], 2D U-Net [119], 2D Seg U Det [149], 3D FCN [150], 3D nodule R-CNN [151], 2D AE [152], 2D CNN [153], 2D LGAN [154], and 2D encoder–decoder [155]. The accuracy of purposed method was 99%, which is much better than the other listed methods, as shown in Table 3.3. The sensitivity of the purposed method was 89% higher than all listed methods, except the published results by the AWEU-Net and 2D encoder–decoder. However, the other parameters values were lower than the purposed method.

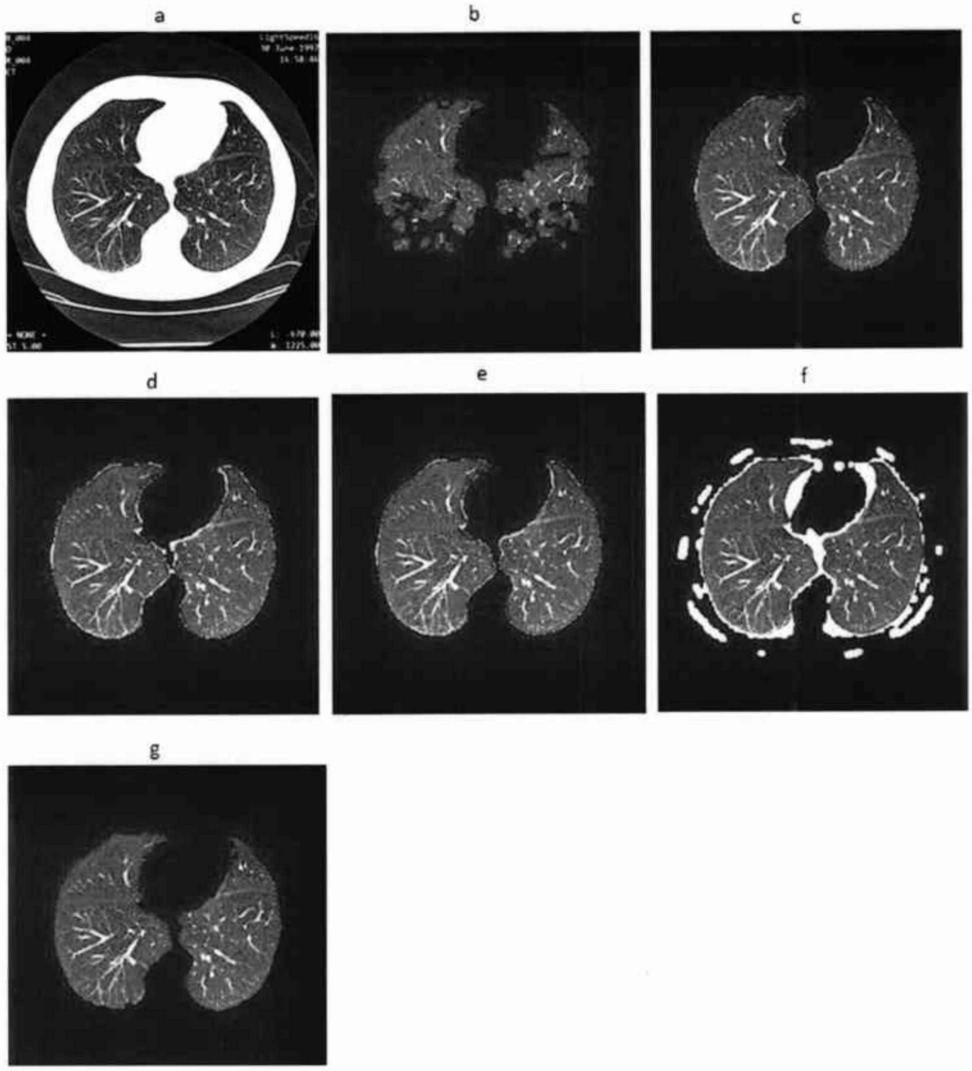

Figure 3.6: Result of the segmented image using the proposed method, (a): Source image, and (b–f): Segmented image with various global thresholds, (g): Final segmented image

3.4.3 Image Fusion Results

This section describes the result of the proposed fusion method. A comparative experiment was performed with single-patient multi-view diagnostic images of lungs to check the feasibility of the proposed procedure (CT images). In this study, the experiment was performed using the CT images of the lung patients. There were six indices used to test the fusion results. The contrast was measured using the Average Pixel Intensity (API). The arithmetic square root of the variance is the Standard Deviation (SD), which represents the degree of dispersion. The total amount of information in the image is represented by the entropy (H) [169]. The resolution

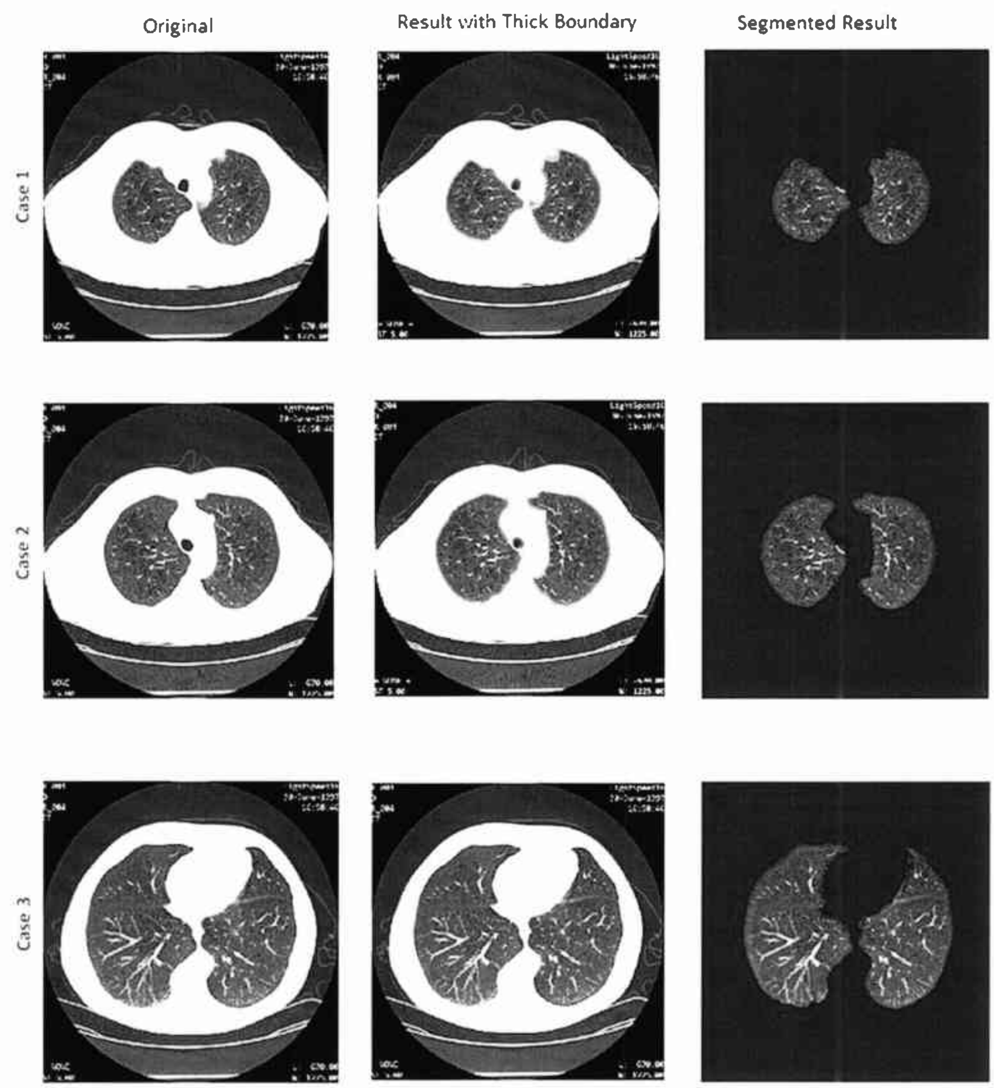

Figure 3.7: Segmented images using the proposed algorithm. The left, center, and right columns are the original CT images, segmented with a thick boundary, and the final segmented images, respectively.

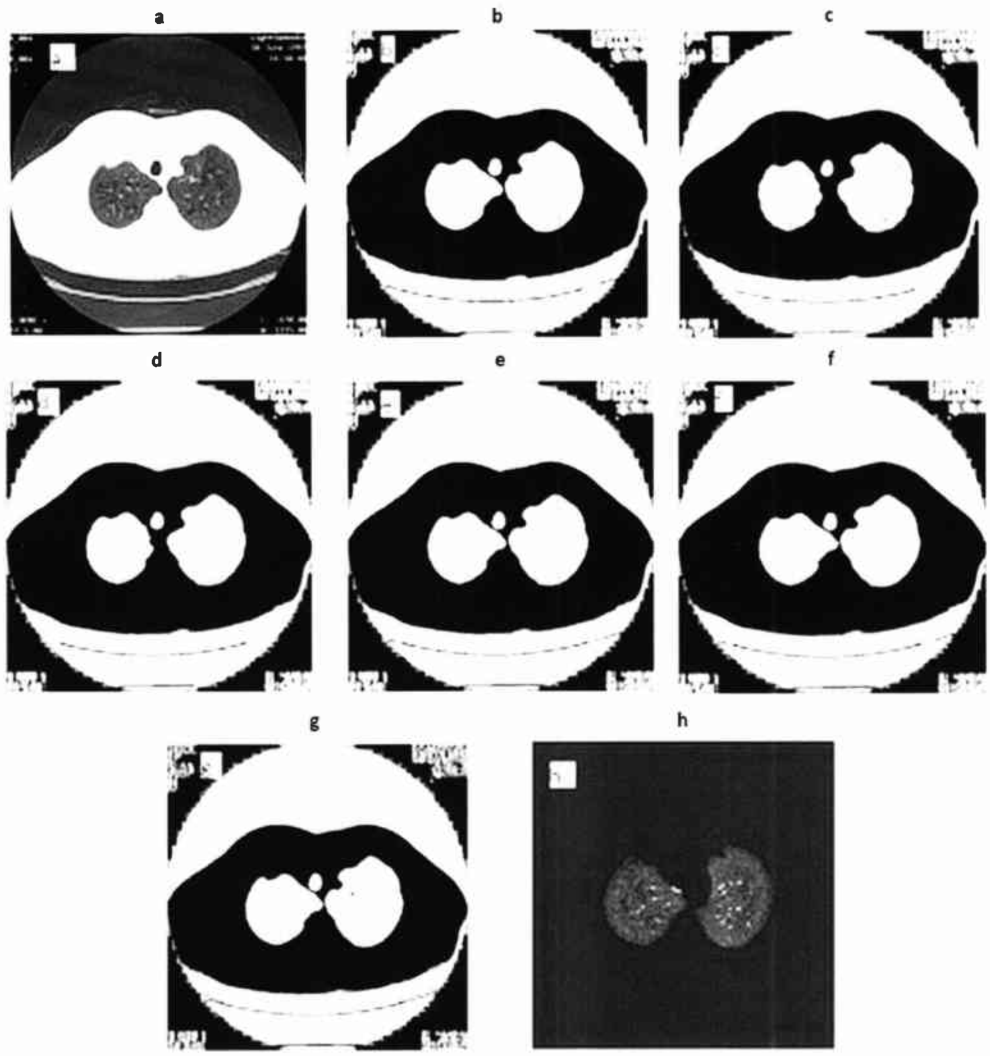

Figure 3.8: Comparison of the segmentation methods, (a): Original image, (b): Region Detection(RD), (c): Level Set Without Initialization (LSWI), (d): Re-initialization Methods (RMs), (e): GDRLSE1, (f): GDRLSE2, (g): GDRLSE3, (h): The proposed method

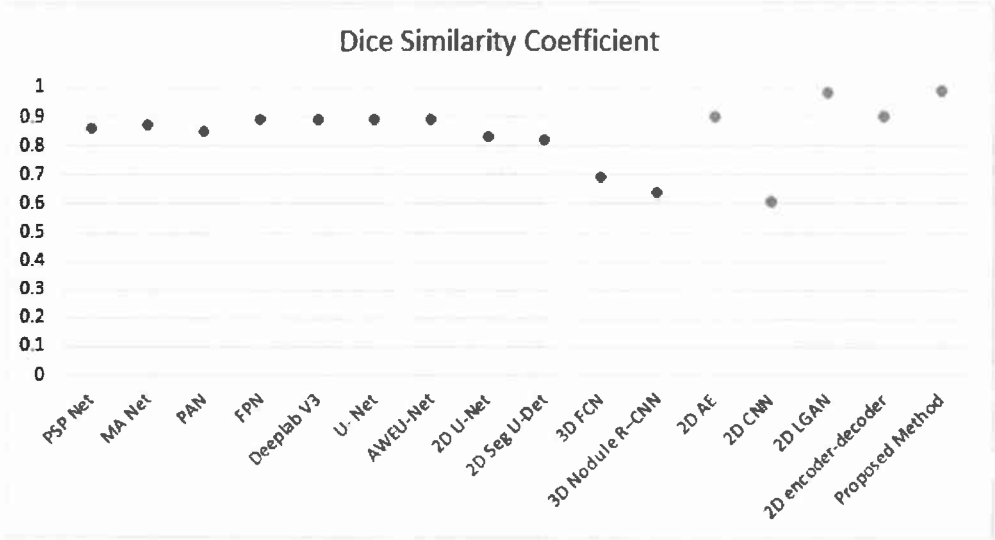

Figure 3.9: Dice coefficient comparison of existing methods with the proposed method.

Table 3.2: Quantitative comparison of different methods.

Method	Dice Similarity Coefficient	Running Time (s)
U-Net [147]	0.89	-
Attention-UNet[156]	0.466	-
Gated-UNet [157]	0.447	-
Dense-UNet [158]	0.410	-
U-Net + [159]	0.444	-
Inf-Net [160]	0.579	-
Seg-Net [161]	0.705	-
BiSe-Net [162]	706	-
ESP-Net [163]	0.706	-
U-Net++ [164]	0.714	-
AWEU-Net [148]	0.89	-
2D U-Net [119]	0.83	-
2D Seg U- Det [149]	0.82	-
3D FCN [150]	0.69	5.0
3D Nodule R- CNN [151]	0.64	-
2D AE [152]	0.90	-
2D CNN [153]	0.61	-
2D- LGAN [154]	0.98	-
2D Encoder–Decoder [154]	0.90	-
RD [165]	**0.992**	169.2
re-initialization method [165]	**0.993**	1593
GDRLSE1 [165]	**0.992**	161.57
GDRLSE2 [165]	**0.992**	237.66
GDRLSE3 [165]	**0.992**	265.26
Level Set Without Initialization [166]	**0.993**	124.83
RASM+OSF [167]	0.974	270
MSGC [168]	0.988	1800
GMMs [146]	0.987	900
Proposed Method	**0.99**	**1.2252**

of the fusion effects is measured by the Average Gradient (AG). Mutual Information (MI) reflects the energy transferred from the input image to the fused output image [170]. The Spatial Frequency (SF) was used to analyze the total level of the fused output image information. Edge retention ($Q_{AB/F}$) [171] refers to how much the input image edge information is preserved in the final result. The total loss of the image was determined using $L_{AB/F}$ [172], and the level of noise and other related artifacts was calculated using ($N^{m}_{AB/F}$) [172].

Figures 3.10–3.12 present the fusion results obtained using various fusion methods. In general, the proposed approach produced a fused image that retained the edges and information as well. Figure 3.10 shows the source multi-view images. The first column shows the different

Table 3.3: Result comparison of the proposed method with existing techniques.

Methodology	Sensitivity (%)	Specificity (%)	Accuracy (%)
U-Net [147]	84.0	96.3	94.3
AWEU- Net [148]	90.0	96.4	94.6
2D U-Net [119]	89.0	-	-
2D Seg U-Det [149]	85.0	-	-
2D Encoder–Decoder [154]	90.0	-	-
Attention-UNet[156]	72.3	93.0	39.0
Gated-UNet [157]	67.4	95.5	37.5
Dense-UNet [158]	67.7	97.7	41.5
U-Net + [159]	87.7	92.9	36.9
Inf-Net [160]	87.0	97.4	50.0
Seg-Net [161]	85.2	95.4	-
BiSe-Net [162]	70.6	85.2	-
ESP-Net [163]	70.6	93.3	-
U-Net++ [164]	73.3	97.0	73.9
RASM+OSF [167]	-	-	97.5
MSGC [168]	-	-	**98.0**
GMMs [146]	-	-	79.7
Proposed Method	**97.9**	**98.5**	**98.0**

multi-view source CT images. The second, third, and fourth columns show the different layers of the Gaussian pyramid. The proposed approach was applied to the source images at different levels.

The SR method easily created a block effect, as seen in Figure 3.11. Poor gradient contrast and the block effects were not eliminated by the ASR approach, resulting in a fusion result with a blurred texture and structure. The lack of pattern, poor contrast and fuzzy edges in the fused lungs images would greatly impact the doctor's treatment accuracy. The proposed method, on the other hand, it can produce better fusion results and is consistent with the human visual system, as shown in Figure 3.12. The suggested approach therefore obtained the maximum extent of medical image fusion efficiency and is applicable to healthcare.

To evaluate the experimental results, six statistical indicators, SF, MI, API, SD, AG, and H, were used. The better the quality of the fused image, the higher the value of each indicator is. Since the values of API, SD, and SF were too high, we divided them by ten to make the observation easier. $(Q_{AB/F})$, $(L_{AB/F})$, and $(N^{m}_{AB/F})$ are the fusion efficiency metrics Q, L, and

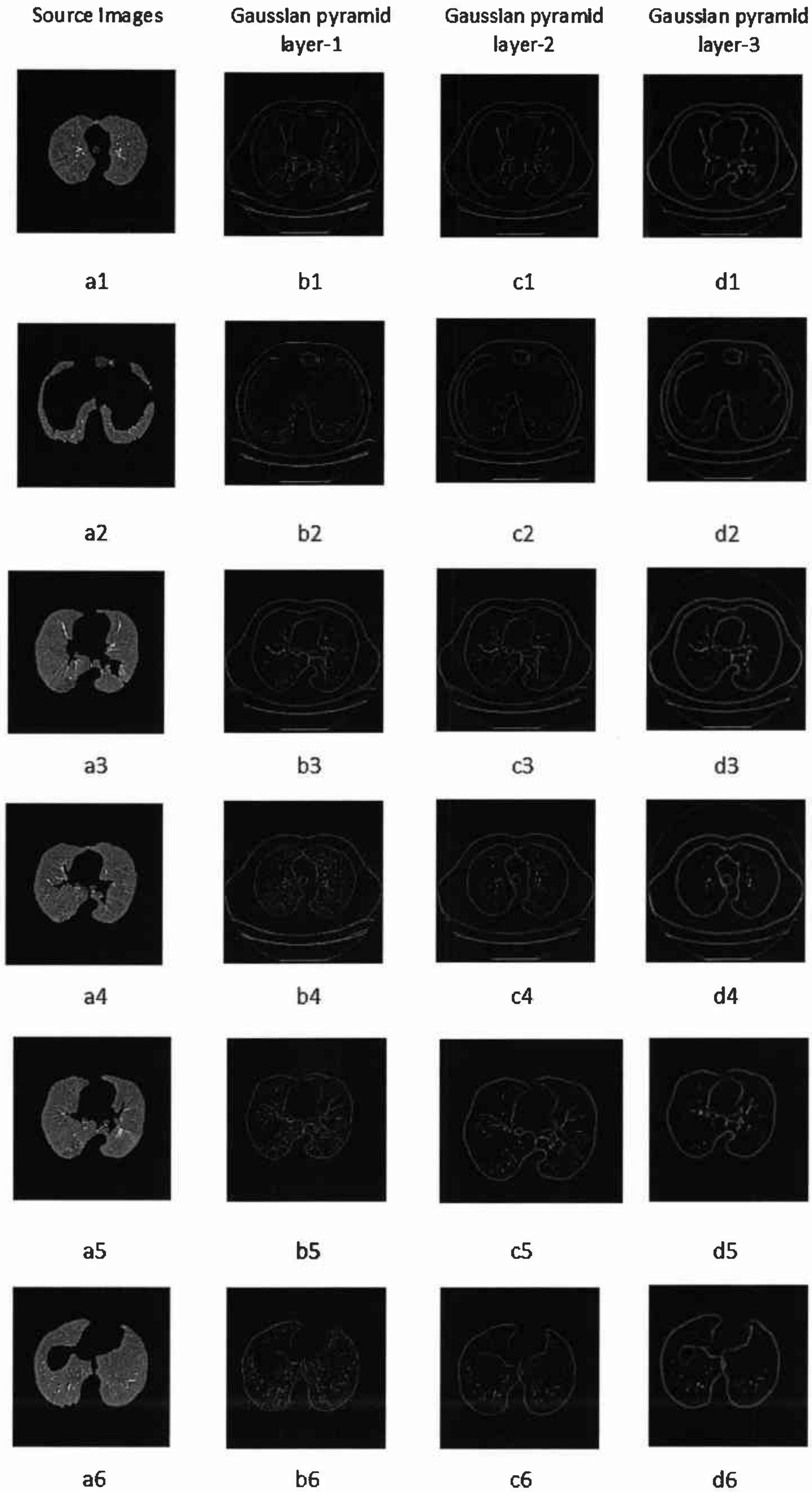

Figure 3.10: (a1)–(a6): Source images, (b1)–(b6): Gaussian pyramid of Layer 1, (c1)–(c6): Gaussian pyramid of Layer 2, (d1)–(d6): Gaussian pyramid of Layer 3

N, respectively Table 3.4. $(Q_{AB/F})$ has a positive sign as well, but the $(L_{AB/F})$ and $(N^{m}_{AB/F})$ values should be lower.

Table 3.4: Conventional statistical indicators and objective performance measures of Figure 3.12.

Method	API	SD	AG	H	MI	SF	Q	L	N
LP [144]	4.60	7.84	9.19	3.88	2.71	2.16	0.80	0.17	0.02
DWT [173]	5.30	7.07	8.41	4.10	2.68	1.89	0.76	0.22	**0.01**
CVT [174]	5.46	7.22	9.51	5.22	2.42	2.08	0.77	0.20	**0.01**
NSCT [175]	5.42	7.42	9.38	4.66	2.57	2.13	**0.81**	**0.16**	0.02
SR [176]	5.33	7.48	9.16	3.72	3.59	2.53	0.75	0.20	0.03
ASR [145]	5.37	7.27	9.68	3.99	2.64	2.17	0.76	0.22	0.02
Proposed Method	**5.76**	**8.13**	**10.64**	**5.62**	**3.78**	**2.70**	0.79	**0.16**	**0.01**

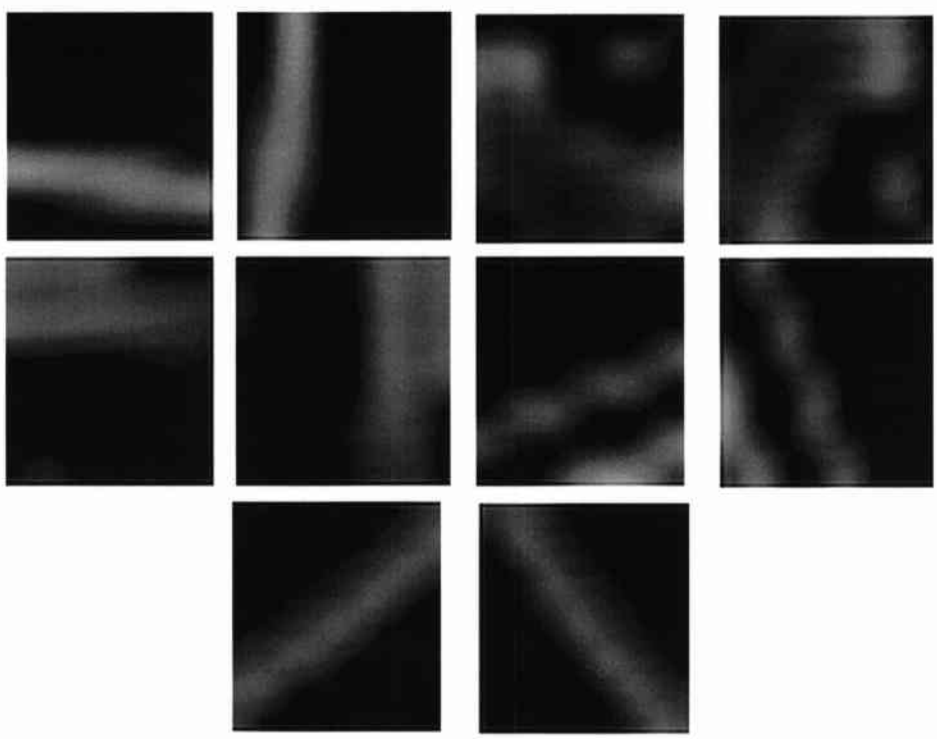

Figure 3.11: Dictionary random samples from a single-source image.

The proposed method showed significant results with respect to the API, SD, and MI, indicating that the suggested technique has a good capacity to maintain details. Because of the block effect, the SR method outperformed the proposed method in terms of the AG and SF. As shown in Figure 3.12, the resultant images acquired by using the SR method contained several artifacts and became smooth due to the loss of internal information in the fused image. The proposed approach had the best $(L_{AB/F})$ and $(N^{m}_{AB/F})$ ratings, i.e., it retained the relevant infor-

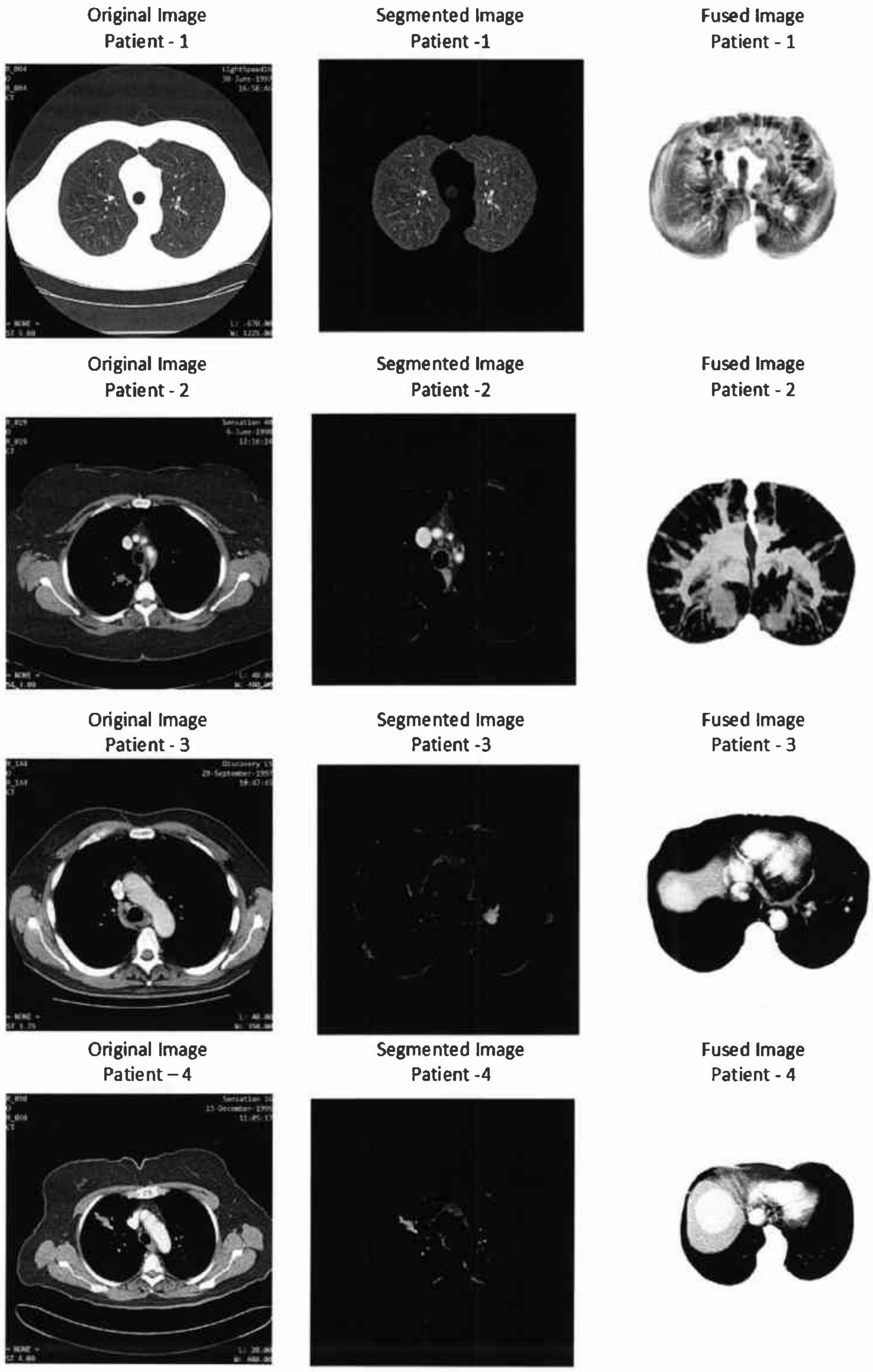

Figure 3.12: Final fused results of lung CT images of different patients.

mation from the source image while still maintaining the edge and structure. This shows that our method is effective in general. According to the study of the fusion results, the suggested technique had a better overall performance than the other fusion techniques. As a result, when evaluating multi-view medical image fusion, it is important to consider if the assessment indexes are appropriate and conform to the human visual system. The results showed that the proposed approach mostly produced the high-quality fused image with no distortion while attempting to recreate the fused image with all the information and structure preserved.

3.4.4 Nodule Detection

1332 nodules out of 2341 CT scans, 612 were malignant and 720 were benign by using to evaluate the proposed method. The complete set of data was randomly and evenly partitioned into 2, 5, 7, and 10 subgroups for 2-fold, 5-fold, 7-fold and 10-fold cross validation respectively. We calculated the average level for each nodule in order to determine the nodule's level and came to the conclusion that: if the average level is greater than 3, this nodule is considered to be malignant; if the average level is less than 3, it is considered to be benign; and if the average level is equal to 3, it is considered to be uncertain and is discarded as shown in Table 3.5. In order to assist the radiologists in making decisions, an estimated malignant probability was also given to them. To evaluate the effectiveness of our proposed system with the existing lung CAD system, as shown in Table 3.6. In terms of sensitivity and FP/scan, our proposed method outperforms in existing systems. Other systems with comparable performance include Zhang et al.[96] and Naqi et al.[177], which developed a shape-based feature extraction technique. In addition to the 2D form characteristics, Naqi et al. calculated the 3D shape features Volume, Compactness, Bounding Box Dimensions, Elongation, and Principal Axis Length (Area, Diameter, Perimeter, Circularity). Proposed system has sensitivity performance with a value of 97.9% and performance achieved in terms of false positive with a value of 2.0 FP/scan.

Table 3.5: Lung nodule categorization by proposed technique

Patient Image (PI) No.	**Nodules (N)**	**Classification**	**Remarks (True=T,False=F)**
PI-9	N-1	Malignant	T
	N-2	Malignant	T
	N-3	Malignant	T
PI-34	N-1	Malignant	T
	N-2	Benign	T
	N-3	Benign	T
PI-42	N-1	Malignant	T
	N-2	Malignant	T
	N-3	Malignant	T
PI-135	N-1	Malignant	T
	N-2	Benign	T
	N-3	Malignant	T
PI-267	N-1	Malignant	T
	N-2	Malignant	T
PI-395	N-1	Benign	T
	N-2	Malignant	T
	N-3	Malignant	T
PI-483	N-1	Malignant	T
	N-2	Malignant	F
	N-3	Malignant	T
PI-592	N-1	Malignant	T
	N-2	Benign	T
	N-3	Benign	T
PI-643	N-1	Benign	T
	N-2	Benign	T
PI-813	N-1	Malignant	T
	N-2	Benign	F
	N-3	Malignant	T

A progressive advance selection approach was then applied to obtain the optimal feature subset. The proposed system performed well in terms of sensitivity, specificity, and accuracy. The system was assessed by using the LIDC dataset with 1332 nodules to validate the results. The system has an significantly high in accuracy, sensitivity, and specificity with the value of 98.0%, 97.9%, and 98.5% respectively.

Table 3.6: Performance comparison between proposed and existing CAD systems with nodule size 3-30(mm)

Method	Accuracy	Sensitivity	Specificity	FP/Scan	No.of Nodules
Proposed Method	**98.0**	**97.9**	**98.5**	**2.0**	1332
Naqi et al [177]	96.9	95.6	97.0	2.8	777
Xie et al [178]	-	83.0	-	8.0	-
Shaukat et al [102]	93.7	95.5	94.28	5.27	148
Zhang et al [96]	93.6	89.3	-	2.1	168
Ali et al [98]	64.4	58.9	55.3	-	888
Teramoto and Fujita [179]	-	83.0	-	5.0	186

3.4.5 Discussion

In view of a global pandemic and its effect on lung cancer patients, early diagnosis using segmentation of lung CT images has received greater attention from clinical analysts and research scholars. They have proposed many algorithms to achieve the objective of preciseness and accuracy. Taking this into consideration, a novel method based on the adaptive global threshold was proposed by considering three different aspects: DSC, accuracy, and time-based analysis. First, the DSC results are computed in Table 3.2, which can be further validated by Figure 3.9. In order to evaluate the proposed method, the results were compared with the results of the recently published methods and the manual segmentation made by experts. From Figure 3.8, it can be observed that the proposed method provides accurate lung segmentation results. The proposed method extracts the lung region accurately, as it uses a modified algorithm and mathematical morphological operations. In Figure 3.6, the specific value of the threshold is σ, which was applied to the input of the original image. The level of the grey threshold was 2/3 in our experimentation. The segmented lung boundary is flawless and clear with the mentioned value. In this way, the accuracy perfectly aligned with the requirements.

Next, the fusion was performed and improved the classification parameters, as given in Table 3.3 and Figure 3.12. The fusion accuracy achieved by the proposed method was 98%. From the review of the existing methods, we found that it is very hard to compare the results with the previously published work because of their use of non-uniform performance metrics and different evaluation criteria including the datasets and types of nodules considered. Despite the constraint, we tried to make a performance comparison of our proposed system with the other lung CAD systems, as shown in Table 3.3. It can be seen that our proposed system showed better performance compared to the other systems regarding the sensitivity, specificity, and accuracy. Other systems that were close on the performance indicators, i.e., API, SD, AG, H, MI, SF, $Q_{AB/F}$, $L_{AB/F}$, and $N^{m}_{AB/F}$, are shown in Table 3.4. It is clear that the proposed method had the optimum performance on the API, SD, and MI, which demonstrates the ability of the suggested method to retain the particular information. The images produces by the suggested method included various artefacts, and the fused image was too smooth since too many internal features were lost, according to the values of $N^{m}_{AB/F}$ in Table 3.4. The smaller values of $L_{AB/F}$ and $N^{m}_{AB/F}$ indicate that the image had a minor loss of information along with artifacts in the fusion process. The study of the fusion outcomes leads to the conclusion that the suggested method performs more effectively overall than the other fusion methods.

The fusion approach has a significant disadvantage in terms of computing time, while the total classification time is prolonged by the fusion of several characteristics, which can be reduced by the selection process, but in the proposed method, it was minimized to 1.22 sec. An analysis of the given comparison between the computing time and final segmented results revealed that our proposed method of the adaptive global threshold is more efficient in lung segmentation. The proposed approach would improve the fused images' contrast and brightness. The output of the experiments showed that the suggested technique can significantly preserve detail information within a range, provide a clear view of the input images data, and ensure that no additional objects or information are added during the fusion process. In particular, the proposed method contains information regarding the edges and structure of all CT image slices. The proposed method was applied only on a LIDC-IDRI dataset, which is the limitation of this study.

3.5 Conclusions and Future Work

Lung segmentation has gained much attention in the past due to its effectiveness in lung CT image processing and clinical analysis of lung disease, and various segmentation methods have been suggested. A robust lung segmentation method is also required to support computer-aided lung lesion treatment planning and quantitative evaluation of lung cancer treatment response. The improved global threshold approach has made significant development in the field of computer vision and image processing, prompting us to study its utility in lung CT image segmentation. As a result, selecting the appropriate collection of characteristics can improve the system's overall accuracy by increasing the sensitivity and decreasing false positives. To evaluate the system's effectiveness, we also used fusion methods (LP and ASR) and classified using SVM; however, the findings clearly revealed that these methods reduce image noise and enhance the image quality by reducing the time as shown in Table 3.2. Experiments revealed that the suggested approach produced favourable outcomes with accuracy (98%), sensitivity (97.9%), and specificity (98.5%).

Our proposed method outcomes showed significant results, but it still has potential for improvement. First, the fusion rule of the detail layer requires further research. Secondly, the system should be evaluated on large and different datasets to achieve greater robustness.

Chapter 4

Enhanced Lung CT Image Segmentation using Multi-View Image Registration and Fusion for Lung Cancer Detection

In the previous chapter, we discuss the improved lung segmentation, fusion, detection, and classification techniques. Here, another multi-view strategy is used to expand the amount of qualitative and quantitative medical data available to doctors, allowing them to identify cancer in its starting phase immediately. For multi-view image registration, MRR is suggested in this method, while, for image fusion, DWT and PCAv are employed for this purpose. After that lung nodules were detected and stage classifying by using the proposed GA-CNN. For quantitative assessment of the proposed technique, seven different quality analysis measures are used to quantify the fusion results.

4.1 Introduction

Lung cancer is one of the most lethal forms of cancer, with an estimated 422 people dying every day around the world [36]. Cancer is most often diagnosed after the age of 50 years, so the number of lung cancer patients increases every day [180]. Since lung cancer is difficult to detect relative to other diseases, it is considered one of the leading causes of death. The primary cause of failure is the small size of the lesion, which is referred to as a nodule. Tumor cell size is small in the beginning stage, but it grows and becomes malignant after a certain period. Therefore, controlling the disease at an early stage has become important. If cancer is detected early, the survival rate can be improved [10]. Recently, computer vision researchers have developed high-tech networks that automatically spot and identify healthy and tumor areas [11].

One imaging modality is inadequate to give the morphological and functional data needed to diagnose normal and diseased structures in medical imaging. To provide expanded medical knowledge that cannot be seen with a single imaging modality, multi-view medical imaging requires the use of two or more images. Multi-view diagnostic imaging improves the identification of lesions, cancerous cells, non-cancerous cells, and tumors [181]. Multi-view image registration and fusion can create a final image that contains the most detail. Registration and fusion procedures are used to resolve this constraint to diagnose certain diseases more reliably [182]. Image registration works in the lines of geometrical dimensions of both images and matches their level of intensity. After image fusion, the next step is to overlays both images without removing significant clinical information. The resulting merged image will provide anatomical and functional information. Medical image fusion is the process of combining various single-modality medical images to better understand the morphological structure and metabolic state of lesions and provide a more accurate disease diagnosis. A common medical image fusion combines single-mode different CT images in slices. CT imaging examines how distinct parts of the human body absorb X-rays. It can capture the human skeleton and has a high resolution. Nuclear magnetic resonance technology is used in MRI imaging. While it can collect soft tissue details from the human body, it does so at a lower resolution [183].

Recently, the coronavirus disease (COVID-19) outbreak has spread over the world and become a worldwide threat since the end of 2019, prompting the World Health Organization (WHO) to label the outbreak a pandemic. Nucleic acid testing is currently used to diagnose COVID-19, although it can result in false negatives. Lung CT scans can be used to screen and monitor diagnosed cases more effectively. Computer-aided diagnosis technologies can relieve doctors of their responsibilities, allowing for more quick and large-scale diagnostic screening. Image fusion, medical image processing technologies, and computer analysis are used in the computer-aided diagnosis system.

In order to more effectively extract information from medical images and conserve image energy, this study offers multi-view medical image (CT scan) registration and fusion algorithms. The aim of the research is to create registration and fusion tools for early diagnosis of lung cancer. This approach increases image visual perception while also increasing computing efficiency and fusion performance. For multi-view image registration, a MRR technique is presented. This proposed method also employs the DWT as well as principal component averaging. To begin, the image is decomposed into three phases using DWT. The coefficient and approximation components are then obtained using PCA. Separates the coefficient's main element from both images. Finally, fusion quality evaluation metrics are utilized to assess the merged image quality. Using multi-view imaging, surgeons and other medical professionals may conduct surgery with greater accuracy. The suggested methodology's contribution is to use multi-view CT scans to more clearly visualise anatomical and functional elements of the lung.

The primary contributions of this study can be summarised as follows:

1- Human visual system is sensitive to the changes of image contrast. Thus, this chapter proposed multi-view contrast pyramid decomposition based image fusion method, which can selectively highlight the contrast information of fused image to achieve better human visual effects.

2- For the high-frequency components of multi-view medical images, it suggests a useful fusion rule. To improve the specific qualities of high frequency components, the fusion rule integrates three low-level aspects, including local phase consistency, local abrupt metric, and local energy information.

3- The lung are manually marked by the radiologist in most existing CAD-based nodule detectors, which is a time-consuming and laborious procedure. In the proposed algorithm, the lung are automatically segmented from the CT images without any user intervention.

4- Nodules come in a variety of shapes and sizes, both regular and irregular. Existing algorithms detect nodules using a few shape templates, however the proposed methodology is independent by nodule shape or size.

5- In an experimental evaluation carried out on a standard LIDC dataset, the proposed system achieved high sensitivity and accuracy, outperforming the existing similar techniques.

4.2 Related Work

Multiview image fusion is one of the latest fields of study in medical imaging. The approaches are divided into three fusion levels i.e pixel, decision, and feature.

A deep learning strategy for medical image fusion was proposed by Liu et al. [45]. The Laplacian method is used in this technique. In the Pilella context presented a DTCWT-based lung cancer CT/PET image adaptable fusion method. As a result, the border and textural data of the lesions could be more highlighted in the reconstructed fusion image. Fei et al. introduced a sparse modeling and decision mapping-based multi-modal medical image fusion approach, enhancing the algorithm's efficiency while simultaneously improving the accuracy of the fusion findings [184]. Li et al. utilized an updated CNN model to estimate the volume of the ventriculus sinister using MR images for multi-view fusion [125]. A method for using fusing images that uses translation-invariant wavelets and cascaded PCA was proposed by Benjamin and Jayasree

[185]. According to the experiments, the fusion method outperforms the visual and quantitative assessment frameworks . An adaptive dictionary learning method for multi-view medical image fusion was proposed by Aishwarya and Thangammal. For dictionary learning, useful information blocks were separated by removing zero data blocks and using MSF to approximate the remaining image patches. This reduced the amount of computing while simultaneously producing a high-quality image [119]. Ziyad et al. proposed a profound knowledge technique for lung cancer classification from CT scan images found to be the most effective in 2019. The removed characteristics from a deep approach are optimized using MGSA [186]. Later, using LDA reduced irrelevant features and got a categorizing precision of 94.57%.

Nasrullah et al. in (2019) developed an automated model to classify lung cancer from CT scan images. A composite connection network connects to profound systems for feature extraction, U-Net and the faster RCNN [187]. A Gradient Boosting Machine (GBM) was used to grouped using such elements and these elements yielded a sensitivity of 94% when tested on 1200 CT scan images. Moreover, in 2019 Zhang et al. proposed model based on hybrid features to classify lung nodules from CT scan images [188]. For better characterization of lung nodules, they combined CNN, LBP, and HOG characteristics. Finally, the GBM classifier is used to classify the fused features, with a precision of 93.78%.

A novel multi-modality medical image fusion strategy was proposed by Zhu et al. 2019 based on phase congruence and local Laplacian energy. Low-pass subbands are subjected to a local Laplacian energy-based fusion rule. The fused image is created by inverting the combined high-pass and low-pass sub-bands. There are three different kinds of multi-view medical image pairings used in the comparative studies to ensure that the suggested strategy is effective. The experiments' results discover that the proposed strategy performs well in terms of image quantity as well as computing costs the comparative studies to ensure that the suggested strategy is effective. The results of the experiments reveal that the proposed strategy does well with respect to image quantity as well as computing costs [189].

In the year 2020, Wang et al present a healthcare image fusion technique stemming from Convolutional Neural Networks (CNNs). For generating a weight map, the suggested methodology blends the trained Siamese convolutional system (network) with the source images' pixel activity information. In the meantime, to deconstruct the original image, a contrast pyramid is used. A weighted fusion operator and the multiple spatial frequency bands are used to combine source images. Comparative investigations reveal that the recommended fusion algorithm is successful in protecting source images' full structure information [190].

Three major phases are included in the proposed method given by Khan et al. (2020). First, the gamma correction maximum intensity weights method improves the contrast of original CT images. Second, multiple texture points and geometric characteristics are removed from contrast images that are fused serially using canonical correlation. Finally, an entropy-based approach substitutes zero values and negative characteristics, followed by a weighted NCA for selection. The most distinguishing characteristics are fed into a collective classifier for the final categorization. The recommended approach is validated using a publicly accessible dataset: Lung Cancer Data Science Bowl 2017, with a maximum precision of 99.4% [191]. Li and Zhao, tomography and MR images are decomposed into low and high frequencies sub-bands. Image reconstruction is used to create the fusion image [125]. The algorithm's fusion findings will significantly improve image fusion accuracy. It has certain benefits in optical impressions and objective assessment, offering a more reliable base for medical detection and treatment of disorders.

Dafni et al, in 2021 [192] developed fused image technique to improve the results of the mass screening based on lung tumor examination along with Fuzzy C-Means (FCM) and framework study based on PET (positron emission tomography) and CT (computerized tomography). It monitored the frequency bands of different images and fused some low-frequency bands with the help of congruency measurement among the image phases. It combined an approach involving direct contrast with an algorithm involving a conventional fusion and the purpose of doing this is to produce fused images of cells at molecular levels. Besides, the accuracy of entropy, similarity value, PSNR is also improved by it. Furthermore, Xiao et al (2022) [193] developed an innovative network of Siamese autoencoder for the fusion of CT and PET. As the object of the model solution, they designed a structural similarity loss function combined with the L1 regularization term. An assessment of intricate experimental design and over 700 pairs of CT-PET images validated the efficacy of the recommended technique. The information entropy gets 0.076 value and the visual fidelity after fusion gets 0.350 value. The fusion performance results are comparatively excellent, which verifies suggested method's usefulness.

4.3 Proposed Method

The proposed method for image fusion is cased on MRR and DWT-PCAv methods in this study. The MRR method is highly precise compared to SRR. The resulting image is then enhanced with the DWT-PCAv fusion technique. Medical CT images are used as input in the current study. The MRR technique is used to line up the images and compare the different levels of their intensities in the initial step of the registration process. It has been noted that the suggested method produces preferable results than the split ring resonating technique. The resulting image is perfectly fitted and provides more useful diagnostic information. The DWT-PCAv fusion method is used to merge both images after registration. Figure 4.1 depicts the overall proposed method's structure. The resulting image is perfectly lined up and provides useful diagnostic data. The DWT-PCAv fusion method is used to merge multiple images after registration. Figure 4.2a shows the source image and 4.2b shows the enhanced image, which is used in the next process of this study and Figure 4.4 depicts the proposed fusion method's structure.

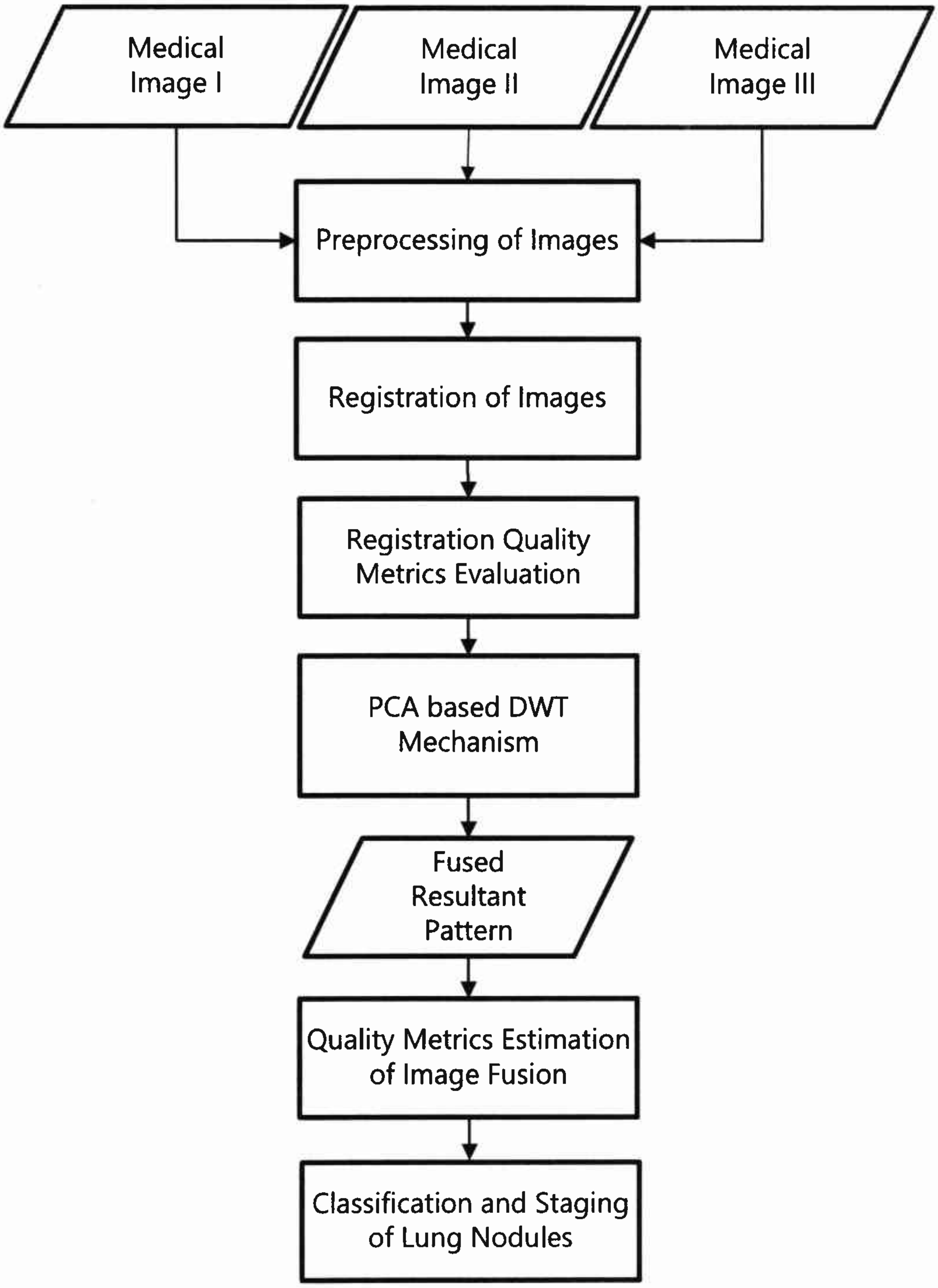

Figure 4.1: Block Diagram of the proposed method

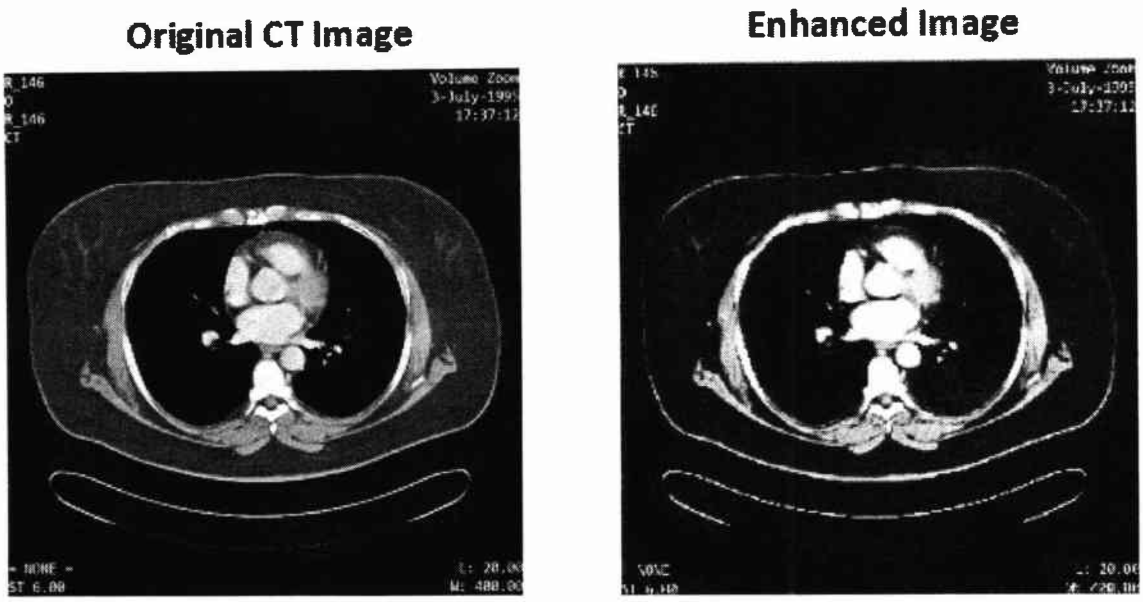

(a) (b)

Figure 4.2: Enhancement of CT image, (a): Original CT Image, (b): Enhanced Image

4.3.1 Multi-Resolution Rigid Registration (MRR)

The improved input medical images are changed at various resolution levels during the MRR process. The multi-view registration pyramid is shown in Figure 4.3. The pyramid's base image has a higher resolution than its top image, which is the lowest. Each level of the separated images will go through a registration process. The registration procedure will produce better results if the input images are identical in size and resolution that, will aid in diagnosing imperfections. The pyramid's base contains the original input images. if they are N x N, the following stage would be $N/2$ x $N/2$, the third level would be $N/4$ x $N/4$. MRR is a geometric transformation iterative process that exploits the similarity among the source and targeted image.

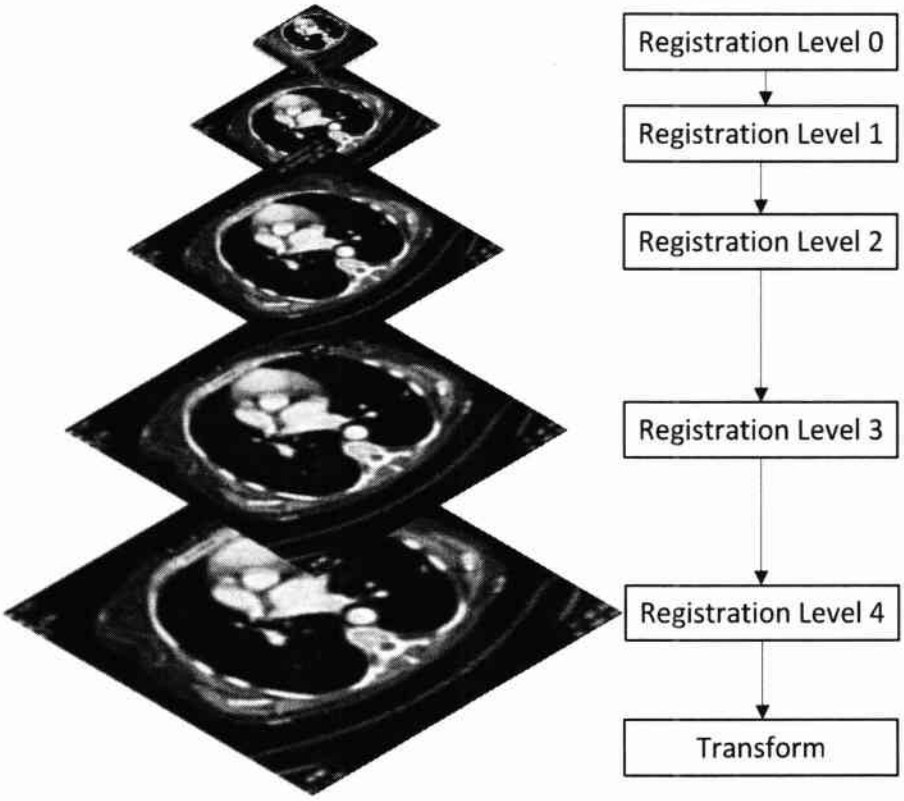

Figure 4.3: Pyramid model of multi-view for registration

To line up the source images into the targeted image, the proposed technique uses affine rigid registration geometric transformations that involve rotation, scaling and shearing of the images. There are several related metrics; however, because to its simplicity and time efficiency, we choose using the cross-correlation similarity metric. The optimizer will execute an automatic MRR process till getting a maximum resemblance among the original and resultant images. It will keep calculating the similarity value until it reaches a maximum and both images are perfectly matched. The similarity metric is defined by a non-convex function. The suggested approach makes use of a gradient descent optimizer. Each pixel's location, value, and neighbouring pixels' values are determined by the interpolator. The optimizer function ensures that images are correctly registered by taking into identical metric standards. The registration procedure uses images with a range of intensities, therefore the similarity function is not continuous and has a number of local optimum values. The images can be better overlapped and recorded after the optimal spot is found. MRR requires more time than SRR since it registers images iteratively.

MRR registration adjusted the levels of each image one after the other, halting when the source and targeted images were exactly aligned. The final recorded image has a greater geometrical arrangement with the intended image. Still, it is more exact with respect to alignment but takes more time for registration. Futhermore, the proposed fusion process can reduce the amount of time spent during the image registration process using the MRR technique.

4.3.2 DWT-PCAv Fusion

Following the MRR approach, the input source images are divided into distinct multi-view resolutions and rotations utilizing DWT.

Figure 4.4 shows the entire step-by-step fusion process. This procedure is utilized to view input images at various levels, with each deconstructed level holding unique data. After the multi-scale breakdown, the main elements are computed on every image coefficients levels. On each level of a decomposed image, the mean of the key elements is calculated, and weights are given to each image coefficient variable for fusion rules. Low-Low (LL), Low-High (LH), High-Low (HL), and High-High (HH) coefficient levels are applied to the input images. The detailed coefficient scale levels LH, HL, and HH are present, while the approximate coefficients factor LL is also presented. The PCA is fed with the LL coefficient components from two source images. The new coefficient elements n_1, n_2 and n_3 are determined from the LL coefficients components. To measure the principle components, other complete coefficient components are also managed. The average of the key elements of the estimation and coefficients is then used to calculate the n_1, n_2 and n_3 average components. Finally, the final image is fused using these two average principal components.

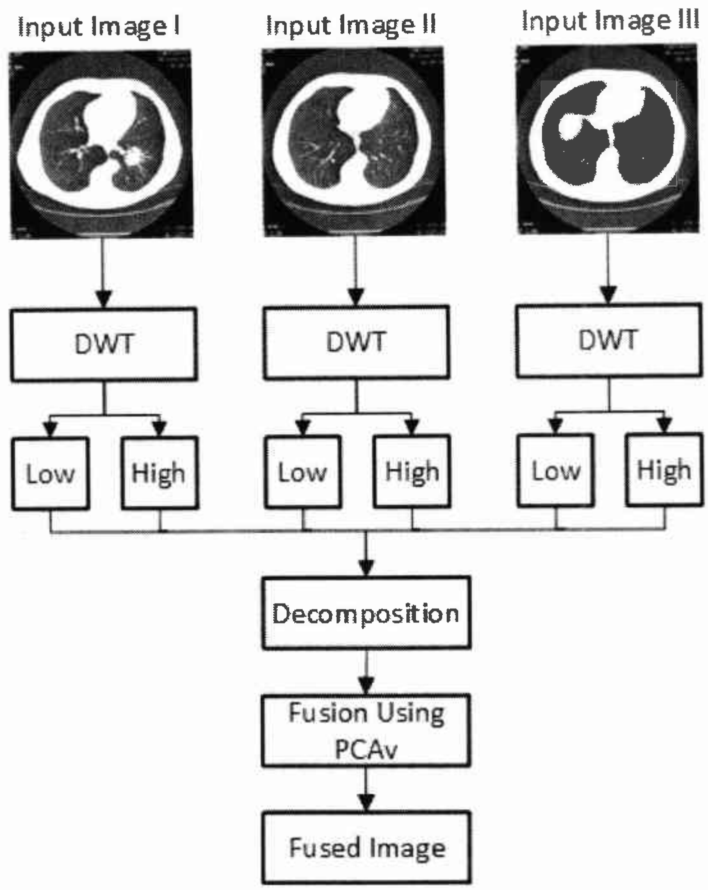

Figure 4.4: DWT-PCAv fusion process

The following are the key steps:

1. In the beginning, DWT is used to decompose CT input images into two or three stages.

2. After that, PCA is used to obtain detailed coefficients and approximation components.

3. Multiple multi-view source images classify each principle element of corresponding coefficient elements.

4. PCAv technique is used to determine the average coefficient components.

5. Using the mean and averaging principal components to implement the PCAv fusion approach.

6. Use fusion quality evaluation metrics to measure the quality of the merged image.

Consider the instance where X_i^1 , X_i^2 and X_i^3 are coefficients written as a matrix column and are generated from LL decomposition levels from three medical image sources. The components of the initial medical image, X_i^1, the components of the second medical image X_i^2 and the components of third medical image X_i^3 are included within a matrix. Where j denotes the number of approximation coefficients.

$$X_i^1 = LL^1 = \left[x_1^1, x_2^1, x_3^1, \ldots, x_j^1\right] \tag{4.1a}$$

$$X_i^2 = LL^2 = \left[x_1^2, x_2^2, x_3^2, \ldots, x_j^2\right] \tag{4.1b}$$

$$X_i^3 = LL^3 = \left[x_1^3, x_2^3, x_3^3, \ldots, x_j^3\right] \tag{4.1c}$$

The average sample values μ^1, μ^2 and μ^3 are calculated as

$$\mu_{x_i}^1 = \left(\frac{1}{j}\right)\sum x_i^1 \quad , \quad \mu_{x_i}^2 = \left(\frac{1}{j}\right)\sum x_i^2 \quad and \quad \mu_{x_i}^3 = \left(\frac{1}{j}\right)\sum x_i^3 \tag{4.2}$$

The co-variance of three vectors are calculated as.

$$\operatorname{cov}(X_i^1, X_i^2) = E[\left(x_i^1 - \mu_x^1\right)\left(x_i^2 - \mu_x^2\right)] \tag{4.3}$$

$$\operatorname{cov}(X_i^1, X_i^3) = E[\left(x_i^1 - \mu_x^1\right)\left(x_i^3 - \mu_x^3\right)] \tag{4.4}$$

$$\operatorname{cov}(X_i^2, X_i^3) = E[\left(x_i^2 - \mu_x^2\right)\left(x_i^3 - \mu_x^3\right)] \tag{4.5}$$

$$E[(X_i^1, X_i^2), (X_i^1, X_i^3), (X_i^2, X_i^3] = \begin{bmatrix} E_{11} & E_{12} & E_{13} \\ E_{21} & E_{22} & E_{23} \\ E_{31} & E_{32} & E_{33} \end{bmatrix} \tag{4.6}$$

Diagonal matrix can be define as E which contains the Eigen values. p denotes the decomposition levels. n_1, n_2 and n_3 are determined from estimation coefficients, elements in the following equations. After calculating all of the n_1, n_2 and n_3 components, the average of these elements is calculated from the given below equations. The final medical image is fused using the PCAv with valuable assessment details in the final stage.

If $E_{11} > E_{22} > E_{33}$

$$\begin{aligned} n_1(LL_p^1) &= \frac{E(1,1)}{E(1,1)+E(2,1)+E(3,1)}; \\ n_2(LL_p^2) &= \frac{E(2,1)}{E(1,1)+E(2,1)+E(3,1)}; \\ n_3(LL_p^3) &= \frac{E(3,1)}{E(1,1)+E(2,1)+E(3,1)} \end{aligned} \tag{4.7a}$$

if E_{33} is the greatest among all the Eigen values then

$$\begin{aligned} n_1(LL_p^1) &= \frac{E(1,3)}{E(1,3)+E(2,3)+E(3,3)}; \\ n_2(LL_p^2) &= \frac{E(2,3)}{E(1,3)+E(2,3)+E(3,3)}; \\ n_3(LL_p^3) &= \frac{E(3,3)}{E(1,3)+E(2,3)+E(3,3)} \end{aligned} \tag{4.7b}$$

4.3.3 Lung Nodule Detection and Classification

Detection of pulmonary nodules can be done using different techniques including image segmentation, image matching and image enhancement technology. The structure of the lung parenchyma region contains vascular tissue, bronchial tissue and pulmonary nodules. So, unlike the previous detection methods, there is a need of more precise algorithm because it can directly affect the results of our classification system. Most intolerable thing for a radiologist is a missed nodule which can be potential cancerous nodule. Therefore computer-aided detection system can rather detect erroneously but should not miss any potential candidate nodule is the primary requirement of the system.

4.3.3.1 Lung Nodule Segmentation

Lung nodule segmentation was an important step for the detection of nodule. In order to achieve this, we implemented optimal thresholding which was followed by contour correction and labeling of connected components. The following steps were adopted for the lung nodule segmentation:

1. Initially, the lung volume was evaluated by using the component labeling approach after the fused CT images has been segmented using optimal thresholding.

2. We obtained a lung CT image having body and non-body areas after applying the optimal thresholding. Black belongs to the body area, whereas white belongs to the non-body area. The first and second biggest lung volumes were identified using connected component labelling on a thresholded image. The majority of the undesirable non-body areas were ignored while choosing the volume.

3. The final image after background removal has holes in the lung lobes that might contain prospective nodules. Morphological operations were used to filled the holes for the accurate detection of nodules.

4. Finally, the rolling ball algorithm were used to smooth the lung juxta pleural nodes.

4.3.3.2 Extraction of Nodule Candidates

There were determined to be three different kinds of lung nodules: isolated, juxta-pleural, and juxta-vascular. By using suggested approach, there were further sub-steps involved for the extraction of lung nodules. In first step, improved Ostu's method was used for grouping and labeling of lung nodule. After that dot-shape selective enhancement filter was used to distinguish the spherical, tubular, and planner structure of nodules. The optimal thresholding was used to detect the nodules. Finally, a rule-based analysis has been performed to select whether to keep or discard the detected nodule based on area, volume, and diameter. A nodule candidate with a volume more than 30 mm should be recognized as a mass or non-nodule since nodules range in size from 3 to 30 mm. Following rule-based analysis, many features from prospective nodule candidates were selected and applied to train the GA-CNN classifier.

4.3.3.3 Stage Classification of Lung Nodule

Final resultant segmented lung nodules images were used as input in our proposed GA-CNN multi-layer method. We have employed six CNN layers, with one convolutional layer and one global average-pool layer in each layer. The suggested GA-CNN algorithm used to investigate 3x3 kernel function to categories the stages of lung tumors. We trained our proposed model in each of the 30 epochs. By using the factor value of 10 epochs, the learning rate μ in each of the 8 epochs was reduced using the proposed model. Firstly, the input image of (height × width × depth) 512 × 512 × 8 pixels was given to the proposed GA-CNN model with 0.2 dropout and 8192 units of fully connected layer used to classify and achieve the 98.2% accuracy in the classification of lung cancer stage. Therefore, our proposed model achieved the accuracy to predict the early cancer stage.

Proposed GA-CNN model has been widely employed with numerous configurations, depending on the number of convolutional layers used in this model. The analysis was performed after CNN tested with one convolution layer. Then, CNN with two layers was used, and its findings were assessed. This technique was applied until the model's output became efficient and more precise. The final GA-CNN model was composed of six convolutional layers using global average pooling layer. With respect to size of the nodules, proposed GA-CNN classified into four stages for detection of lung cancer as shown in Table 4.1. In order to increase accuracy, we used the fused segmented image and then forwarded it to our proposed GA-CNN model.

Table 4.1: Classification of lung cancer stages based on size

Cancer stage	Size of nodules
STG-1	3 to 10 mm
STG-2	>10mm to <15 mm
STG-3	>=15mm to <25 mm
STG-4	>=25mm

4.3.3.4 Cross Validation Set

In this proposed method, the 10-fold cross validation approach were used. Nine sets were utilised for training and one set was used for validation with a repeat of 15 epochs in the 10-fold cross validation set. There will be 150 epochs in total for the training operations with a batch size of 10. For the cross validation set, we fold our dataset into a set of images that is 10 folds. Using the same dataset of images, we examined folds 1, 4, and 6, and the findings were less accurate than those of the other fold sets. The accuracy, precision, and recall performance metrics for 10-fold cross-validation with the mean value are shown in Table 4.2.

Table 4.2: Performance metrics for 10 fold cross-validation

K- fold	Precision (%)	Recall (%)	Accuracy (%)
1-fold	97.5	96.4	96.5
2-fold	98.7	98.1	99.5
3-fold	99.3	97.3	99.7
4-fold	97.4	96.4	96.3
5-fold	99.2	97.7	99.6
6-fold	99.7	96.2	96.1
7-fold	97.8	97.6	98.1
8-fold	97.9	97.4	99.6
9-fold	97.1	97.4	98.6
10-fold	98.6	98.3	98.0
Mean value	98.32	97.28	98.20

4.4 Results and Discussions

For the evaluation of the proposed technique, LIDC dataset is used for our proposed methodology, which has DICOM image format [21]. In the section 4.4.1 LIDC dataset will be discussed in detail. The performance parameters will also be discussed which are used for the evaluation of proposed technique. The results of the proposed technique are presented and also compared with the results of other techniques in details. The environment for the experimental work was MATLAB 2016a and Dell Latitude E6230 G3 Intel Core i5 3340M, CPU 2.70 GHz with 16GB RAM.

4.4.1 Imaging Database

The LIDC is commonly used to evaluate proposed techniques as it reveals in literature review. The Cancer Imaging Archive (CIA) hosts LIDC which is freely accessible on the website of TCIA [194]. This dataset comprises of 4,682 CT Scan images of 61 patients of lung cancer, which include nodules ranging in size from 3 to 30 mm that four expert radiologists annotated in two sessions. Each patient has 60-120 slices, each of which is 512x512 pixels in size and has 4096 grey levels in HU. Pixel spacing ranges from 0.78 mm to 1 mm, with a 1-3 mm reconstruction interval.

4.4.2 Performance Parameters

The proposed model is validated using the metrics like MI, FMI, NCC, Peak Signal to Noise Ratio (PSNR), Structural Similarity Index Metric (SSIM), and Root Mean Square Error (RMSE). MI decides how information from source images and fused images are combined [195]. If the source and resultant images are independent then the MI will be zero [196]. More information are common between the source and resultant images if the MI is higher. MI can be expressed as [197].

$$MI_{xy} = Gx + Gy - Gxy \tag{4.8a}$$

$$MI_O = MI_{OX} + MI_{Oy} \tag{4.8b}$$

Where G_x indicates the joint entropy of image X and G_y means the joint entropy of image Y, and G_{xy} denotes the joint entropy of image X and Y. MI_{xy} signifies the mutual knowledge between the source and the consequent image. Similar to this, Eq. 4.8b defines MI of the fused image, which is MI_O. PSNR is an RMSE-based quantitative measure. PSNR calculates the ratio of intensity levels in medical images to the corresponding pixels in the final image. A higher PSNR value indicates higher quality fusion or registration.

$$PSNR = 10 * \log_{10}\left(\frac{(f_{\max})^2}{RMSE}\right) \tag{4.9}$$

The highest pixel grey levels quantity in the fused image is indicated by f_{max}. The $SSIM$ estimates the similarity among two regions z_x and z_y in images X and Y. Where $\bar{z}_x$ and $\bar{z}_y$ are the local means, $\sigma z_x z_y$ is the standard deviation, h_1 and h_2 are the positive constants.

$$SSIM_{(x,y|z)} = \frac{(2\bar{z}_x\bar{z}_y + h_1)(2\sigma z_x z_y + h_2)}{(\bar{z}_x^2 + \bar{z}_y^2 + h_1)(\sigma^2 z_x + \sigma^2 z_y + h_2)} \tag{4.10}$$

MI calculates features from the resultant fused image. It showed how various edges, curves, and additional characteristics were added to the fused image from the source images. The efficiency of the resultant fused image is proportional to the value of FMI, which can be expressed in the following way mathematically.

$$FMI_O = FMI_{OX} + FMI_{Oy} \tag{4.11}$$

FMI_O represents for the attributes of the final image that were transferred from the source images X and Y. Images X and Y have the characteristics FMI_{OX} and FMI_{Oy} respectively. By comparing the final fused image to the ground truth image, RMSE calculates the image's quality. Where $S(i,j)$ is the resultant fused image and $O(i,j)$ are the original input images. Its value should be closer to zero for successful fusion performance.

$$RMSE = \sqrt{\frac{1}{MN}\sum_{i=o}^{M-1}\sum_{j=0}^{N-1}(S(i,j) - O(i,j))^2} \tag{4.12}$$

4.4.3 Multi-Resolution Rigid Registration (MRR) Results

Figure 4.10 shows the pre-processed enhanced image. After pre-processing, registration is the most crucial step. Registration affects the fusion efficiency as well. Intensity-based registration works well with multi-view image registration. Both rigid registration techniques are applied on CT lung images. These approaches were chosen because full image alignment can be completed rapidly, whereas time complexity is not an issue in SRR. But, the quality of image registration is compromised.

In order to evaluate improved registration outcomes, the visual consequences of lung registered images with an absolute difference are exhibited. It is observed that these outcomes are suitable for human perception. Figure 4.5 shows the results of MRR technique implemented on different lung CT images of patients. Each set of CT images is divided into three parts from (a-i), [Left] side shows the source image, [Center] side shows the thick boundary identification, and [Right] side shows the resultant images after applying the MRR technique while 4.3 represents the results of image registration quality assessments measures. Furthermore, statistical analyses is performed to show which technique produces significant results in the registration process. In most circumstances, the MRR performs better. MI, CC, SSIM, NCC, PSNR, SSD, and RMSE are the seven registration quality assessment measures that have been chosen for validation. Both registration methods' computing costs are also computed. For better image registration, the values of MI, CC, SSIM, NCC, and PSNR should be high, while the values of SSD, RMSE. Table 4.3 displays the statistical results of lung image registration.

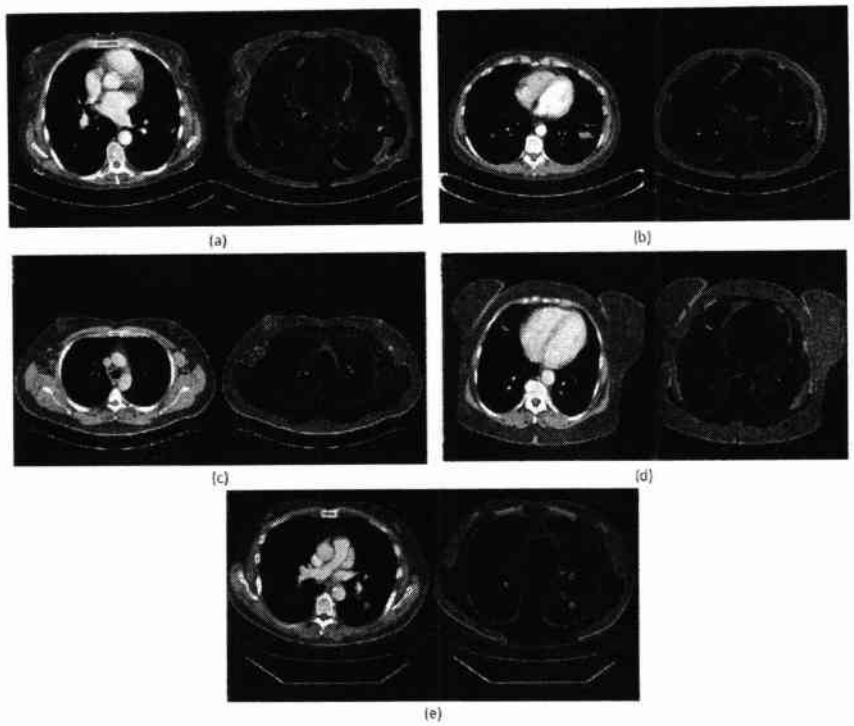

Figure 4.6: Set-1: Multi-view image registration of lung CT images using SRR method with different performance parameters

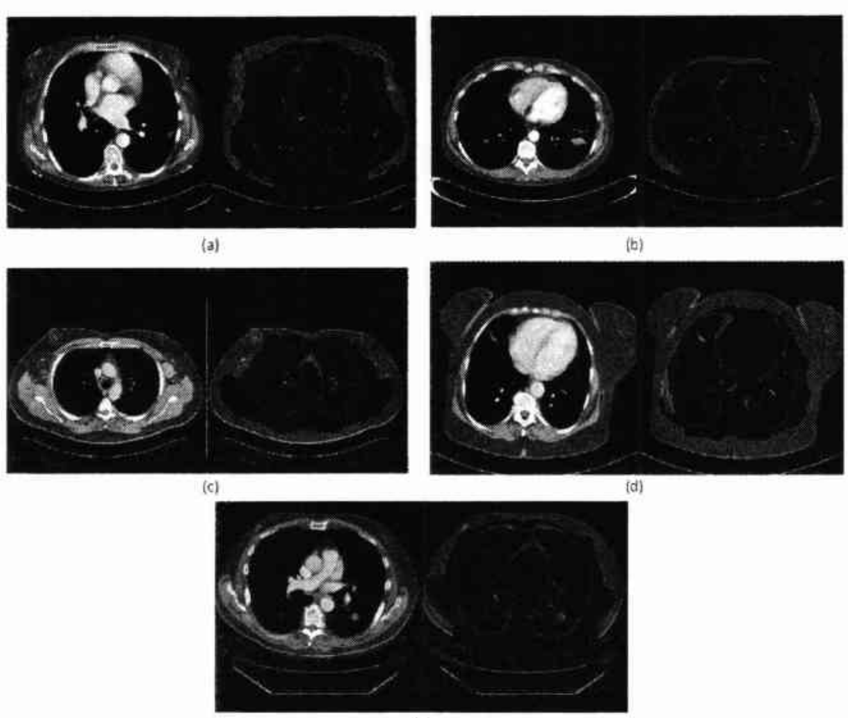

Figure 4.7: Set-2: Multi-view image registration of lung CT images using SRR method with different performance parameters

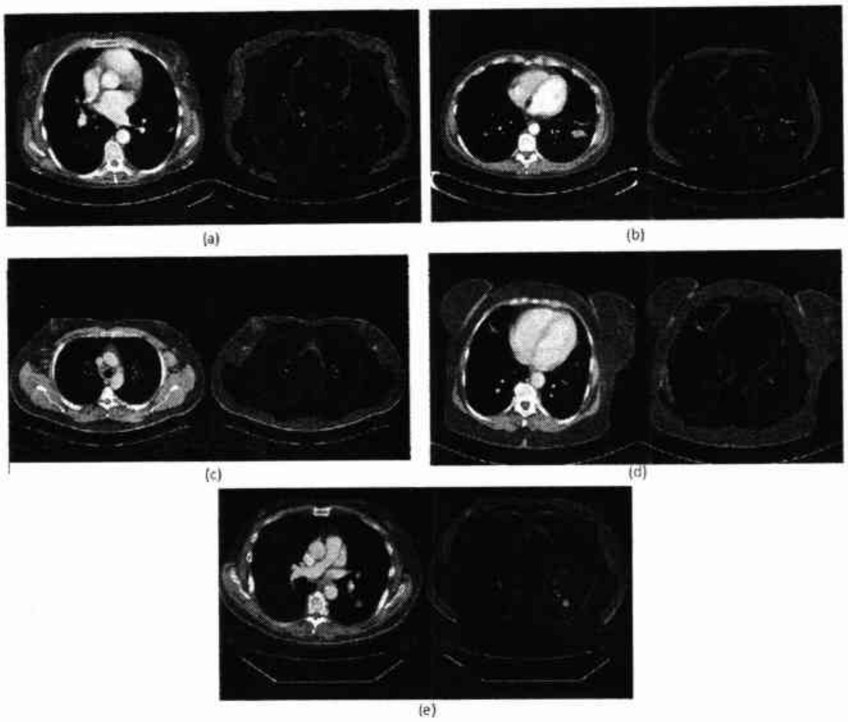

Figure 4.8: Set-1: Multi-view image registration of lung CT images using MRR method with different performance parameters

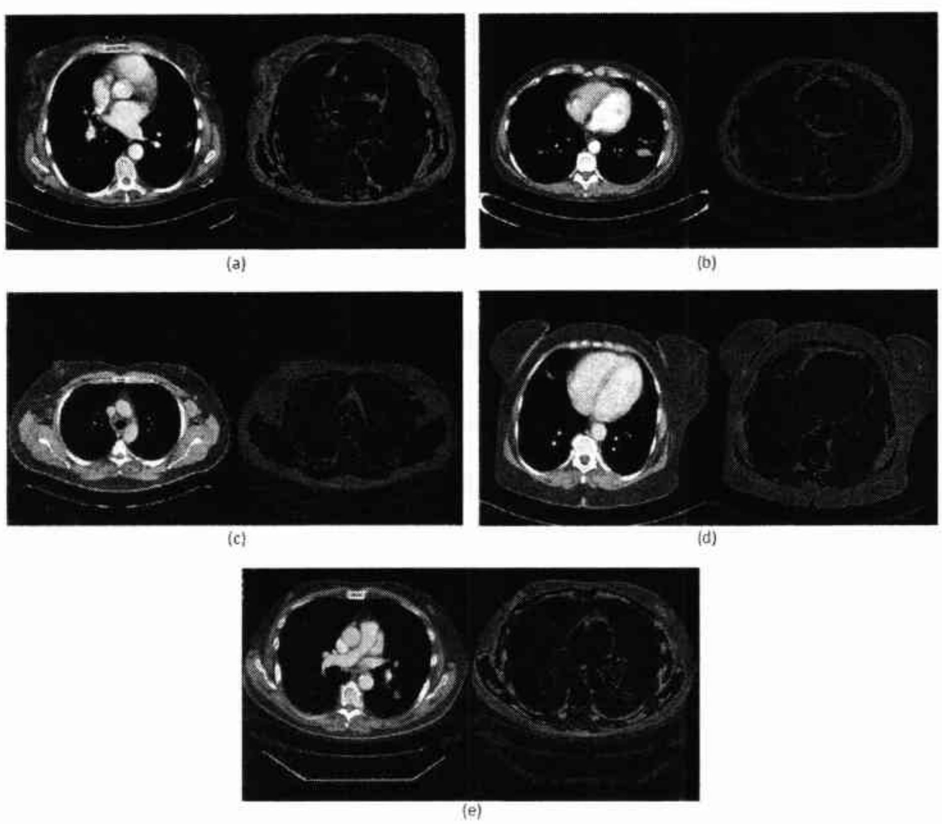

Figure 4.9: Set-2: Multi-view image registration of lung CT images using MRR method with different performance parameters

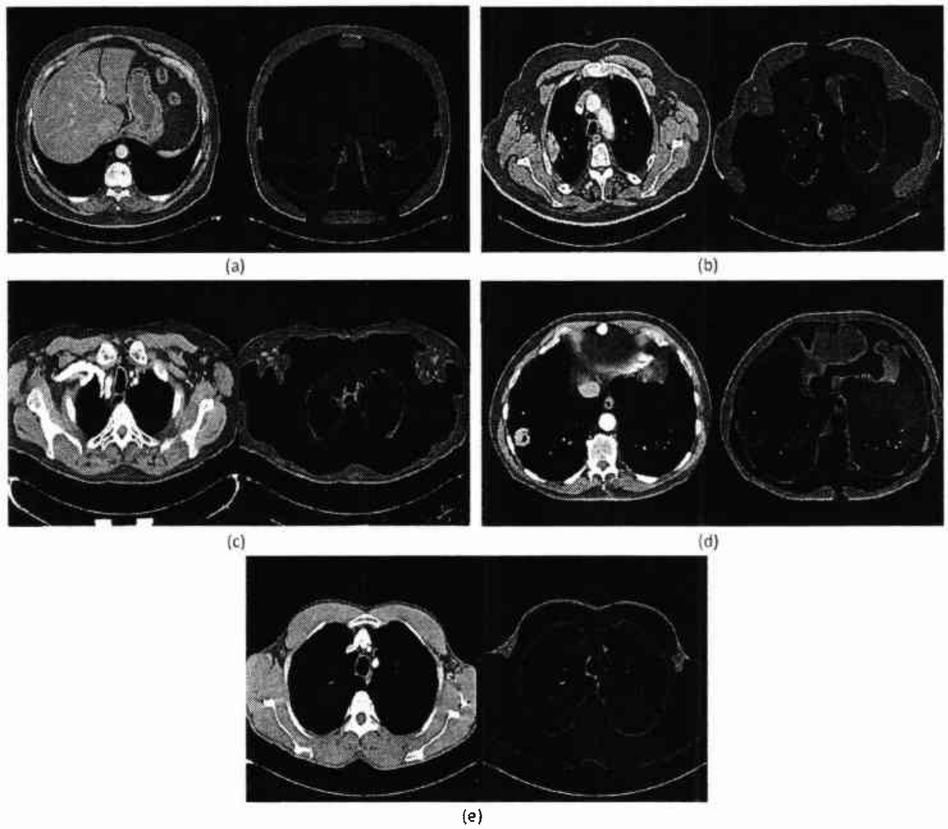

Figure 4.10: Set-3: Multi-view image registration of lung CT images using MRR method with different performance parameters

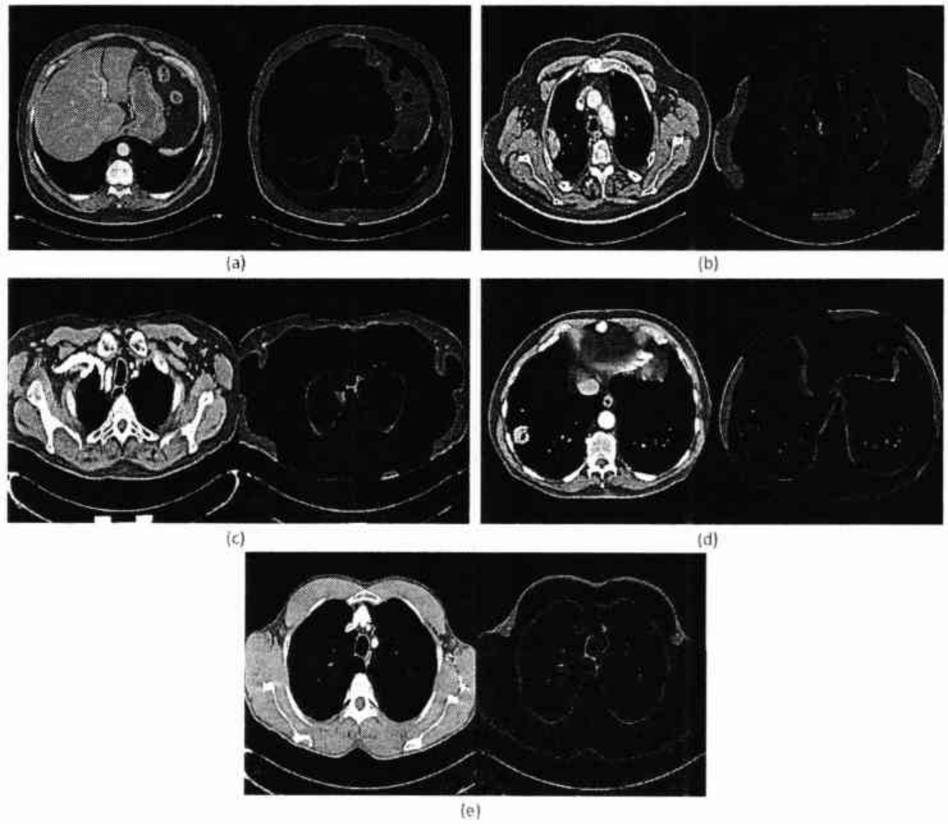

Figure 4.11: Set-4: Multi-view image registration of lung CT images using MRR method with different performance parameters

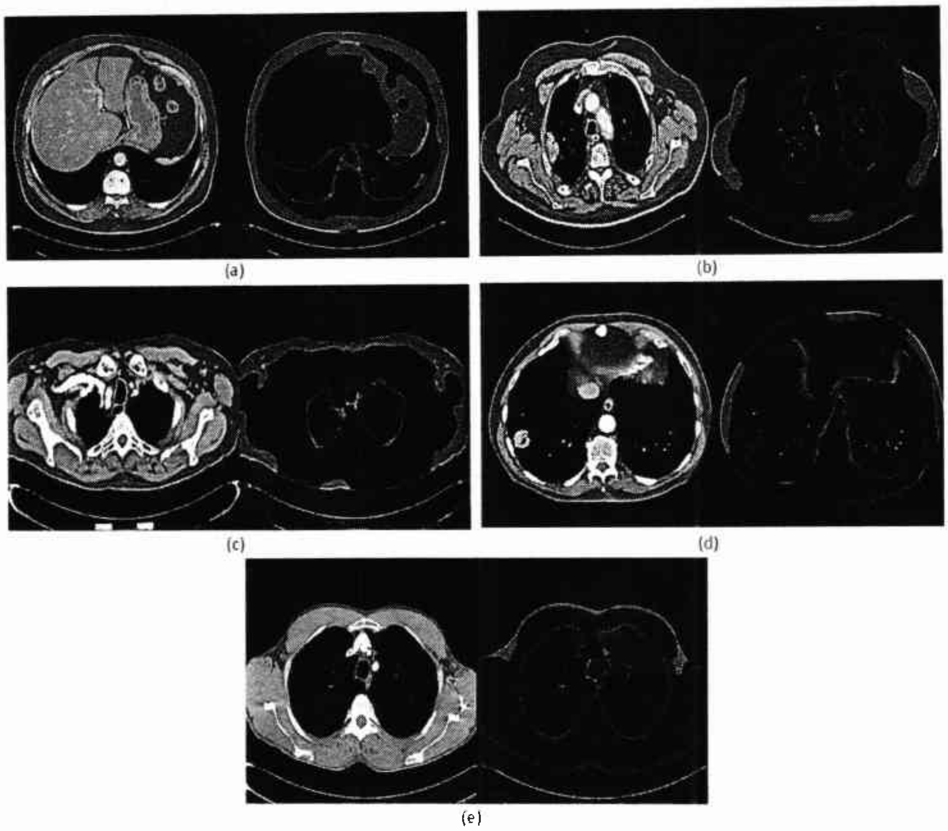

Figure 4.12: Set-5: Multi-view image registration of lung CT images using MRR method with different performance parameters

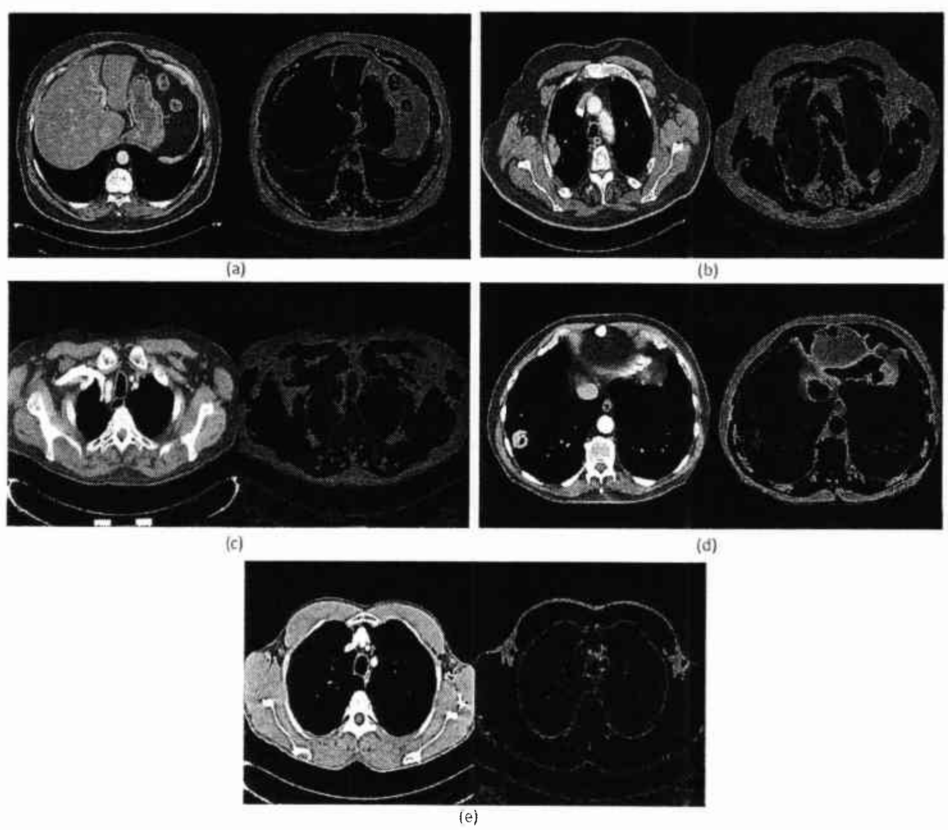

Figure 4.13: Set-6: Multi-view image registration of lung CT images using MRR method with different performance parameters

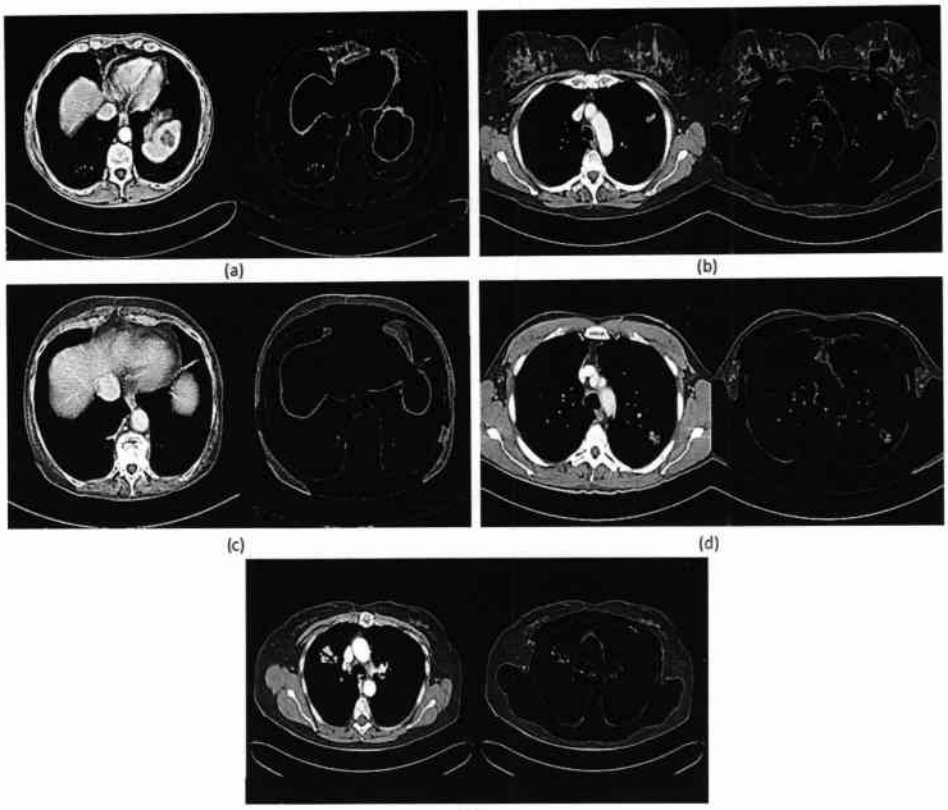

Figure 4.14: Set-7: Multi-view image registration of lung CT images using MRR method with different performance parameters

Table 4.3: SRR and MRR Technique comparison on multi-view lung CT images

Techniques	Source Images					
	Source Image-1		Source Image-2		Source Image-3	
	SRR	MRR	SRR	MRR	SRR	MRR
Mutual Information (MI)	1.165	1.186	1.154	1.167	1.15	0.93
Co-relation Co-efficient(CC)	0.88	0.89	0.91	0.92	0.74	0.81
Structure Similarity Index Method (SSIM)	0.77	0.79	0.81	0.82	0.57	0.60
Normalized Cross Correlation (NCC)	0.93	0.94	0.95	0.96	0.92	0.94
Peak Signal to Noise Ratio(PSNR)	30.91	40.43	32.35	43.34	27.62	30.42
Sum of Square Distance (SDD)	9.41e + 09	9.20e+ 09	7.78e + 09	7.04e + 09	1.17e + 09	1.17e+ 09
Root Mean Square Error (RMSE)	0.033	0.033	0.032	0.032	0.035	0.035

The proposed strategy produces significant results than the other methods tested. The assessment metrics MIF, CC, FMI, SSIM, NCC, PSNR, and RMSE are chosen in Table 4.4 to compare the statistical results of the suggested methodologies with state-of-the-art fusion methods. Image fusion evaluation parameters were then compared with previous methodologies (Symlet wavelet [198], Daubechies wavelet [47], Dual tree complex wavelet [46] and proposed method). For MIF, CC, FMI, SSIM values are 1.58, 0.91, 0.80, 0.81, respectively. SSIM values are 0.53, 0.34, 0.29 0.15. In NCC values were 1.74, 2.10, 0.25, and 0.73. Moreover, PSNR values were 12.26, 10.00, 42.98, and 10.25 simultaneously. RMSE was also calculated and values were 0.62, 0.80, 0.02, and 0.02 correspondingly. It has been observed that the proposed technique, for the most part, yields satisfactory outcomes.

Table 4.4: Image fusion quality assessment result of multi-view CT images by using different fusion method

Fusion Techniques	LIDC			
	Symlet wavelet	Daubechies wavelet	Dual-tree complex wavelet transform	Proposed Method
Medical Image Fusion (MIF)	-	-	-	**1.58**
Co-relation Co-efficient (CC)	-	-	-	**0.91**
Feature Mutual Information (FMI)	-	-	-	**0.80**
Structure Similarity Index Method (SSIM)	0.53	0.34	0.29	**0.81**
Normalized Cross Correlation (NCC)	1.74	1.74	0.25	**0.73**
Peak Signal to Noise Ratio(PSNR)	12.26	10.00	**42.98**	10.25
Root Mean Square Error (RMSE)	0.621	0.806	**0.02**	**0.02**

Table 4.5: Objective metrics of multi-view medical image fusion

Techniques	Data set	$Q^{AB/F}$	$(L_{AB/F})$	$(N^m_{AB/F})$	Q^{TE}	Q^{IE}	VIF
Nazir et al[203]	LIDC	0.79	0.16	0.01	-	-	-
Proposed method	LIDC	**0.850**	-	-	0.546	0.809	1.76

Figure 4.15 explains how metrics of each fusion quality evaluation should be high to produce superior image fusion outcomes, with the exception of computation time. Better fusion necessitates a low computation time value. The majority of current fusion methods are computationally intensive. Compared to other existing methodologies, the suggested methodology requires less calculation time. The image fusion computation time is measured in seconds. It is determined by the parameters of algorithm and the hardware and software specifications.

4.4.4 Evaluation of Objective Metrics

A single assessment metric cannot accurately represent the quality of the fused image for quantitative evaluation. As a result, a variety of measures are used to provide a thorough review. The performance of several fusion approaches is quantitatively evaluated in this research using six widely used measures, which are $(L_{AB/F})$, $(N^m_{AB/F})$, Q^{TE} [199], Q^{IE} [200], $Q^{AB/F}$ [201] and VIF [202]. The Tsallis entropy and nonlinear correlation information entropy of fused images are assessed using the functions Q^{TE} and Q^{IE}, respectively. The edge information is measured using $Q^{AB/F}$, VIF assesses many elements of how well humans can visualise fused images. The ratio of referenced image information to distorted testing image information is represent as VIF. Whereas, the total loss of the image was determined using $L_{AB/F}$, and the level of noise and other related artifacts was calculated using $(N^m_{AB/F})$ [172].

Six indicators are used in this research to assess the performance of the fusion. The average values of previous and proposed method for multi-view CT image fusion are shown in Table 4.5. The proposed method achieves the higher $Q^{AB/F}$ value than other method.

4.4.5 Result of Image Fusion By Using DWT-PCAv

Using DWT-PCAv, the multi-view image fusion of lung CT images is shown in Figure 4.15. Original CT lung image of patients (1-5) is shown in column 1. These images have low contrast and a lot of colour misrepresentation. Column 2 shows segmented images of patients (1-5). The third column shows the resultant fused images of patients (1-5) with detailed information. The proposed method also preserves much information that helps doctors diagnose the disease. The evaluation parameters MIF, CC, FMI, SSIM, NCC, PSNR, and RMSE in Table 4.4 are calculated and compared the proposed method with different image fusion techniques, i.e., Symlet wavelet, Daubechies wavelet and Dual-tree complex wavelet transform. For MIF, CC, and FMI the value were 1.58, 0.91, and 0.80. In SSIM proposed method showed uppermost value (0.81), however, Dual-tree complex wavelet contained the lowest value (0.29). NCC contains the best value (0.73) by using our proposed method whereas Symlet wavelet and Daubechies wavelet showed the values (1.74). Moreover, PNSR has the highest value (42.98) for Dual-tree complex wavelet whereas, Daubechies wavelet had the lowest value (10.00). For RMSE, Daubechies wavelet is having highest value 0.806 and the lowest value for this parameter is 0.019 by using our proposed method.

4.4.6 Results of GA-CNN Classifier

In the LIDC/IDRI dataset, 61 cases included 2341 CT images. The proposed GA-CNN model detected 1423 lung nodules. The nodules with sizes ranging from 3 to 30 mm (512 × 512 pixels) were used in this model. The CT lung images with solid, semisolid, and non-solid nodules were all categorized using the LIDC-IDRI data collection. GA-CNN classified the nodules as "well-circumscribed, juxta vascular, juxta pleural, pleural tail" Table 4.6showed the number of solid nodules, semisolid nodules, and non-solid nodules.

Our proposed model detected 1398 out of 1423 nodules, which showed the detection rate of

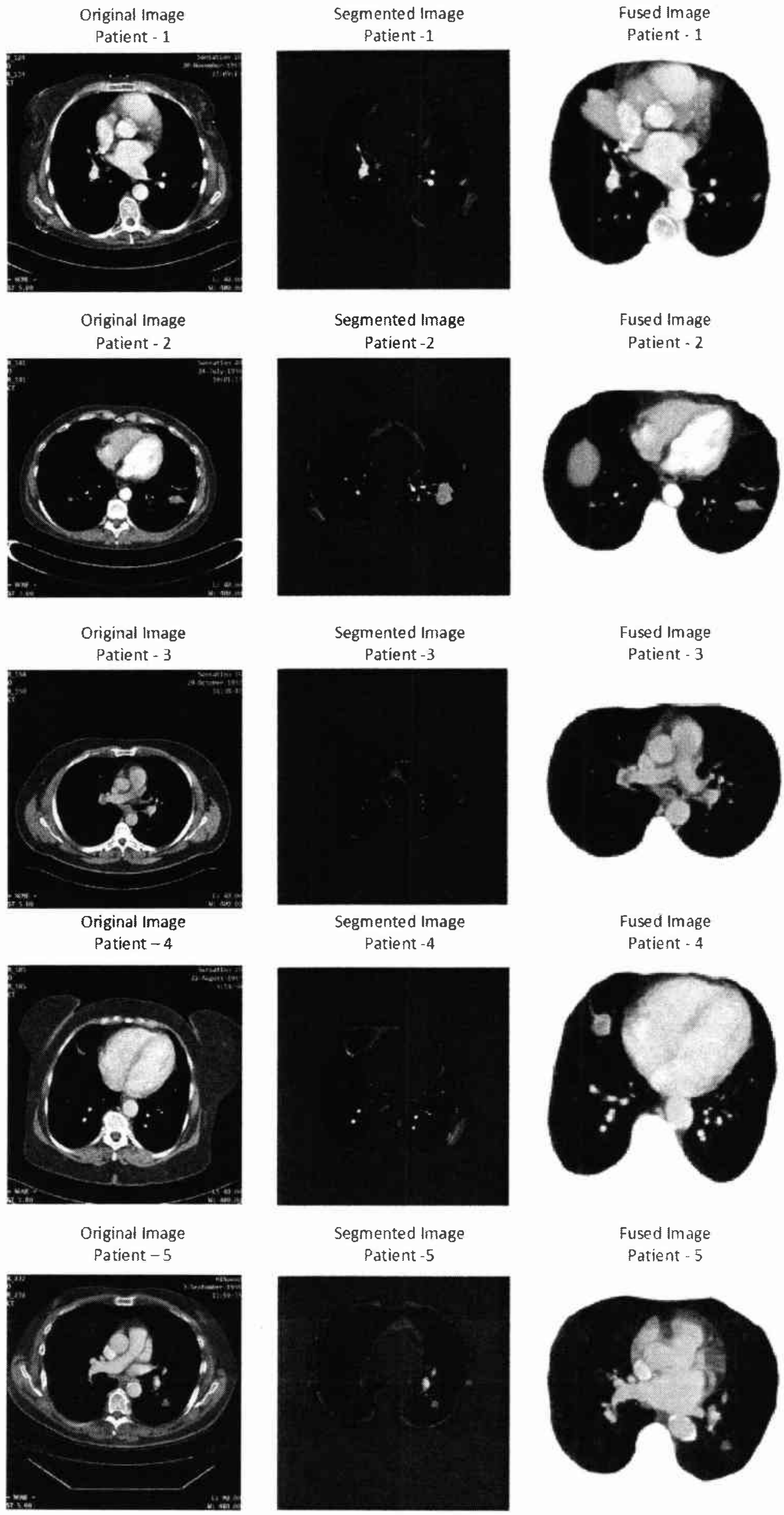

Figure 4.15: Multi-view image fusion of lung CT images by using DWT-PCAv

Table 4.6: Various types of lung nodules

Solid nodules	Semi-solid nodules	Non-solid nodules	Total nodules
513	609	301	1423

Table 4.7: Classification results of lung cancer stages based on nodule size

Cancer stage	Size of nodules	Total nodules
STG-1	3 to 10 mm	708
STG-2	>10mm to <15 mm	290
STG-3	>=15mm to <25 mm	304
STG-4	>=25mm	96

98.2 % with 1.8 % FP/scan. The total number of false positive (missed nodules) by the proposed model were 25. The GA-CNN model classified the nodules with respect to size and internal structure. Result has been summarized in the table 4.7 through GA-CNN classifier. In stage-1 (STG-1), total 708 nodules classified within range of size from 3 to 10 mm, while in stage-2 (STG-2) total 290 nodules classified as per defined size range. Moreover, in stage-3 (STG-3) and stage-4 (STG-4), total 304 and 96 nodules classified using GA-CNN respectively. Due to the use of non-uniform performance metrics and various assessment criteria, such as the dataset and types of nodules taken into consideration, we concluded that it is very difficult to compare the findings with earlier work that has been published. Despite this limitation, we attempted to compare the performance of our suggested system with the existing Lung CAD systems, as shown in table.4.8. The proposed model performed well in terms of accuracy, sensitivity, and specificity, obtaining values of 98.2%, 96.4%, and 97.2%, respectively, but underperformed in terms of false positives, with a value of 1.8 FP/scan. Each test set is different, with training samples comprising 20–70% of images and testing samples comprising 10–40% of images. The proposed model significantly outperformed than "3D-CNN, 2D-CNN, SVM, ANN, and CNN" suggested by other authors included in the summary Table 4.8.

Table 4.8: Performance comparison between proposed and existing CAD systems with nodule size 3-30(mm)

Method	**Dataset**	**Classifier**	**Accuracy**	**Sensitivity**	**Specificity**	**FPs/Scan**	**Nodules**
Proposed Method	LIDC-IDRI	GA-CNN	**98.2**	**96.4**	97.2	1.8	1398
Eali Stephhen[204]	LUNA	3D CNN	89.0	83.5	80.5	-	-
Naqi et al [177]	LIDC-IDRI	SVM	96.9	95.6	**97.0**	2.8	777
Gopi et al.(2022)[205]	LIDC-IDRI	M-CNN	97.0	84.7	81.7	**1.7**	-
Xie et al [178]	LUNA16	2D CNN	-	83.0	-	8.0	-
Shaukat et al [102]	LIDC	SVM	93.7	95.5	94.28	5.27	148
Zhang et al [96]	LIDC-IDRI	SVM	93.6	89.3	-	2.1	168
Ali et al [98]	LIDC-IDRI	ANN	64.4	58.9	55.3	-	888
Teramoto [179]	Clinical	SVM	-	83.0	-	5.0	186
Acharya et al.[206]	EPILEPSIAE	CNN	88.7	82.61	78.61	-	-

Our suggested GA-CNN model outperformed other methods based on performance measures, and this was attributable to the effective tumour stage classification, segmentation, and fusion techniques used in the lung tumour. By utilising CT scans images of lung tumours, this suggested method helps produce a precise tumour detection. The time complexity of the suggested technique is $O(p^2)$ and the overall processing time is 1800 seconds, where p is the number of pixels in the segmented fused image.

4.5 Conclusion And Impending Work

Compared to classification methods, the proposed methodology for image registration and fusion aims to reduce the number of manual inspections while increasing the precision of the auto process. The proposed MRR eliminates the SRR's drawback. The SRR is a time-saving method, but it comes with the risk of mis-registration. The fusion phase uses the MRR recorded image as an input. By fusing three lung images thus preserving important details, the PCAv fusion technique enhances the image quality. PCAv fusion also has the benefit of being time-saving. The suggested technique is applied on whole dataset of lung images, one of which contains regular source images, the second contains the segmented images, and the last one is the final resultant fused images. Established fusion approaches are contrasted with the proposed approach. Visual and statistical representations of the image registration and fusion results are given. Moreover, suggested GA-CNN model for nodule classification were applied unsupervised learning neural networks as a predictor and stage classifier to detect nodule more accurately. The accuracy, sensitivity, and specificity of the performance metrics were calculated, and compared with the existing approaches. The findings indicate that stage categorization for evaluated segmented fused images was 98.2% accurate. In comparison to other existing techniques, the proposed approach shows potential. Researchers will continue to work on non-rigid registration in this field and apply their findings to other image modalities procedures. For improved results, this study may be integrated with machine learning models, such as the quick and portable 3D CNN. The cutting-edge research can be applied to a variety of current diseases including COVID-19 and its effects on lung psychology.

Chapter 5

Conclusion and Future Work

5.1 Conclusions

In this dissertation different methods are proposed for lung cancer detection and staging. For this the major steps are segmentation, features extraction and classification. In proposed method multi-view image fusion techniques along with SVM and GA-CNN classifiers for early lung cancer detection are used.

In the proposed method for lung cancer detection adaptive global threshold is used without post image processing. The proposed method uses LP decomposition and ASR approach for multi-view image fusion. In the proposed method, dictionaries are built in each layer using LP method. This reduces the effect of background, noise and block impact. From the lung nodule candidates, the features like shape, intensity, and texture information are extracted by using SVM. The experimental results reveal that the sensitivity of the proposed method is 97.9%, with 2 false positive per scan which is better than the existing methods.

To improve the image quality, an image fusion technique is proposed based on the PCAv which fuses three lung images without loosing clinical information. Before fusion the images, MRR technique is used for image registration. The fused image is used for lung cancer detection and staging. A GA-CNN classifier is used for the lung nodule detection and staging. The experimental result shows that the accuracy of the proposed method is 98.2%, with 1.8 false positive per scan which is also promising results.

5.2 Future Work

There is still has a lot of research work space to be done in CAD system before a commercial product can be developed and used in hospitals. Following are the future work directions:

1. It is necessary to build a more comprehensive local template library for lung nodules in order to conduct future research and development on the segmentation of suspected nodules. Recently, some researchers have assembled different types of nodule patterns and experimented with assembling a library of nodule templates, but the primary issue they have run across is the diversity in nodule features.

2. The proposed methods could also be used to detect problems in tissue patterns, including endobronchial nodules, carcinomas showing as uneven wall thickening of lung bullae and hilar lesions. The fundamental problem with these diseases is that a limited dataset is available.

3. The CAD system needs to be tested on adequately large dataset to increase robustness, and after that, the results on how the system is capable of safely managing hospital real-time clinical tests must be published. The radiologists should also be taken into loop for the validity of the results.

4. Multi dimensional image reconstruction has become an important aspect of image processing in CAD system. Doctors require more comprehensive multi dimensional imaging systems. The concept of multi-dimensional image reconstruction and segmentation required extensive research.

5. The detection of nodules (less than 3mm) is an another area that requires attention. Future CAD systems needs to be capable of detecting all sizes of nodule (including micro nodules) in

terms of accuracy, sensitivity, specificity, and less FP/scan.

Abbreviations

CT	Computed Tomography
LP	Laplacian Pyramid
ASR	Adaptive Sparse Representative
LIDC-IDRI	Lung Image Database Consortium and Image Database Resource Initiative
PET	Positron Emission Tomography
HRCT	High-Resolution Computed Tomography
CAD	Computer-Aided Detection
GCPSO	Guaranteed Convergence Particle Swarm Optimization
SD	Spatial Domain
TD	Transform Domain
PF	Pyramid Fusion
DWT	Discrete Wavelet Transform
CVT	Curvelet Transform
NSCT	Non-Subsampled Contour Transform
SR	Sparse Representation
SVD	Singular-Value Decomposition
DL-GSGR	Dictionary Learning with Group Sparsity and Graph Regularization
RWT	Redundant Wavelet Transform
R-DWT	Redundant Discrete Wavelet Transform
RMLP	Region Mosaicking on Laplacian Pyramids
NCA	Neighborhood Component Analysis
LDSB	Lung Data Science Bowl
MI	Mutual Information
NCC	Normalized Cross-Correlation

FMI	Feature Mutual Information
PCA	Principal Component Analysis
ROI	Region Of Interest
DICOM	Digital Imaging and Communications in Medicine
RGB	Red Green Blue
DSC	Distributed Source Coding
RD	Region Detection
LSWI	Level Set Without Initialization
RM	Re-initialization Methods
API	Average Pixel Intensity
SD	Standard Deviation
AG	Average Gradient
MI	Mutual Information
SF	Spatial Frequency
BiSe-Net	Bilateral Segmentation Network
SVM	Support Vector Machine
GA-CNN	Global Averaging - Convolutional Neural Network
STG	Stage

5.3 Bibliography

[1] Rebecca L Siegel, Kimberly D Miller, and Ahmedin Jemal. Cancer statistics, 2016. *CA: a cancer journal for clinicians*, 66(1):7–30, 2016.

[2] Joey Mark Diaz, Raymond Christopher Pinon, and Geoffrey Solano. Lung cancer classification using genetic algorithm to optimize prediction models. In *IISA 2014, The 5th International Conference on Information, Intelligence, Systems and Applications*, pages 1–6. IEEE, 2014.

[3] Angela B Mariotto, K Robin Yabroff, Yongwu Shao, Eric J Feuer, and Martin L Brown. Projections of the cost of cancer care in the united states: 2010–2020. *Journal of the National Cancer Institute*, 103(2):117–128, 2011.

[4] F Shaukat and G Raja. An efficient algorithmic solution for automatic segmentation of lungs from ct images. *Pakistan Journal of Science*, 70(1):71–78, 2018.

[5] Chetan Tiwari, Kirsten Beyer, and Gerard Rushton. The impact of data suppression on local mortality rates: the case of cdc wonder. *American journal of public health*, 104(8):1386–1388, 2014.

[6] Malcolm A Moore, Pattarawin Attasara, Thiravud Khuhaprema, TN Le, TH Nguyen, Prak Piseth Raingsey, Supannee Sriamporn, Hutcha Sriplung, Petcharin Srivanatanakul, DT Bui, et al. Cancer epidemiology in mainland south-east asia-past, present and future. *Asian Pac J Cancer Prev*, 11(Suppl 2):67–80, 2010.

[7] D Forman, J Ferlay, BW Stewart, and CP Wild. The global and regional burden of cancer. *World cancer report*, 2014:16–53, 2014.

[8] Muhammad Luqman, Muhammad Mohsin Javed, Shakeela Daud, Nafeesa Raheem,

Jamil Ahmad, and Amin-Ul-Haq Khan. Risk factors for lung cancer in the pakistani population. *Asian Pacific Journal of Cancer Prevention*, 15(7):3035–3039, 2014.

[9] National Lung Screening Trial Research Team. Reduced lung-cancer mortality with low-dose computed tomographic screening. *New England Journal of Medicine*, 365(5):395–409, 2011.

[10] Wook-Jin Choi and Tae-Sun Choi. Automated pulmonary nodule detection based on three-dimensional shape-based feature descriptor. *Computer methods and programs in biomedicine*, 113(1):37–54, 2014.

[11] Igor Rafael S Valente, Paulo César Cortez, Edson Cavalcanti Neto, José Marques Soares, Victor Hugo C de Albuquerque, and Joao Manuel RS Tavares. Automatic 3d pulmonary nodule detection in ct images: a survey. *Computer methods and programs in biomedicine*, 124:91–107, 2016.

[12] William J Kostis, Anthony P Reeves, David F Yankelevitz, and Claudia I Henschke. Three-dimensional segmentation and growth-rate estimation of small pulmonary nodules in helical ct images. *IEEE transactions on medical imaging*, 22(10):1259–1274, 2003.

[13] Claudia I Henschke, Dorothy I McCauley, David F Yankelevitz, David P Naidich, Georgeann McGuinness, Olli S Miettinen, Daniel M Libby, Mark W Pasmantier, June Koizumi, Nasser K Altorki, et al. Early lung cancer action project: overall design and findings from baseline screening. *The Lancet*, 354(9173):99–105, 1999.

[14] S Shaik Parveen and C Kavitha. A review on computer aided detection and diagnosis of lung cancer nodules. *International Journal of Computers & Technology*, 3(3a):393–400, 2012.

[15] Mai Mabrouk, Ayat Karrar, and Amr Sharawy. Computer aided detection of large lung nodules using chest computer tomography images. *Computer*, 3(9):12–18, 2012.

[16] Wook-Jin Choi and Tae-Sun Choi. Automated pulmonary nodule detection system in computed tomography images: A hierarchical block classification approach. *Entropy*, 15(2):507–523, 2013.

[17] Ian A Cunningham. Computed tomography. *Biomed Engineer Handbook*, 1998.

[18] Syed M Naqi and Muhammad Sharif. Recent developments in computer aided diagnosis for lung nodule detection from ct images: a review. *Current Medical Imaging*, 13(1):3–19, 2017.

[19] Kazuo Awai, Kohei Murao, Akio Ozawa, Masanori Komi, Haruo Hayakawa, Shinichi Hori, and Yasumasa Nishimura. Pulmonary nodules at chest ct: effect of computer-aided diagnosis on radiologists' detection performance. *Radiology*, 230(2):347–352, 2004.

[20] Hengmin Jia, Liang Zhang, and Baolong Wang. The value of combination analysis of tumor biomarkers for early differentiating diagnosis of lung cancer and pulmonary tuberculosis. *Annals of Clinical & Laboratory Science*, 49(5):645–649, 2019.

[21] Samuel G Armato III, Geoffrey McLennan, Michael F McNitt-Gray, Charles R Meyer, David Yankelevitz, Denise R Aberle, Claudia I Henschke, Eric A Hoffman, Ella A Kazerooni, Heber MacMahon, et al. Lung image database consortium: developing a resource for the medical imaging research community. *Radiology*, 232(3):739–748, 2004.

[22] Justin Kirby, Fred Prior, Nicholas Petrick, Lubomir Hadjiski, Keyvan Farahani, Karen Drukker, Jayashree Kalpathy-Cramer, Carri Glide-Hurst, and Issam El Naqa. Introduction to special issue on datasets hosted in the cancer imaging archive (tcia). *Medical Physics*, 47(12):6026–6028, 2020.

[23] Michael F McNitt-Gray, Samuel G Armato III, Charles R Meyer, Anthony P Reeves, Geoffrey McLennan, Richie C Pais, John Freymann, Matthew S Brown, Roger M Engelmann, Peyton H Bland, et al. The lung image database consortium (lidc) data collection process for nodule detection and annotation. *Academic radiology*, 14(12):1464–1474, 2007.

[24] Bendong Zhao, Shanzhu Xiao, Huanzhang Lu, and Junliang Liu. Point target detection in space-based infrared imaging system based on multi-direction filtering fusion. *Progress In Electromagnetics Research M*, 56:145–156, 2017.

[25] MV Sprindzuk, VA Kovalev, EV Snezhko, and SA Kharuzhyk. Lung cancer differential diagnosis based on the computer assisted radiology: The state of the art. *Polish journal of radiology*, 75(1):67, 2010.

[26] Kunio Doi. Computer-aided diagnosis in medical imaging: historical review, current status and future potential. *Computerized medical imaging and graphics*, 31(4-5):198–211, 2007.

[27] Gwilym S Lodwick, Theodore E Keats, and John P Dorst. The coding of roentgen images for computer analysis as applied to lung cancer. *Radiology*, 81(2):185–200, 1963.

[28] Ahmed Hosny, Chintan Parmar, John Quackenbush, Lawrence H Schwartz, and Hugo JWL Aerts. Artificial intelligence in radiology. *Nature Reviews Cancer*, 18(8):500–510, 2018.

[29] Ingrid Sluimer, Mathias Prokop, and Bram Van Ginneken. Toward automated segmentation of the pathological lung in ct. *IEEE transactions on medical imaging*, 24(8):1025–1038, 2005.

[30] Giorgio De Nunzio, Eleonora Tommasi, Antonella Agrusti, Rosella Cataldo, Ivan

De Mitri, Marco Favetta, Silvio Maglio, Andrea Massafra, Maurizio Quarta, Massimo Torsello, et al. Automatic lung segmentation in ct images with accurate handling of the hilar region. *Journal of digital imaging*, 24(1):11–27, 2011.

[31] Asem M Ali and Aly A Farag. Automatic lung segmentation of volumetric low-dose ct scans using graph cuts. In *International Symposium on Visual Computing*, pages 258–267. Springer, 2008.

[32] Vicky Goh, Steve Halligan, Anita Gharpuray, David Wellsted, Josefin Sundin, and Clive I Bartram. Quantitative assessment of colorectal cancer tumor vascular parameters by using perfusion ct: influence of tumor region of interest. *Radiology*, 247(3):726–732, 2008.

[33] Vincent Barra and Jean-Yves Boire. A general framework for the fusion of anatomical and functional medical images. *NeuroImage*, 13(3):410–424, 2001.

[34] Lucie Kavalcova, Richard Skaba, Martin Kyncl, Blanka Rouskova, and Ales Prochazka. The diagnostic value of mri fistulogram and mri distal colostogram in patients with anorectal malformations. *Journal of pediatric surgery*, 48(8):1806–1809, 2013.

[35] Bahareh Langari, Saeed Vaseghi, Ales Prochazka, Babak Vaziri, and Farzad Tahmasebi Aria. Edge-guided image gap interpolation using multi-scale transformation. *IEEE Transactions on Image Processing*, 25(9):4394–4405, 2016.

[36] Guihong Qu, Dali Zhang, and Pingfan Yan. Medical image fusion by wavelet transform modulus maxima. *Optics Express*, 9(4):184–190, 2001.

[37] Paul R Hill, Cedric Nishan Canagarajah, and David R Bull. Image fusion using complex wavelets. In *BMVC*, pages 1–10, 2002.

[38] Parul Shah, TV Srikanth, Shabbir N Merchant, and Uday B Desai. Multimodal image/video fusion rule using generalized pixel significance based on statistical properties of the neighborhood. *Signal, Image and Video Processing*, 8(4):723–738, 2014.

[39] Kun Zhan, Qiaoqiao Li, Jicai Teng, Mingying Wang, and Jinhui Shi. Multifocus image fusion using phase congruency. *Journal of Electronic Imaging*, 24(3):033014, 2015.

[40] Yuanyuan Li, Yanjing Sun, Xinhua Huang, Guanqiu Qi, Mingyao Zheng, and Zhiqin Zhu. An image fusion method based on sparse representation and sum modified-laplacian in nsct domain. *Entropy*, 20(7):522, 2018.

[41] Ming Yin, Xiaoning Liu, Yu Liu, and Xun Chen. Medical image fusion with parameter-adaptive pulse coupled neural network in nonsubsampled shearlet transform domain. *IEEE Transactions on Instrumentation and Measurement*, 68(1):49–64, 2018.

[42] Yu Liu, Xun Chen, Juan Cheng, and Hu Peng. A medical image fusion method based on convolutional neural networks. In *2017 20th international conference on information fusion (Fusion)*, pages 1–7. IEEE, 2017.

[43] Durga Prasad Bavirisetti and Ravindra Dhuli. Multi-focus image fusion using multi-scale image decomposition and saliency detection. *Ain Shams Engineering Journal*, 9(4):1103–1117, 2018.

[44] Sharma Dileepkumar Ramlal, Jainy Sachdeva, Chirag Kamal Ahuja, and Niranjan Khandelwal. Multimodal medical image fusion using non-subsampled shearlet transform and pulse coupled neural network incorporated with morphological gradient. *Signal, Image and Video Processing*, 12(8):1479–1487, 2018.

[45] Yu Liu, Xun Chen, Hu Peng, and Zengfu Wang. Multi-focus image fusion with a deep convolutional neural network. *Information Fusion*, 36:191–207, 2017.

[46] Kun Zhan, Yuange Xie, Haibo Wang, and Yufang Min. Fast filtering image fusion. *Journal of Electronic Imaging*, 26(6):063004, 2017.

[47] Durga Prasad Bavirisetti, Vijayakumar Kollu, Xiao Gang, and Ravindra Dhuli. Fusion of mri and ct images using guided image filter and image statistics. *International journal of Imaging systems and Technology*, 27(3):227–237, 2017.

[48] BK Shreyamsha Kumar. Image fusion based on pixel significance using cross bilateral filter. *Signal, image and video processing*, 9(5):1193–1204, 2015.

[49] Hyun Ho Choi, Ju Hwan Lee, Sung Min Kim, and Sung Yun Park. Speckle noise reduction in ultrasound images using a discrete wavelet transform-based image fusion technique. *Bio-medical materials and engineering*, 26(s1):S1587–S1597, 2015.

[50] Liu Shuaiqi, Zhao Jie, and Shi Mingzhu. Medical image fusion based on rolling guidance filter and spiking cortical model. *Computational and mathematical methods in medicine*, 2015, 2015.

[51] Kede Ma and Zhou Wang. Multi-exposure image fusion: A patch-wise approach. In *2015 IEEE International Conference on Image Processing (ICIP)*, pages 1717–1721. IEEE, 2015.

[52] Liu Shuaiqi, Zhu Zhihui, Li Huiya, Zhao Jie, and Wen Xin. Multi-focus image fusion using self-similarity and depth information in nonsubsampled shearlet transform domain. *International Journal of Signal Processing, Image Processing and Pattern Recognition*, 9(1):347–360, 2016.

[53] Tariq A Alshawi, Fathi E Abd El-Samie, and Saleh A Alshebeili. Magnetic resonance and computed tomography image fusion using bidimensional empirical mode decomposition.

In *2015 IEEE Global Conference on Signal and Information Processing (GlobalSIP)*, pages 413–417. IEEE, 2015.

[54] Yong Yang, Song Tong, Shuying Huang, and Pan Lin. Multifocus image fusion based on nsct and focused area detection. *IEEE Sensors Journal*, 15(5):2824–2838, 2014.

[55] Xiangzhi Bai, Yu Zhang, Fugen Zhou, and Bindang Xue. Quadtree-based multi-focus image fusion using a weighted focus-measure. *Information Fusion*, 22:105–118, 2015.

[56] Zhaodong Liu, Yi Chai, Hongpeng Yin, Jiayi Zhou, and Zhiqin Zhu. A novel multi-focus image fusion approach based on image decomposition. *Information Fusion*, 35:102–116, 2017.

[57] Anahita Fathi Kazerooni, Meysam Mohseni, Sahar Rezaei, Gholamreza Bakhshandeh-pour, and Hamidreza Saligheh Rad. Multi-parametric (adc/pwi/t2-w) image fusion approach for accurate semi-automatic segmentation of tumorous regions in glioblastoma multiforme. *Magnetic Resonance Materials in Physics, Biology and Medicine*, 28(1):13–22, 2015.

[58] Nóirín Duggan, Egil Bae, Shiwen Shen, William Hsu, Alex Bui, Edward Jones, Martin Glavin, and Luminita Vese. A technique for lung nodule candidate detection in ct using global minimization methods. In *International workshop on energy minimization methods in computer vision and pattern recognition*, pages 478–491. Springer, 2015.

[59] Huan Liu and Lei Yu. Toward integrating feature selection algorithms for classification and clustering. *IEEE Transactions on knowledge and data engineering*, 17(4):491–502, 2005.

[60] Yvan Saeys, Inaki Inza, and Pedro Larranaga. A review of feature selection techniques in bioinformatics. *bioinformatics*, 23(19):2507–2517, 2007.

[61] Bram Van Ginneken, Samuel G Armato III, Bartjan de Hoop, Saskia van Amelsvoort-van de Vorst, Thomas Duindam, Meindert Niemeijer, Keelin Murphy, Arnold Schilham, Alessandra Retico, Maria Evelina Fantacci, et al. Comparing and combining algorithms for computer-aided detection of pulmonary nodules in computed tomography scans: the anode09 study. *Medical image analysis*, 14(6):707–722, 2010.

[62] Joao Rodrigo Ferreira da Silva Sousa, Aristófanes Corrêa Silva, Anselmo Cardoso de Paiva, and Rodolfo Acatauassú Nunes. Methodology for automatic detection of lung nodules in computerized tomography images. *Computer methods and programs in biomedicine*, 98(1):1–14, 2010.

[63] Temesguen Messay, Russell C Hardie, and Steven K Rogers. A new computationally efficient cad system for pulmonary nodule detection in ct imagery. *Medical image analysis*, 14(3):390–406, 2010.

[64] Shu Ling Alycia Lee, Abbas Z Kouzani, and Eric J Hu. Random forest based lung nodule classification aided by clustering. *Computerized medical imaging and graphics*, 34(7):535–542, 2010.

[65] Michael C Lee, Lilla Boroczky, Kivilcim Sungur-Stasik, Aaron D Cann, Alain C Borczuk, Steven M Kawut, and Charles A Powell. Computer-aided diagnosis of pulmonary nodules using a two-step approach for feature selection and classifier ensemble construction. *Artificial intelligence in medicine*, 50(1):43–53, 2010.

[66] Hui Chen, Wenfang Wu, Hong Xia, Jing Du, Miao Yang, and Binrong Ma. Classification of pulmonary nodules using neural network ensemble. In *International Symposium on Neural Networks*, pages 460–466. Springer, 2011.

[67] Stelmo Magalhães Barros Netto, Aristófanes Corrêa Silva, Rodolfo Acatauassú Nunes, and Marcelo Gattass. Automatic segmentation of lung nodules with growing neural gas

and support vector machine. *Computers in biology and medicine*, 42(11):1110–1121, 2012.

[68] Donato Cascio, Rosario Magro, Francesco Fauci, Marius Iacomi, and Giuseppe Raso. Automatic detection of lung nodules in ct datasets based on stable 3d mass–spring models. *Computers in biology and medicine*, 42(11):1098–1109, 2012.

[69] Hui Chen, Jing Zhang, Yan Xu, Budong Chen, and Kuan Zhang. Performance comparison of artificial neural network and logistic regression model for differentiating lung nodules on ct scans. *Expert Systems with Applications*, 39(13):11503–11509, 2012.

[70] D Shiloah Elizabeth, H Khanna Nehemiah, C Sunil Retmin Raj, and Arputharaj Kannan. A novel segmentation approach for improving diagnostic accuracy of cad systems for detecting lung cancer from chest computed tomography images. *Journal of Data and Information Quality (JDIQ)*, 3(2):1–16, 2012.

[71] Atsushi Teramoto and Hiroshi Fujita. Fast lung nodule detection in chest ct images using cylindrical nodule-enhancement filter. *International journal of computer assisted radiology and surgery*, 8(2):193–205, 2013.

[72] Qingzhu Wang, Wenwei Kang, Chunming Wu, and Bin Wang. Computer-aided detection of lung nodules by svm based on 3d matrix patterns. *Clinical imaging*, 37(1):62–69, 2013.

[73] Ahmet Tartar, N Kılıç, and Aydin Akan. A new method for pulmonary nodule detection using decision trees. In *2013 35th Annual International Conference of the IEEE Engineering in Medicine and Biology Society (EMBC)*, pages 7355–7359. IEEE, 2013.

[74] Mohsen Keshani, Zohreh Azimifar, Farshad Tajeripour, and Reza Boostani. Lung nod-

ule segmentation and recognition using svm classifier and active contour modeling: A complete intelligent system. *Computers in biology and medicine*, 43(4):287–300, 2013.

[75] Hoon-seok Jang, Wook-Jin Choi, and Tae-Sun Choi. Optimal fuzzy rule based pulmonary nodule detection. *Advanced Science and Technology Letters*, 29:75–78, 2013.

[76] Jinsa Kuruvilla and K Gunavathi. Lung cancer classification using neural networks for ct images. *Computer methods and programs in biomedicine*, 113(1):202–209, 2014.

[77] Peng Cao, Jinzhu Yang, Wei Li, Dazhe Zhao, and Osmar Zaiane. Ensemble-based hybrid probabilistic sampling for imbalanced data learning in lung nodule cad. *Computerized Medical Imaging and Graphics*, 38(3):137–150, 2014.

[78] Antonio Oseas de Carvalho Filho, Wener Borges de Sampaio, Aristofanes Correa Silva, Anselmo Cardoso de Paiva, Rodolfo Acatauassu Nunes, and Marcelo Gattass. Automatic detection of solitary lung nodules using quality threshold clustering, genetic algorithm and diversity index. *Artificial intelligence in medicine*, 60(3):165–177, 2014.

[79] Pawel Badura and Ewa Pietka. Soft computing approach to 3d lung nodule segmentation in ct. *Computers in biology and medicine*, 53:230–243, 2014.

[80] Matthew S Brown, Pechin Lo, Jonathan G Goldin, Eran Barnoy, Grace Hyun J Kim, Michael F McNitt-Gray, and Denise R Aberle. Toward clinically usable cad for lung cancer screening with computed tomography. *European radiology*, 24(11):2719–2728, 2014.

[81] Erdal Taşcı and Aybars Uğur. Shape and texture based novel features for automated juxtapleural nodule detection in lung cts. *Journal of medical systems*, 39(5):1–13, 2015.

[82] Sheeraz Akram, Muhammad Younus Javed, Usman Qamar, Aasia Khanum, and Ali Hassan. Artificial neural network based classification of lungs nodule using hybrid features

from computerized tomographic images. *Applied Mathematics & Information Sciences*, 9(1):183–195, 2015.

[83] Bing Wang, Xuedong Tian, Qian Wang, Ying Yang, Hongzhi Xie, Shuyang Zhang, and Lixu Gu. Pulmonary nodule detection in ct images based on shape constraint cv model. *Medical physics*, 42(3):1241–1254, 2015.

[84] Aydın Kaya and Ahmet Burak Can. A weighted rule based method for predicting malignancy of pulmonary nodules by nodule characteristics. *Journal of biomedical informatics*, 56:69–79, 2015.

[85] Zhenghao Shi, Binxin Xu, Minghua Zhao, Jinwei Zhao, Yinghui Wang, Yonghong Liu, Ming Zhang, Lifeng He, and Kenji Suzuki. A joint roi extraction filter for computer aided lung nodule detection. *Bio-medical materials and engineering*, 26(s1):S1491–S1499, 2015.

[86] Shuangfeng Dai, Ke Lu, Jiyang Dong, Yifei Zhang, and Yong Chen. A novel approach of lung segmentation on chest ct images using graph cuts. *Neurocomputing*, 168:799–807, 2015.

[87] Hao Han, Lihong Li, Fangfang Han, Bowen Song, William Moore, and Zhengrong Liang. Fast and adaptive detection of pulmonary nodules in thoracic ct images using a hierarchical vector quantization scheme. *IEEE journal of biomedical and health informatics*, 19(2):648–659, 2014.

[88] Shiwen Shen, Alex AT Bui, Jason Cong, and William Hsu. An automated lung segmentation approach using bidirectional chain codes to improve nodule detection accuracy. *Computers in biology and medicine*, 57:139–149, 2015.

[89] Kai-Lung Hua, Che-Hao Hsu, Shintami Chusnul Hidayati, Wen-Huang Cheng, and Yu-

Jen Chen. Computer-aided classification of lung nodules on computed tomography images via deep learning technique. *OncoTargets and therapy*, 8, 2015.

[90] Macedo Firmino, Giovani Angelo, Higor Morais, Marcel R Dantas, and Ricardo Valentim. Computer-aided detection (cade) and diagnosis (cadx) system for lung cancer with likelihood of malignancy. *Biomedical engineering online*, 15(1):1–17, 2016.

[91] Aiden Nibali, Zhen He, and Dennis Wollersheim. Pulmonary nodule classification with deep residual networks. *International journal of computer assisted radiology and surgery*, 12(10):1799–1808, 2017.

[92] Qi Dou, Hao Chen, Lequan Yu, Jing Qin, and Pheng-Ann Heng. Multilevel contextual 3-d cnns for false positive reduction in pulmonary nodule detection. *IEEE Transactions on Biomedical Engineering*, 64(7):1558–1567, 2016.

[93] Giovanni LF da Silva, Otílio P da Silva Neto, Aristófanes C Silva, Anselmo C de Paiva, and Marcelo Gattass. Lung nodules diagnosis based on evolutionary convolutional neural network. *Multimedia Tools and Applications*, 76(18):19039–19055, 2017.

[94] Wenqing Sun, Bin Zheng, and Wei Qian. Automatic feature learning using multichannel roi based on deep structured algorithms for computerized lung cancer diagnosis. *Computers in biology and medicine*, 89:530–539, 2017.

[95] Anindya Gupta, Tonis Saar, Olev Martens, and Yannick Le Moullec. Automatic detection of multisize pulmonary nodules in ct images: Large-scale validation of the false-positive reduction step. *Medical physics*, 45(3):1135–1149, 2018.

[96] Weihang Zhang, Xue Wang, Xuanping Li, and Junfeng Chen. 3d skeletonization feature based computer-aided detection system for pulmonary nodules in ct datasets. *Computers in biology and medicine*, 92:64–72, 2018.

[97] M Arfan Jaffar, Abdul Basit Siddiqui, and Mubashar Mushtaq. Ensemble classification of pulmonary nodules using gradient intensity feature descriptor and differential evolution. *Cluster Computing*, 21(1):393–407, 2018.

[98] Issa Ali, Gregory R Hart, Gowthaman Gunabushanam, Ying Liang, Wazir Muhammad, Bradley Nartowt, Michael Kane, Xiaomei Ma, and Jun Deng. Lung nodule detection via deep reinforcement learning. *Frontiers in oncology*, 8:108, 2018.

[99] Hongyang Jiang, He Ma, Wei Qian, Mengdi Gao, and Yan Li. An automatic detection system of lung nodule based on multigroup patch-based deep learning network. *IEEE journal of biomedical and health informatics*, 22(4):1227–1237, 2017.

[100] Chaofeng Li, Guoce Zhu, Xiaojun Wu, and Yuanquan Wang. False-positive reduction on lung nodules detection in chest radiographs by ensemble of convolutional neural networks. *IEEE Access*, 6:16060–16067, 2018.

[101] Ratishchandra Huidrom, Yambem Jina Chanu, and Khumanthem Manglem Singh. Pulmonary nodule detection on computed tomography using neuro-evolutionary scheme. *Signal, Image and Video Processing*, 13(1):53–60, 2019.

[102] Furqan Shaukat, Gulistan Raja, Rehan Ashraf, Shehzad Khalid, Mudassar Ahmad, and Amjad Ali. Artificial neural network based classification of lung nodules in ct images using intensity, shape and texture features. *Journal of Ambient Intelligence and Humanized Computing*, 10(10):4135–4149, 2019.

[103] Seba Susan, Dhaarna Sethi, and Kriti Arora. Cw-cae: pulmonary nodule detection from imbalanced dataset using class-weighted convolutional autoencoder. In *International Conference on innovative computing and communications*, pages 825–833. Springer, 2021.

[104] Gopi Kasinathan, Selvakumar Jayakumar, Amir H Gandomi, Manikandan Ramachandran, Simon James Fong, and Rizwan Patan. Automated 3-d lung tumor detection and classification by an active contour model and cnn classifier. *Expert Systems with Applications*, 134:112–119, 2019.

[105] Yaling Pan, Dejun Shi, Hanqi Wang, Tongtong Chen, Deqi Cui, Xiaoguang Cheng, and Yong Lu. Automatic opportunistic osteoporosis screening using low-dose chest computed tomography scans obtained for lung cancer screening. *European radiology*, 30(7):4107, 2020.

[106] V Pranathi, G Ranadheer Reddy, G Sunil, D Raghava Kumari, and Bhavana Jamalpur. A comprehensive study on the various applications of deep learning. In *IOP Conference Series: Materials Science and Engineering*, volume 981, page 022045. IOP Publishing, 2020.

[107] M Attique Khan, Sadia Rubab, Asifa Kashif, Muhammad Imran Sharif, Nazeer Muhammad, Jamal Hussain Shah, Yu-Dong Zhang, and Suresh Chandra Satapathy. Lungs cancer classification from ct images: An integrated design of contrast based classical features fusion and selection. *Pattern Recognition Letters*, 129:77–85, 2020.

[108] Mohd Firdaus Abdullah, Siti Noraini Sulaiman, Muhammad Khusairi Osman, Noor Khairiah A Karim, Ibrahim Lutfi Shuaib, and Muhamad Danial Irfan Alhamdu. Classification of lung cancer stages from ct scan images using image processing and k-nearest neighbours. In *2020 11th IEEE Control and System Graduate Research Colloquium (ICSGRC)*, pages 68–72. IEEE, 2020.

[109] Vikul J Pawar, Kailash D Kharat, Suraj R Pardeshi, and Prashant D Pathak. Lung cancer detection system using image processing and machine learning techniques. *Cancer*, 3:4, 2020.

[110] Yi Li, Junli Zhao, Zhihan Lv, and Zhenkuan Pan. Multimodal medical supervised image fusion method by cnn. *Frontiers in Neuroscience*, 15:303, 2021.

[111] G Vijaya and A Suhasini. An adaptive preprocessing of lung ct images with various filters for better enhancement. *Academic Journal of Cancer Research*, 7(3):179–184, 2014.

[112] Bejnordi BE Litjens G, Kooi T. A survey on deep learning in medical image analysi. *Med Image Anal*, 42(3):60–88, 2017.

[113] Jiantao Pu, Justus Roos, A Yi Chin, Sandy Napel, Geoffrey D Rubin, and David S Paik. Adaptive border marching algorithm: automatic lung segmentation on chest ct images. *Computerized Medical Imaging and Graphics*, 32(6):452–462, 2008.

[114] K Senthil Kumar, K Venkatalakshmi, and K Karthikeyan. Lung cancer detection using image segmentation by means of various evolutionary algorithms. *Computational and mathematical methods in medicine*, pages 1–16, 2019.

[115] Onika Akter, Mohammad Ali Moni, Mohammad Mahfuzul Islam, Julian MW Quinn, and AHM Kamal. Lung cancer detection using enhanced segmentation accuracy. *Applied Intelligence*, pages 1–14, 2020.

[116] Jiao Du, Weisheng Li, Ke Lu, and Bin Xiao. An overview of multi-modal medical image fusion. *Neurocomputing*, 215:3–20, 2016.

[117] Shutao Li, Haitao Yin, and Leyuan Fang. Group-sparse representation with dictionary learning for medical image denoising and fusion. *IEEE Transactions on biomedical engineering*, 59(12):3450–3459, 2012.

[118] Hong Liu, Haichao Cao, Enmin Song, Guangzhi Ma, Xiangyang Xu, Renchao Jin, Yong Jin, and Chih-Cheng Hung. A cascaded dual-pathway residual network for lung nodule segmentation in ct images. *Physica Medica*, 63:112–121, 2019.

[119] N Aishwarya and C Bennila Thangammal. A novel multimodal medical image fusion using sparse representation and modified spatial frequency. *International Journal of Imaging Systems and Technology*, 28(3):175–185, 2018.

[120] Rajveer Kaur and Er Gurpreet Kaur. Medical image fusion using redundant wavelet based ica co-variance analysis. *Int J Eng Comp Sci*, 4(08):28, 2015.

[121] Xingbin Liu, Wenbo Mei, and Huiqian Du. Detail-enhanced multimodality medical image fusion based on gradient minimization smoothing filter and shearing filter. *Medical & biological engineering & computing*, 56(9):1565–1578, 2018.

[122] GK Matsopoulos, S Marshall, and JNH Brunt. Multiresolution morphological fusion of mr and ct images of the human brain. *IEE Proceedings-Vision, Image and Signal Processing*, 141(3):137–142, 1994.

[123] Jiao Du, Weisheng Li, Bin Xiao, and Qamar Nawaz. Union laplacian pyramid with multiple features for medical image fusion. *Neurocomputing*, 194:326–339, 2016.

[124] Liang Kou, Liguo Zhang, Kejia Zhang, Jianguo Sun, Qilong Han, and Zilong Jin. A multi-focus image fusion method via region mosaicking on laplacian pyramids. *PloS one*, 13(5):e0191085, 2018.

[125] Xinhua Li and Jing Zhao. A novel multi-modal medical image fusion algorithm. *Journal of Ambient Intelligence and Humanized Computing*, 12(2):1995–2002, 2021.

[126] Ahmed Soliman, Fahmi Khalifa, Ahmed Elnakib, Mohamed Abou El-Ghar, Neal Dunlap, Brian Wang, Georgy Gimel'farb, Robert Keynton, and Ayman El-Baz. Accurate lungs segmentation on ct chest images by adaptive appearance-guided shape modeling. *IEEE transactions on medical imaging*, 36(1):263–276, 2016.

[127] Muhammad Adeel Azam, Khan Bahadar Khan, Muhammad Ahmad, and Manuel Mazzara. Multimodal medical image registration and fusion for quality enhancement. *CMC-COMPUTERS MATERIALS & CONTINUA*, 68(1):821–840, 2021.

[128] Hiram Madero Orozco, Osslan Osiris Vergara Villegas, Humberto de Jesús Ochoa Domínguez, and Vianey Guadalupe Cruz Sánchez. Lung nodule classification in ct thorax images using support vector machines. In *2013 12th Mexican International Conference on Artificial Intelligence*, pages 277–283. IEEE, 2013.

[129] Sheeraz Akram, Muhammad Younus Javed, M Usman Akram, Usman Qamar, and Ali Hassan. Pulmonary nodules detection and classification using hybrid features from computerized tomographic images. *Journal of Medical Imaging and Health Informatics*, 6(1):252–259, 2016.

[130] G Curigliano, S Banerjee, A Cervantes, MC Garassino, P Garrido, N Girard, J Haanen, K Jordan, F Lordick, Jean-Pascal Machiels, et al. Managing cancer patients during the covid-19 pandemic: an esmo multidisciplinary expert consensus. *Annals of Oncology*, 31(10):1320–1335, 2020.

[131] Tingting Chen, Xinjun Ma, Xingde Ying, Wenzhe Wang, Chunnv Yuan, Weiguo Lu, Danny Z Chen, and Jian Wu. Multi-modal fusion learning for cervical dysplasia diagnosis. pages 1505–1509. IEEE, 2019.

[132] Xiaole Ma, Shaohai Hu, Shuaiqi Liu, Jing Fang, and Shuwen Xu. Multi-focus image fusion based on joint sparse representation and optimum theory. *Signal Processing: Image Communication*, 78:125–134, 2019.

[133] Zhiqin Zhu, Yi Chai, Hongpeng Yin, Yanxia Li, and Zhaodong Liu. A novel dictionary learning approach for multi-modality medical image fusion. *Neurocomputing*, 214:471–482, 2016.

[134] Huafeng Li, Xiaoge He, Dapeng Tao, Yuanyan Tang, and Ruxin Wang. Joint medical image fusion, denoising and enhancement via discriminative low-rank sparse dictionaries learning. *Pattern Recognition*, 79:130–146, 2018.

[135] Yu Liu, Xun Chen, Rabab K Ward, and Z Jane Wang. Medical image fusion via convolutional sparsity based morphological component analysis. *IEEE Signal Processing Letters*, 26(3):485–489, 2019.

[136] Wei Jiang, Xiaomin Yang, Wei Wu, Kai Liu, Awais Ahmad, Arun Kumar Sangaiah, and Gwanggil Jeon. Medical images fusion by using weighted least squares filter and sparse representation. *Computers & Electrical Engineering*, 67:252–266, 2018.

[137] Zhiping Xu. Medical image fusion using multi-level local extrema. *Information Fusion*, 19:38–48, 2014.

[138] Sarmad Maqsood and Umer Javed. Multi-modal medical image fusion based on two-scale image decomposition and sparse representation. *Biomedical Signal Processing and Control*, 57:101810, 2020.

[139] Xiaopeng Guo, Rencan Nie, Jinde Cao, Dongming Zhou, and Wenhua Qian. Fully convolutional network-based multifocus image fusion. *Neural computation*, 30(7):1775–1800, 2018.

[140] Hui Li and Xiao-Jun Wu. Densefuse: A fusion approach to infrared and visible images. *IEEE Transactions on Image Processing*, 28(5):2614–2623, 2018.

[141] Yu Zhang, Yu Liu, Peng Sun, Han Yan, Xiaolin Zhao, and Li Zhang. Ifcnn: A general image fusion framework based on convolutional neural network. *Information Fusion*, 54:99–118, 2020.

[142] Jiayi Ma, Han Xu, Junjun Jiang, Xiaoguang Mei, and Xiao-Ping Zhang. Ddcgan: A dual-discriminator conditional generative adversarial network for multi-resolution image fusion. *IEEE Transactions on Image Processing*, 29:4980–4995, 2020.

[143] Qi Zhang, Xiaoyong Shen, Li Xu, and Jiaya Jia. Rolling guidance filter. In *European conference on computer vision*, pages 815–830. Springer, 2014.

[144] Run Mao, Xian Song Fu, Ping-juan Niu, Hui Quan Wang, Jie Pan, Shu Shu Li, and Lei Liu. Multi-directional laplacian pyramid image fusion algorithm. In *2018 3rd International Conference on Mechanical, Control and Computer Engineering (ICMCCE)*, pages 568–572. IEEE, 2018.

[145] Yu Liu and Zengfu Wang. Simultaneous image fusion and denoising with adaptive sparse representation. *IET Image Processing*, 9(5):347–357, 2015.

[146] Fabian Hollaus, Markus Diem, and Robert Sablatnig. Multispectral image binarization using gmms. In *2018 16th International Conference on Frontiers in Handwriting Recognition (ICFHR)*, pages 570–575. IEEE, 2018.

[147] Brahim Ait Skourt, Abdelhamid El Hassani, and Aicha Majda. Lung ct image segmentation using deep neural networks. *Procedia Computer Science*, 127:109–113, 2018.

[148] Syeda Furruka Banu, Md Sarker, Mostafa Kamal, Mohamed Abdel-Nasser, Domenec Puig, and Hatem A Raswan. Aweu-net: An attention-aware weight excitation u-net for lung nodule segmentation. *Applied Sciences*, 11(21):10132, 2021.

[149] Joana Rocha, António Cunha, and Ana Maria Mendonça. Conventional filtering versus u-net based models for pulmonary nodule segmentation in ct images. *Journal of medical systems*, 44(4):1–8, 2020.

[150] Suvadip Mukherjee, Xiaojie Huang, and Roshni R Bhagalia. Lung nodule segmentation using deep learned prior based graph cut. In *2017 IEEE 14th international symposium on biomedical imaging (ISBI 2017)*, pages 1205–1208. IEEE, 2017.

[151] Wenzhe Wang, Yifei Lu, Bian Wu, Tingting Chen, Danny Z Chen, and Jian Wu. Deep active self-paced learning for accurate pulmonary nodule segmentation. In *International Conference on Medical Image Computing and Computer-Assisted Intervention*, pages 723–731. Springer, 2018.

[152] Junjie Zhang, Yong Xia, Hengfei Cui, and Yanning Zhang. Pulmonary nodule detection in medical images: A survey. *Biomedical Signal Processing and Control*, 43:138–147, 2018.

[153] Xinyang Feng, Jie Yang, Andrew F Laine, and Elsa D Angelini. Discriminative localization in cnns for weakly-supervised segmentation of pulmonary nodules. In *International conference on medical image computing and computer-assisted intervention*, pages 568–576. Springer, 2017.

[154] Jiaxing Tan, Longlong Jing, Yumei Huo, Lihong Li, Oguz Akin, and Yingli Tian. Lgan: Lung segmentation in ct scans using generative adversarial network. *Computerized Medical Imaging and Graphics*, 87:101817, 2021.

[155] Sihang Chen and Yifan Wang. Pulmonary nodule segmentation in computed tomography with an encoder-decoder architecture. In *2019 10th International Conference on Information Technology in Medicine and Education (ITME)*, pages 157–162. IEEE, 2019.

[156] Nabila Abraham and Naimul Mefraz Khan. A novel focal tversky loss function with improved attention u-net for lesion segmentation. In *2019 IEEE 16th International Symposium on Biomedical Imaging (ISBI 2019)*, pages 683–687. IEEE, 2019.

[157] Jo Schlemper, Ozan Oktay, Michiel Schaap, Mattias Heinrich, Bernhard Kainz, Ben Glocker, and Daniel Rueckert. Attention gated networks: Learning to leverage salient regions in medical images. *Medical image analysis*, 53:197–207, 2019.

[158] Xiaomeng Li, Hao Chen, Xiaojuan Qi, Qi Dou, Chi-Wing Fu, and Pheng-Ann Heng. H-denseunet: hybrid densely connected unet for liver and tumor segmentation from ct volumes. *IEEE transactions on medical imaging*, 37(12):2663–2674, 2018.

[159] Zongwei Zhou, Md Mahfuzur Rahman Siddiquee, Nima Tajbakhsh, and Jianming Liang. Unet++: A nested u-net architecture for medical image segmentation. In *Deep learning in medical image analysis and multimodal learning for clinical decision support*, pages 3–11. Springer, 2018.

[160] Deng-Ping Fan, Tao Zhou, Ge-Peng Ji, Yi Zhou, Geng Chen, Huazhu Fu, Jianbing Shen, and Ling Shao. Inf-net: Automatic covid-19 lung infection segmentation from ct images. *IEEE Transactions on Medical Imaging*, 39(8):2626–2637, 2020.

[161] Vijay Badrinarayanan, Alex Kendall, and Roberto Cipolla. Segnet: A deep convolutional encoder-decoder architecture for image segmentation. *IEEE transactions on pattern analysis and machine intelligence*, 39(12):2481–2495, 2017.

[162] Changqian Yu, Jingbo Wang, Chao Peng, Changxin Gao, Gang Yu, and Nong Sang. Bisenet: Bilateral segmentation network for real-time semantic segmentation. In *Proceedings of the European conference on computer vision (ECCV)*, pages 325–341, 2018.

[163] Sachin Mehta, Mohammad Rastegari, Anat Caspi, Linda Shapiro, and Hannaneh Hajishirzi. Espnet: Efficient spatial pyramid of dilated convolutions for semantic segmentation. In *Proceedings of the european conference on computer vision (ECCV)*, pages 552–568, 2018.

[164] Adel Oulefki, Sos Agaian, Thaweesak Trongtirakul, and Azzeddine Kassah Laouar. Automatic covid-19 lung infected region segmentation and measurement using ct-scans images. *Pattern recognition*, 114:107747, 2021.

[165] Kaihua Zhang, Lei Zhang, Huihui Song, and David Zhang. Reinitialization-free level set evolution via reaction diffusion. *IEEE Transactions on Image Processing*, 22(1):258–271, 2012.

[166] Chunming Li, Chenyang Xu, Changfeng Gui, and Martin D Fox. Level set evolution without re-initialization: a new variational formulation. In *2005 IEEE computer society conference on computer vision and pattern recognition (CVPR'05)*, volume 1, pages 430–436. IEEE, 2005.

[167] Shanhui Sun, Christian Bauer, and Reinhard Beichel. Automated 3-d segmentation of lungs with lung cancer in ct data using a novel robust active shape model approach. *IEEE transactions on medical imaging*, 31(2):449–460, 2011.

[168] Zhipeng Gui, Dehua Peng, Huayi Wu, and Xi Long. Msgc: Multi-scale grid clustering by fusing analytical granularity and visual cognition for detecting hierarchical spatial patterns. *Future Generation Computer Systems*, 112:1038–1056, 2020.

[169] Gemma Piella and Henk Heijmans. A new quality metric for image fusion. In *Proceedings 2003 International Conference on Image Processing (Cat. No. 03CH37429)*, volume 3, pages III–173. IEEE, 2003.

[170] Harbinder Singh, Vinay Kumar, and Sunil Bhooshan. Weighted least squares based detail enhanced exposure fusion. *International Scholarly Research Notices*, 2014:1–18, 2014.

[171] Costas S Xydeas, Vladimir Petrovic, et al. Objective image fusion performance measure. *Electronics letters*, 36(4):308–309, 2000.

[172] Vladimir Petrovic and Costas Xydeas. Objective image fusion performance characterisation. In *Tenth IEEE International Conference on Computer Vision (ICCV'05) Volume 1*, volume 2, pages 1866–1871. IEEE, 2005.

[173] K Joseph Abraham Sundar, Motepalli Jahnavi, and Konudula Lakshmisaritha. Multi-sensor image fusion based on empirical wavelet transform. In *2017 International Conference on Electrical, Electronics, Communication, Computer, and Optimization Techniques (ICEECCOT)*, pages 93–97. IEEE, 2017.

[174] Filippo Nencini, Andrea Garzelli, Stefano Baronti, and Luciano Alparone. Remote sensing image fusion using the curvelet transform. *Information fusion*, 8(2):143–156, 2007.

[175] Qiang Zhang and Bao-long Guo. Multifocus image fusion using the nonsubsampled contourlet transform. *Signal processing*, 89(7):1334–1346, 2009.

[176] Bin Yang and Shutao Li. Multifocus image fusion and restoration with sparse representation. *IEEE Transactions on Instrumentation and Measurement*, 59(4):884–892, 2009.

[177] Syed Muhammad Naqi, Muhammad Sharif, and Arfan Jaffar. Lung nodule detection and classification based on geometric fit in parametric form and deep learning. *Neural Computing and Applications*, 32(9):4629–4647, 2020.

[178] Hongtao Xie, Dongbao Yang, Nannan Sun, Zhineng Chen, and Yongdong Zhang. Automated pulmonary nodule detection in ct images using deep convolutional neural networks. *Pattern Recognition*, 85:109–119, 2019.

[179] Atsushi Teramoto and Hiroshi Fujita. Automated lung nodule detection using positron emission tomography/computed tomography. In *Artificial intelligence in decision support systems for diagnosis in medical imaging*, pages 87–110. Springer, 2018.

[180] Ruchita Tekade. Lung nodule detection and classification using machine learning techniques. *Asian Journal For Convergence In Technology (AJCT)*, 2018.

[181] Dhevendra Alagan Palanivel, Sivakumaran Natarajan, and Sainarayanan Gopalakrishnan. Mutifractals based multimodal 3d image registration. *Biomedical Signal Processing and Control*, 47:126–136, 2019.

[182] Zheng Cui, Sasan Mahmoodi, Matthew Guy, Emma Lewis, Tom Havelock, Michael Bennett, and Joy Conway. A general framework in single and multi-modality registration for lung imaging analysis using statistical prior shapes. *Computer methods and programs in biomedicine*, 187:105232, 2020.

[183] Rabia Bashir, Riaz Junejo, Nadia N Qadri, Martin Fleury, and Muhammad Yasir Qadri. Swt and pca image fusion methods for multi-modal imagery. *Multimedia Tools and Applications*, 78(2):1235–1263, 2019.

[184] Yin Fei, Gao Wei, and Song Zongxi. Medical image fusion based on feature extraction and sparse representation. *International journal of biomedical imaging*, 2017, 2017.

[185] J Reena Benjamin and T Jayasree. Improved medical image fusion based on cascaded pca and shift invariant wavelet transforms. *International journal of computer assisted radiology and surgery*, 13(2):229–240, 2018.

[186] Shabana R Ziyad, V Radha, and V Thavavel. Performance evaluation of lung segmentation techniques in computer aided lung nodule detection system. In *International Conference on Futuristic Trends in Networks and Computing Technologies*, pages 619–633. Springer, 2019.

[187] Nasrullah Nasrullah, Jun Sang, Mohammad S Alam, Muhammad Mateen, Bin Cai, and

Haibo Hu. Automated lung nodule detection and classification using deep learning combined with multiple strategies. *Sensors*, 19(17):3722, 2019.

[188] Guobin Zhang, Zhiyong Yang, Li Gong, Shan Jiang, and Lu Wang. Classification of benign and malignant lung nodules from ct images based on hybrid features. *Physics in Medicine & Biology*, 64(12):125011, 2019.

[189] Zhiqin Zhu, Mingyao Zheng, Guanqiu Qi, Di Wang, and Yan Xiang. A phase congruency and local laplacian energy based multi-modality medical image fusion method in nsct domain. *IEEE Access*, 7:20811–20824, 2019.

[190] Zhaobin Wang, Zijing Cui, and Ying Zhu. Multi-modal medical image fusion by laplacian pyramid and adaptive sparse representation. *Computers in Biology and Medicine*, 123:103823, 2020.

[191] Sajid Ali Khan, Muhammad Attique Khan, Oh-Young Song, and Muhammad Nazir. Medical imaging fusion techniques: a survey benchmark analysis, open challenges and recommendations. *Journal of Medical Imaging and Health Informatics*, 10(11):2523–2531, 2020.

[192] J Dafni Rose, K Jaspin, and K Vijayakumar. Lung cancer diagnosis based on image fusion and prediction using ct and pet image. In *Signal and Image Processing Techniques for the Development of Intelligent Healthcare Systems*, pages 67–86. Springer, 2021.

[193] Ning Xiao, Wanting Yang, Qiang Yan, Juanjuan Zhao, Rui Hao, Jianhong Lian, and Shuo Li. PET and CT image fusion of lung cancer with siamese pyramid fusion network. *Frontiers in Medicine*, page 886, 2022.

[194] Kenneth Clark, Bruce Vendt, Kirk Smith, John Freymann, Justin Kirby, Paul Koppel, Stephen Moore, Stanley Phillips, David Maffitt, Michael Pringle, et al. The cancer imag-

ing archive (tcia): maintaining and operating a public information repository. *Journal of digital imaging*, 26(6):1045–1057, 2013.

[195] Frederik Maes, Dirk Vandermeulen, and Paul Suetens. Medical image registration using mutual information. *Proceedings of the IEEE*, 91(10):1699–1722, 2003.

[196] Sharma Dileepkumar Ramlal, Jainy Sachdeva, Chirag Kamal Ahuja, and Niranjan Khandelwal. An improved multimodal medical image fusion scheme based on hybrid combination of nonsubsampled contourlet transform and stationary wavelet transform. *International Journal of Imaging Systems and Technology*, 29(2):146–160, 2019.

[197] Xiao-lin Zhang, Zhi-fang Liu, Yong Kou, Jin-bo Dai, and Zhi-meng Cheng. Quality assessment of image fusion based on image content and structural similarity. In *2010 2nd International Conference on Information Engineering and Computer Science*, pages 1–4. IEEE, 2010.

[198] R Vijayarajan and S Muttan. Discrete wavelet transform based principal component averaging fusion for medical images. *AEU-International Journal of Electronics and Communications*, 69(6):896–902, 2015.

[199] Zheng Liu, Erik Blasch, Zhiyun Xue, Jiying Zhao, Robert Laganiere, and Wei Wu. Objective assessment of multiresolution image fusion algorithms for context enhancement in night vision: a comparative study. *IEEE transactions on pattern analysis and machine intelligence*, 34(1):94–109, 2011.

[200] Cui Yang, Jian-Qi Zhang, Xiao-Rui Wang, and Xin Liu. A novel similarity based quality metric for image fusion. *Information Fusion*, 9(2):156–160, 2008.

[201] Zhiqin Zhu, Guanqiu Qi, Yi Chai, Hongpeng Yin, and Jian Sun. A novel visible-infrared

image fusion framework for smart city. *International Journal of Simulation and Process Modelling*, 13(2):144–155, 2018.

[202] Hamid R Sheikh and Alan C Bovik. Image information and visual quality. *IEEE Transactions on image processing*, 15(2):430–444, 2006.

[203] Imran Nazir, Ihsan Ul Haq, Muhammad Mohsin Khan, Muhammad Bilal Qureshi, Hayat Ullah, and Sharjeel Butt. Efficient pre-processing and segmentation for lung cancer detection using fused CT images. *Electronics*, 11(1):34, 2021.

[204] Eali Stephen Neal Joshua, Debnath Bhattacharyya, Midhun Chakkravarthy, and Yung-Cheol Byun. 3d cnn with visual insights for early detection of lung cancer using gradient-weighted class activation. *Journal of Healthcare Engineering*, 2021, 2021.

[205] Gopi Kasinathan and Selvakumar Jayakumar. Cloud-based lung tumor detection and stage classification using deep learning techniques. *BioMed Research International*, 2022, 2022.

[206] U Rajendra Acharya, Shu Lih Oh, Yuki Hagiwara, Jen Hong Tan, and Hojjat Adeli. Deep convolutional neural network for the automated detection and diagnosis of seizure using eeg signals. *Computers in biology and medicine*, 100:270–278, 2018.